

Winter 1988

Dynamic processes and kinetic theory of plasma fluctuations: ARCS3

Keyun Tang

University of New Hampshire, Durham

Follow this and additional works at: <https://scholars.unh.edu/dissertation>

Recommended Citation

Tang, Keyun, "Dynamic processes and kinetic theory of plasma fluctuations: ARCS3" (1988). *Doctoral Dissertations*. 1567.
<https://scholars.unh.edu/dissertation/1567>

This Dissertation is brought to you for free and open access by the Student Scholarship at University of New Hampshire Scholars' Repository. It has been accepted for inclusion in Doctoral Dissertations by an authorized administrator of University of New Hampshire Scholars' Repository. For more information, please contact nicole.hentz@unh.edu.

INFORMATION TO USERS

The most advanced technology has been used to photograph and reproduce this manuscript from the microfilm master. UMI films the text directly from the original or copy submitted. Thus, some thesis and dissertation copies are in typewriter face, while others may be from any type of computer printer.

The quality of this reproduction is dependent upon the quality of the copy submitted. Broken or indistinct print, colored or poor quality illustrations and photographs, print bleedthrough, substandard margins, and improper alignment can adversely affect reproduction.

In the unlikely event that the author did not send UMI a complete manuscript and there are missing pages, these will be noted. Also, if unauthorized copyright material had to be removed, a note will indicate the deletion.

Oversize materials (e.g., maps, drawings, charts) are reproduced by sectioning the original, beginning at the upper left-hand corner and continuing from left to right in equal sections with small overlaps. Each original is also photographed in one exposure and is included in reduced form at the back of the book. These are also available as one exposure on a standard 35mm slide or as a 17" x 23" black and white photographic print for an additional charge.

Photographs included in the original manuscript have been reproduced xerographically in this copy. Higher quality 6" x 9" black and white photographic prints are available for any photographs or illustrations appearing in this copy for an additional charge. Contact UMI directly to order.

U·M·I

University Microfilms International
A Bell & Howell Information Company
300 North Zeeb Road, Ann Arbor, MI 48106-1346 USA
313/761-4700 800/521-0600

Order Number 8907449

**Dynamic processes and kinetic theory of plasma fluctuations:
ARCS3**

Tang, Keyun, Ph.D.

University of New Hampshire, 1988

Copyright ©1989 by Tang, Keyun. All rights reserved.

U·M·I
300 N. Zeeb Rd.
Ann Arbor, MI 48106

**DYNAMIC PROCESSES AND KINETIC THEORY OF
PLASMA FLUCTUATIONS: ARCS3**

BY

KEYUN TANG

B.S., University of Science and Technology of China, 1970

M.S., Graduate School, Academy of Sciences of China, 1981

DISSERTATION

**Submitted to the University of New Hampshire
in Partial Fulfillment of
the Requirements for the Degree of**

Doctor of Philosophy

in

Physics

December, 1988

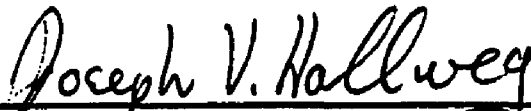
This Dissertation has been examined and approved.



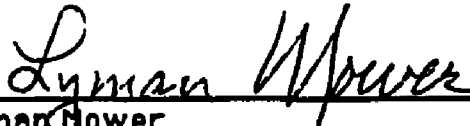
Richard L. Kaufmann, Dissertation Director
Professor of Physics



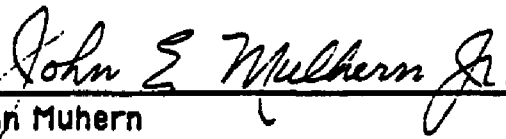
Roger L. Arnoldy, Professor of Physics
Associate Director of EOS



Joseph Hallweg, Research Professor of EOS
Director of Solar-Terrestrial Theory Group



Lyman Hower
Professor of Physics



John Mulhern
Professor of Physics

Nov 22, 1988
Date

TO

MY PARENTS

TO

MY MOTHERLAND

ACKNOWLEDGEMENT

Firs of all, I extend all my gratitude to professor Richard L. Kaufmann who had brought me together with this suitable project, which involves many meaningful concepts of both Physics and Mathematics, and who helped me immensely during the course of this project with his knowledge in plasma physics and computer programming. Professor Roger Arnoldy and Dr. Craig Pollock, Hank Dolben, Professor Larry Cahill and Dr. Robert Erlandson all generously provided me with primary data about the ARCS3 flight, for which I express the deepest appreciation. Professor John Mulhern, Professor Lyman Mower and Professor Joseph Hollweg provided helpful advice during numerous discussions, all of which greatly assisted the completion of this thesis.

Upon the conclusion of this thesis, I would like to thank all the teachers I have known at UNH and back in China, especially my high school Physics teacher, Mr. Li Ping, whose explicit and captivating teaching inspired my interest in Physics and is still helping me to this day. I also have to acknowledge and thank many of my fellow graduate students in the Physics department: Dipen Bhattacharya, James Connelly, Steve Froking, Dr. Rich Ludlow, Dr. Mark McConnell, Dr. Tom Milliman, Mark Popecki, Parameswarn Sreekumar, Dr. Alphonse Sterling and others, their friendship and help furthered the progress of this thesis. Thanks Sherry Palmer for helping me to polish some graphs . My profound thanks to Professor Lennard Fisk, who admitted me to UNH as academic advi-

sor, without whom my life would not cross paths with the campus of the University of New Hampshire.

Last of all, probably most importantly, I have to thank my very own family, for putting up with everything during the course of this thesis, for trying to be helpful even when they really aren't, for relieving me of everyday housework and especial thanks to my daughter Helen, for typing and correcting the manuscript.

I would like to thank NSF for their support of this work through grant ATM-85-21819. I would also to thank Drs. John. Lockwood and Jim Ryan for their financial support during the final stage of this work.

TABLE OF CONTENTS

DEDICATION	i
ACKNOWLEDGEMENTS	ii
LIST OF TABLE	viii
LIST OF FIGURE	ix
ABSTRACT	xii

PART I

DYNAMIC PROCESSES ON ARCS3

INTRODUCTION	1
1. R29015 FLIGHT OVERVIEW	6
1.1 Review of Ionospheric Study	6
1.2 Some Active Ion Beam Experiments	8
1.3 Particle Observations	13
2. GEOMETRIC CONFIGURATIONS	17
2.1 Separation Direction	18
2.2 Main Payload Acceleration	20
2.3 Instrument Coordinates in GM Frame	36
3. METHODS OF DATA ANALYSES	38
3.1 DCE Field Determination	38
3.2 Directional Response of OCTO Detectors	47

3.3 Evolution of Ion Beam	56
3.4 Density and Flux of Argon Ions	67

PART II

**ARTIFICIAL ION BEAM AND KINETIC THEORY
OF PLASMA THERMAL FLUCTUATIONS**

INTRODUCTION	70
4. GENERAL THEORY OF THERMAL FLUCTUATIONS	74
4.1 Thermal Velocity And Temperature	74
4.2 Test Charge and Fluctuations	76
4.3 Klimontovich Distribution function	83
4.4 Single/Two Particle Distribution Functions	84
4.5 Static and Dynamic Form Factors	86
5. FLUCTUATIONS OF MAGNETIZED SPECIES	91
5.1 Power Spectrum of Charge Density	91
5.2 Longitudinal Dielectric Function	94
6. FLUCTUATIONS OF UNMAGNETIZED SPECIES	99
6.1 Power Spectrum of Charge Density	99
6.2 Longitudinal Dielectric Function	101
6.3 Temperature Transformation	104
Summary	107
7. ACOUSTIC WAVES AND FLUCTUATIONS	109

7.1 Isofrequency Contours	110
7.2 Fluctuations of O^+ Acoustic Wave	113
8. EIC Waves, Biybrid Waves and Instability	123
8.1 Observations of EIC Waves	123
8.2 Correlations between EIC Waves and Beams	128
8.3 $O^+ - He^+$ Biybrid Wave and Instability	139
Summary and Conclusions	145
Discussions	147

Appendix

A: TRANSFORMATIONS FROM ROCKET TO GM FRAME	148
A.1 The Coordinate Systems	148
A.2 The Rocket Frame	149
A.3 The Local Geographic Frame	149
A.4 The Local Geomagnetic Frame	152
A.5 Transforms between Frames	152
B: CONIC STRUCTURE OF BEAM	157
B.1 Diamagnetism of Plasma	157
B.2 Single Ion Trajectory	157
B.3 Conic Structure of Beam	161
C: ARGON BEAM SIMULATION	163
C.1 Beam Expansion	163
C.2 Density Weighting Function	166

C.3 Generating Ion Distributions	169
D: TRANSFORM FROM u FRAME TO k FRAME	172
BIBLIOGRAPHY	175

LIST OF TABLE

Table 1-1	Rockets Flight Schedule	10
Table 1-2	The Instruments and Ion Source	11
Table 1-3	The Instruments on ARCS3	12
Table 2-1	ARCS3 Guns Operation Schedule	25
Table 2-2	Corrected Separation Distance (Pollock)	26
Table 2-3	Real ACS Corrected Separation Distance	35
Table 2-4	Coordinates of Instruments in Rocket Frame	36
Table 3-1	Corrected Electric Field	46
Table 3-2	Direction of OCTO Detectors	50
Table 3-3	Reference Time and Spin Rate	59
Table 3-4	Argon Beam Density and Flux	68
Table 7-1	Argon Density Near The Gun	113
Table 7-2	Power Spectrum of Electric Field Fluctuations of 4.5ev e^- , $(mV/M)^2$	121
Table 7-3	O^+ -Acoustic Wave Growth Lengths	122

LIST OF FIGURE

Fig. 1-1	Configuration of Instruments on ARCS3	9
Fig. 1-2	Pitch Angle Integrated Ion Flux Profiles	15
Fig. 1-3	Energy Integrated Ion Flux Profiles	16
Fig. 2-1a	ACS Gas Release (130s - 140s)	22
Fig. 2-1b	ACS Gas Release (190s - 200s)	23
Fig. 2-1c	ACS Force Acting on the Rocket	28
Fig. 2-2a	Main payload Acceleration	31
Fig. 2-2b	Main payload Acceleration (smoothed)	32
Fig. 2-3a	Separation Distances (up to 170s)	33
Fig. 2-3b	Separation Distances (up to 600s)	34
Fig. 3-1	Vector M and Spin Plane Component of the E Field	40
Fig. 3-2	Spin Axis, Vectors \hat{M} and $\hat{\epsilon}$ in LGM System	41
Fig. 3-3	Projection of \hat{s} and \hat{M} on LGM Horizontal Plane	41
Fig. 3-4	Spin plane Component of DCE Field Measurement, 410s	44
Fig. 3-5	Counting Rates of OCTO4, 410.1-410.9s	49
Fig. 3-6	Ion Tracing Trajectory, 410.402s	52
Fig. 3-7a	Directional Response of OCTO4, 410.322-410.399s	53
Fig. 3-7b	Directional Response of OCTO4, 410.425-410.502s	54
Fig. 3-8	Sub-magnetometer Data and Reference Time,(a,b)	60
Fig. 3-9	Sub-magnetometer Data and Reference Time,(c,d)	61
Fig. 3-10	Ion Beam Evolution, 2_{\perp}	63
Fig. 3-11	Ion Beam Evolution, 4_{\perp}	64

Fig. 3-12	Ion Beam Evolution, 1_{\perp} to 4_{\perp}	65
Fig. 3-13	Ion Beam Evolution, 5_{\perp} to 8_{\perp}	66
Fig. 4-1	Measured Spectral Density	72
Fig. 7-1	The Isofrequency Integration Contour	112
Fig. 7-2	The Argon Beam Open Angle	112
Fig. 7-3a	Dielectric Function , 3.0ev e^{-} , O^{+} Ion Acoustic Mode	115
Fig. 7-3b	Dielectric Function , 4.5ev e^{-} , O^{+} Ion Acoustic Mode	116
Fig. 7-4a	Isfrequency Contour of O^{+} Ion Acoustic Wave Mode, Azu from 0° to 89°	117
Fig. 7-4b	Isfrequency Contour of O^{+} Ion Acoustic Wave Mode, Azu from 90° to 180°	118
Fig. 8-1	Dynamic Spectrum of ACE Field, 110-220	125
Fig. 8-2	Dynamic Spectrum of ACE Field, 240-400	126
Fig. 8-3	Dynamic Spectrum of ACE Field, 410-550	127
Fig. 8-4a	Fourier Spectra of Wide Freq. Band, 188.95-190.03s .	130
Fig. 8-4b	Fourier Spectra of Wide Freq. Band, 193.99-195.31s .	131
Fig. 8-5a	Fourier Spectra of Low Freq. Band, 187.-192.s	132
Fig. 8-5b	Fourier Spectra of Low Freq. Band, 300.-302.	133
Fig. 8-6	Comparison of Bursts, Low Freq. Wave and Beams . .	134
Fig. 8-7a	Fourier Spectra of Low Freq. Band, 203.-208.s	137
Fig. 8-7b	Beam Density and Flux, 205.74-206.78	138
Fig. 8-8a	Dielectric Function , 1% He^{+} , $O^{+} - He^{+}$ Byhibrid Mode	141
Fig. 8-8b	Dielectric Function , 10% He^{+} , $O^{+} - He^{+}$ Byhibrid Mode	142
Fig. 8-9	Isfrequency Contour of $O^{+} - He^{+}$, Byhibrid Wave Mode	144
Fig. A-1	The Rocket Frame	150
Fig. A-2	The Local Geographic Frame	150

Fig. A-3	The Local Geomagnetic System	151
Fig. A-4	The Global Geographic System	151
Fig. A-5	B Field in LGG Frame	154
Fig. A-6	Projection of B on Horizontal Plane	154
Fig. B-1	Centripetal Motion of Particles in B Field	160
Fig. B-2	Ion Trajectory in LGM System	160
Fig. B-3	Conic Structure of the Beam	160
Fig. C-1	Beam expansion	165
Fig. C-2	Beam Density Distributions	171
Fig. D-1	Relationship between k , u and B Frames	174

ABSTRACT

DYNAMIC PROCESSES AND KINETIC THEORY OF PLASMA FLUCTUATIONS: ARCS3

by

Keyun Tang

University of New Hampshire, December 1988

Dynamic processes on the ARCS3 flight involve six related coordinate systems: Rocket System, Local Geographic System, Local Geomagnetic System, Global Geographic System, Wave Vector System and Artificial Argon Beam System. The present thesis has found the relationships needed to carry out coordinate transformations between all these six coordinate systems. These coordinate transformations are used to investigate ion trajectories and the directional response of the detector OCTO4. A technique to calculate the 3 - component acceleration of the main payload was completed, and the trajectory of the main payload relative to the sub payload was given. A method to use the measured spin plane component of the electric field to construct the full 3 dimensional electric field vector in the Local Geomagnetic System has been provided. A model to simulate the artificial argon beam distribution is proposed, and used to calculate the beam's flux, density and evolution.

Several kinds of plasma waves were observed by the University of Minnesota ACE detector. To explain the wave observations, a kinetic theory

of plasma fluctuations was developed. This theory includes magnetized plasma species with or without parallel streaming. It is also valid for plasma including an unmagnetized two temperature plasma species that is streaming in any direction. As an application of the theory, the thermal fluctuations of the O^+ acoustic wave mode was calculated and compared with observations. The $O^+ - He^+$ bihybrid mode is also evaluated and compared with the observed wave spectra..

Part I

Dynamic Processes on ARCS III

INTRODUCTION

As one of the most useful means to study the ionosphere and magnetosphere, sounding rocket flights can be used to measure the composition, density and temperature of each ionospheric component. Rockets also are used to study dynamic processes in ionosphere, including particle diffusion, formation of the ionospheric electromagnetic fields and particle motion in this field. The sounding rocket - R29015 or ARCS3 (Auroral Rocket for Controlled Studies 3), which we have been studying for three years now, carried two argon ion guns which were located on a separable sub-payload and some particle detectors, wave detectors, electric and magnetic field detectors which were located on the main payload. The most interesting observations are the argon beam's counting rates, directional distributions and plasma waves associated with the argon beam firing. The argon particles were measured by the OCTO and HEEPS detectors supplied by the University of New Hampshire. The wave data were obtained by the auto gain controlled AC and DC electric field detectors supplied by the University of Minnesota. So the ARCS3 rocket is actually a plasma laboratory moved to the ionosphere more than it is a space vehicle sent to study the natural ionospheric environment.

Since the ARCS3 flight on February 10, 1985, several papers were published. The major observations of ARCS3 flight were concentrated in two Ph.D. theses. R. Erlandson of the University of Minnesota under the advisorship of Professor L. Cahill, wrote a thesis entitled *PLASMA WAVES GENERATED DURING AN ARTIFICIAL ARGON ION BEAM EXPERIMENT IN THE IONOSPHERE* which was completed in 1986; C. Pollock of the University of New Hampshire under the advisorship of Professor R. Arnoldy, wrote a thesis entitled *ROCKET - BORNE LOW ENERGY ION MEASUREMENTS IN SPACE* which was completed in 1987. Erlandson's thesis described the design of the rocket main payload, sub payload, and artificial argon ion beam generation system, including the operation principles of the beam guns. His thesis also described the particle detectors, wave receivers, and especially the electric and magnetic field fluctuation signals for each perpendicular and parallel plasma release event in detail. His thesis discussed the possible wave modes and plasma heating. Pollock's thesis gave a systematic review of magnetospheric physics and ion beam physics. His thesis described a new particle detector - HEEPS. The description includes the operation principles, design, energy calibration, and angular calibration of HEEPS. His thesis presented particle observations made by the OCTO detectors and the HEEPS detectors. He presented the observations, including all 9 perpendicular events and 8 parallel events, as functions of time, energy, pitch angle, and azimuthal angle. He gave also a system transformation by using Goldstein xyz convention.

Although these two theses and other papers have done many great works on the ARCS3 flight, many questions are still left to be answered. For example:

1. What is the actual trajectory followed by the sub payload as it separated from the main payload,
2. why do the OCTO particle detectors receive high particle fluxes at certain times,
3. how can DC electric field data received by the DCE receiver on the rocket be converted into the local geomagnetic coordinate system? This electric field magnitude and direction are needed to calculate the $\mathbf{E} \times \mathbf{B}$ drift, which is especially important for low energy particles.
4. What mechanism produced the electric field noise measured?
5. Why can we see many peaks and also a smooth noise background? What is the actual wave mode for each peak and the background in the electric field wave data?

Actually these questions can be sorted into two categories: one concerns the relative positions, directions of the detectors and particles, another one is about the mechanism that produces the waves. In order to answer the first group of questions, we need a physical model and mathematical method to calculate trajectories of particles and instrument orbits in a moving geomagnetic coordinate system as accurately as possible. For the second group of questions, we need an expanded or new kinetic theory of plasma fluctuations which is valid for a plasma including an unmagnetized two temperature beam streaming in an arbitrary direction, such as the artificial argon ion beam.

The thesis being presented here is based on the particle and wave observations discussed previously by Erlandson and Pollock. We have carried out a series of analytic and numerical calculations involving particle motion and wave production. This thesis consists of three parts. The first

part (Chapters 1 to 3) deals with particle dynamic processes on the ARCS3 flight. The second part (Chapters 4 to 8) presents the kinetic theory of plasma fluctuations and its application. The last part is an appendix, that provides several fundamental physics and mathematics methods, which are used in the part I and part II. In Chapter 1, a brief review of ionospheric experiments and the development of ionospheric theory is given. Some instruments and particle observations related to my analysis are listed in Chapter 1 also. In Chapter 2, an independent method to find the relationships between the Rocket system, Global Geographic system, Local Geographic system and Local Geomagnetic system is presented. Based on those relationships, the main payload acceleration and trajectory, and the geomagnetic coordinates of the instruments are calculated. In Chapter 3, several different data analysis methods are provided. They include how to convert two component electric field data measured by the electric field booms into a three component vector in the Local Geomagnetic system, how to evaluate the directional response of the OCTO detectors, a model to simulate the argon ion beam evolution, and a method of calculating the argon ion density. In the second part of this thesis, I checked the general kinetic theory of plasma fluctuations used by D. Sentman and M. Hudson *et al.* and found that I must expand the general fluctuation theory or derive a new treatment that involves an unmagnetized two temperature plasma component streaming in any direction. The emphasis of the second part is to derive an extended kinetic theory and to apply it to plasma wave observations on ARCS3. The derivation is given in Chapters 4, 5 and 6. Chapter 4 gives a general theory of plasma fluctuations; Chapter 5 presents a derivation of fluctuations of unmagnetized species, the

final expressions are in agreement with many classical works; Chapter 6 presents a complete new treatment leading to a kinetic theory of plasma fluctuations of unmagnetized species. In Chapter 7, the application of kinetic theory of plasma fluctuations, a new technique to trace an isofrequency contour of normal modes is given. In Chapter 8, the correlation between EIC waves and argon ion beams is discussed, and $O^+ - He^+$ bihybrid wave modes are calculated and compared with the observations. In Appendix A, a general technique of coordinate transformation from the moving and spinning Rocket frame to the moving Local Geomagnetic system is derived. In Appendix B, the trajectories of artificial argon ions in a magnetic and electric fields are discussed. Based on this, the conic structure of the artificial ion beam is given. In Appendix C, a model to simulate the ion beam's evolution is provided. Appendix D is a technique to complete the transformation from the ion streaming frame (\vec{u}) to the wave vector frame (\vec{k}) frame.

Chapter 1

R29015 FLIGHT OVERVIEW

1.1 Review of Ionospheric Study

The earliest years in experimental studies of the ionosphere extend back to Hertz(1887). His studies were in the microwave region and the wave from the transmitter penetrated the ionosphere without coming back to Earth. In other respects the study extends back to the experiments of Marconi (1899). He received some radio waves at distances far beyond the horizon with intensities greatly exceeding those to be expected from diffraction theory. This fact led to postulates of an ionized reflection region in the upper atmosphere by Kennelly (1902) and Heaviside (1902). Other geophysical phenomena contributing to the concept of the ionosphere were made by geophysicists such as Stewart (1878), Schhuster (1908) and Chapman (1925). However, until the '20's there was no way of experimentally verifying the existence of the ionosphere. The first experiment to verify the existence of the ionosphere was the frequency change-angle of arrival study of Appleton and Barnett (1925). The second, and most extensively used, technique was the pulse method of Breit and Tuve (1926)[A. H. Waynick, 1974].

Until about 1932 people attempted to record a $P'(t)$ curve to show how the virtual height (pulse delay time P') varied with time. From this curve

people developed a method to evaluate the $P'(f)$ curve, which is the curve that shows virtual height as a function of frequency. The instrument used to record the $P'(f)$ curve was the forerunner of the modern 'ionosonde', and the $P'(f)$ curve was called an 'ionogram'[J. A. Ratcliffe, 1974].

After World War II, many wave-interaction experiments were conducted to deduce the electron density profile in the ionosphere, especially in the D-region of the ionosphere, such as those by Huxley *et al.* (1947), Huxley (1948, 1950), Ratcliffe and Shaw (1948), Huxley and Ratcliffe (1949), Fejer and Vice (1959), Flock and Benson (1961), Landmark and Lied (1962), Barrington and Thrane (1962), Weisbrod *et al.* (1964), Smith *et al.* (1965), Thrane *et al.* (1968) and Ferraro, Lee (1968).

Incoherent (Thomson) Scatter Sounding is another powerful means to make measurements in the ionosphere. The first person who believed that incoherent scattering by ionospheric electrons could be detected by modern radio methods was W. E. Gordon (1958). He constructed a parabolic reflector antenna of 1000-foot diameter and coupled it to a high power VHF radar system to detect the back-scattered signals. This method then was used as a means of probing the distribution of electrons throughout the ionosphere, and measuring their temperature T_e (from the Doppler broadening of signals). After this, the first reported detection of incoherent scattering by the ionosphere was made by Bowles (1958, 1961). He made an important discovery that the Doppler broadening of signals was considerably less than expected from the random thermal velocity of the electrons. Other famous incoherent scattering experiments done later include the work of Evans (1962), Pineo (1962), Walker and Spencer (1968), Maynard and DuCharme (1965), Watkins and Sutcliffe (1963), Hey *et*

al., Du Castel *et al.* Misyura *et al.* (1967), Farley (1970) and Evans (1972) [J. V. Evans, 1974].

1.2 Some Active Ion Beam Experiments

In the recent few decades, several kinds of active experiments were performed, such as those using ground based high frequency transmitters, chemical release experiments and artificial ion beam experiments. In this section we will give a brief review of active ion beam experiments, i.e. artificial ion beam experiments which are of most interest to us. Artificial ion beam experiments focus on the evolution of the artificial ion beam in the ionosphere, and the perturbed ion and electron distribution functions and plasma waves caused by the active ion beam. For comparison we list the four recent active experiments with artificial ion beams in the next three tables. The geometric configurations of instruments on ARCS3 rocket shown in Fig. 1-1. A Gyroscope, a 3-axis magnetometer, a low frequency electric field booms, two OCTO ion detectors, a ion drift detector and the HEEPS ion detector were on the main payload of the ARCS3 rocket. Two argon ion guns, a single axis magnetometer, a langmuir probe and a photometer were on the sub payload. The sub-payload was separated from the main payload at 134.4s.

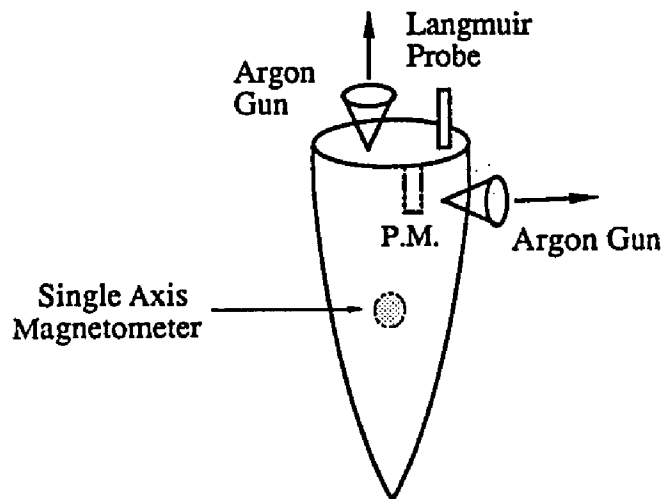
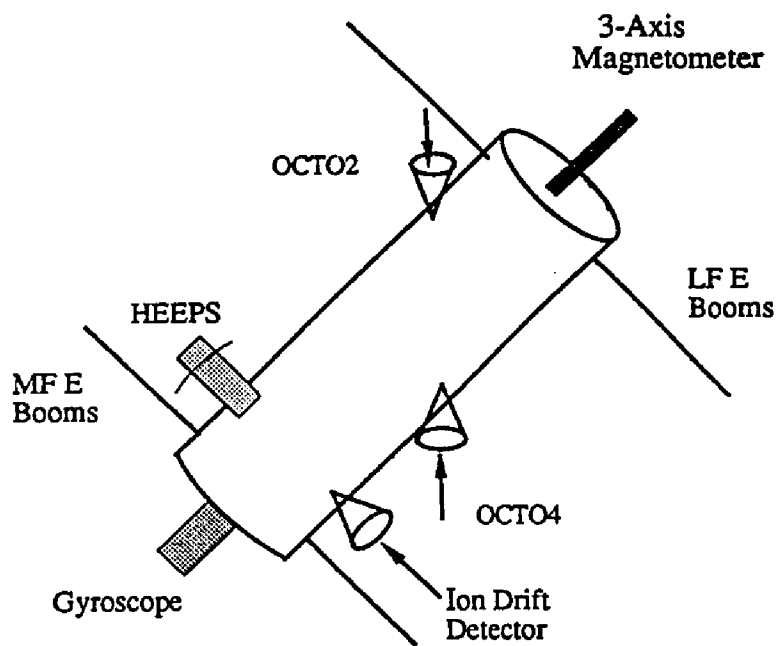


Fig. 1-1 Configuration of Instruments on ARCS3

Table 1-1 Rockets Flight Schedule

Rocket	Collaborators	Location, Time	Sub payloads
Porcupine	MPE,SRI	19, March 1979 Kiruna, SWD	4
	UCB	31, March 1979	4
ARCS1 (R29014)	UNH, UMinn Cornell, NRL	Fairbanks Jan. 1980	no
ARCS2 (R36001)	same as ARCS1	Fairbanks Nov. 1982	one
ARCS3 (R29015)	same as ARCS1,2	SSF, Greenland Feb. 1985	one

MPE : Max - Plank Institute, West Germany

SRI : Space Research Institute of the Academy of Science, USSR

UCB : University of California at Berkeley

UNH : University of New Hampshire

UMinn: University of Minnesota

Cornell : Cornell University

NRL : Navy Research Lab.

SWD : Sweden

SSF : SondreStrom Fjord, Greenland

Table 1-2 The Instruments and Ion Source

Name	Instruments	Ion Guns	Voltage, Current
Porcupine	RPA	Xe^+ (SRI)	200V,4amp
	Langmuir Probe	Ba^+ (MPE)	
ARCS1	2 IDD, 2 PLP ACE, DCE, $\delta n/n$	Ar^+	60V,100mA
ARCS2	same as ARCS1	Ar^+	60V,100mA
ARCS3	see Table 1-3	Ar^+	200V, 100mA

RPA : Retarding Potential Analyzers

IDD : Ion Drift Detectors

PLP : Pulsed Langmuir Probe

Table 1-3 The Instruments on ARCS3

Instrument	Payload	Operating Range	References
Argon guns gun ⊥ gun	Sub Payload	0.1A beam current 220 ev ions 190 ev ions	Erlandson 1985
Electric field meter	Main Payload	5 to 165 mV/m 0 to 300 Hz	Cahill et al. 1980
Photometer	SPL	0.1 to 300 kR $4278 \pm 25 \text{ \AA}$	Arnoldy and Lewis, 1977
Electric AGC receiver	MPL	0.005 to 5 mV/m 0.2 to 10 kHz	Behm 1982
Electrostatic ion detector OCTO	MPL	$10^4 \rightarrow 10^{10}$ $(\text{cm}^2 - \text{s} - \text{sr} - \text{kev})^{-1}$ 10 eV to 30 kev	Arnoldy et al. 1975
Langmuir probe	SPL	$\pm 3V$ sweep, 3.6/s	Erlandson, 86
Imaging ion detector HEEPS	MPL	$10^9 \rightarrow 10^{13}$ $(\text{cm}^2 - \text{s} - \text{sr} - \text{kev})^{-1}$ 0.3 to 260 ev	Pollock 1986
$\delta n/n, e^-$ density fluctuations	MPL	0.2 to 10 kHz	Kelley and Mozer, 1972
Sweep freq. receiver	MPL	10 to 100 $\mu v/m$ 1 to 10 MHz	Erlandson 1986
Magnetic AGC receiver	MPL	0.005 to 1 nT 0.2 to 10 kHz	Erlandson 1986

*from R. Erlandson *et al.*[1987]

1.3 Particle Observations

There were two kinds of particle detectors on the main payload of flight R29015 (ARCS3), i.e, OCTO's (Octospheric electrostatic analyzers) and HEEPS (Hemispheric Electrostatic Energy and Pitch - angle Spectrometer). Erlandson *et al.* [1987] described the particle observations made by the OCTO detectors, and Pollock *et al.* [1988] described the particle observations made by the HEEPS ion detector. These two papers have given detailed descriptions of ion measurements. In this section I will summarize the principal features of the measurements as related to my analysis.

1. The two OCTO ion detectors were opposite each other, and pointed 45° from the rocket spin axis. They can detect particles arriving within a narrow cone of open angle $\sim 30^\circ$ at any one moment. The HEEPS ion detector contained 64 angular bins, so it accepted simultaneously particles of almost all pitch angles.
2. For the 1st perpendicular event, the ions were detected by both OCTO and HEEPS detectors at all possible pitch angles. The reason is that at this time period when the perpendicular gun was very close to the detector, all particles with different pitch angles could reach the detector. For each perpendicular event, from the 2nd to 6th perpendicular gun firing events, the OCTO and the HEEPS detectors received only one high flux peak near the pitch angle of 90° . From the 7th perpendicular event, the ion fluxes dropped dramatically.
3. For the 1st parallel gun firing event, the HEEPS detector received very high ion fluxes at the pitch angle of 180° . For pitch angles less than 160° , the flux was very low. From the 2nd to 4th parallel gun firing

events, the detectors always received two flux peaks; one was near a pitch angle of 180° , another was near a pitch angle of 90° . From the 5th to 8th parallel gun firing, the pitch angles of ions which received by HEEPS detector distributed very widely, from 90° to 170° .

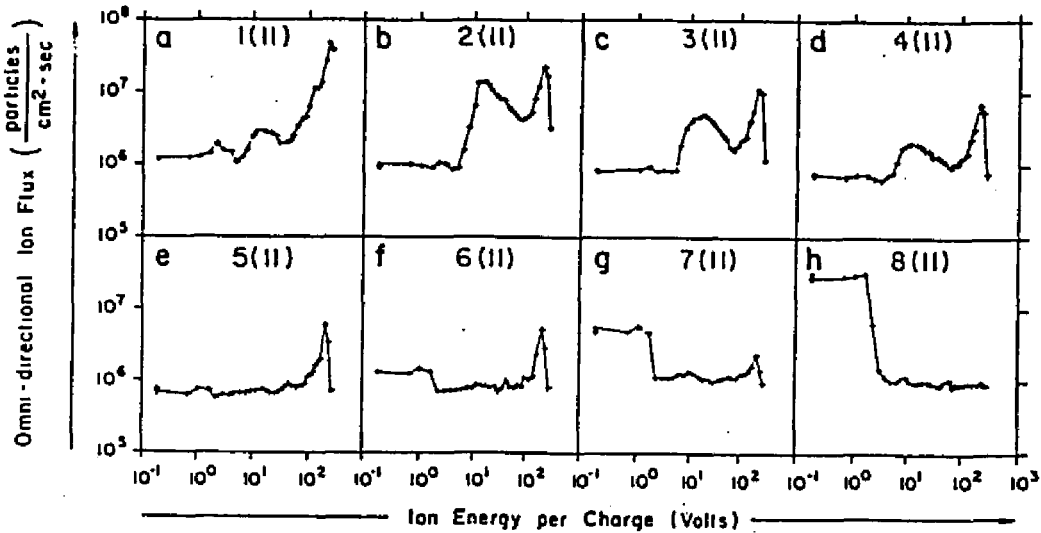
For the 1st to 3rd parallel events, OCTO detectors detected high fluxes near 180° only. From 4th parallel event on, no apparent flux peaks were received by the OCTO detectors.

4. For the first seven parallel events, the major energy peaks were near 200ev. a minor energy peaks were near 15ev for the 2 || to the 4 || events. In comparison, the major energy peaks of the 2 \perp to the 7 \perp events, were near 100ev. There are some 15ev energy peaks for the 1 \perp to 5 \perp events. The magnitudes of the 15ev energy peaks are comparable with those 100ev energy peaks.

The pitch angle integrated ion flux profiles of the HEEPS detector is shown Fig. 1-2 [Pollock *et al.*, 1988]. The flux is plotted logarithmically versus measured ion energy per charge. It is averaged over magnetic azimuth. The energy integrated ion flux profiles of the HEEPS detector is shown Fig. 1-3 [Pollock *et al.*, 1988]. The flux is plotted logarithmically versus measured magnetic pitch angle. It is averaged also over magnetic azimuth.

The observation of two peaks (90° and 180°) for parallel events and one peak for perpendicular events suggested that the artificial Argon beam had a very wide opening angle up to 160° , 170° . The Argon ions with the a pitch angle $\sim 90^\circ$ had longer gyro radii and required longer paths of gyration, so these argon ions had large probability to reach the detectors. That is the reason why the 2nd peaks $\sim 90^\circ$ were received.

PITCH ANGLE INTEGRATED
ION FLUX PROFILES
(Parallel Beam Events)



PITCH ANGLE INTEGRATED
ION FLUX PROFILES
(Perpendicular Beam Events)

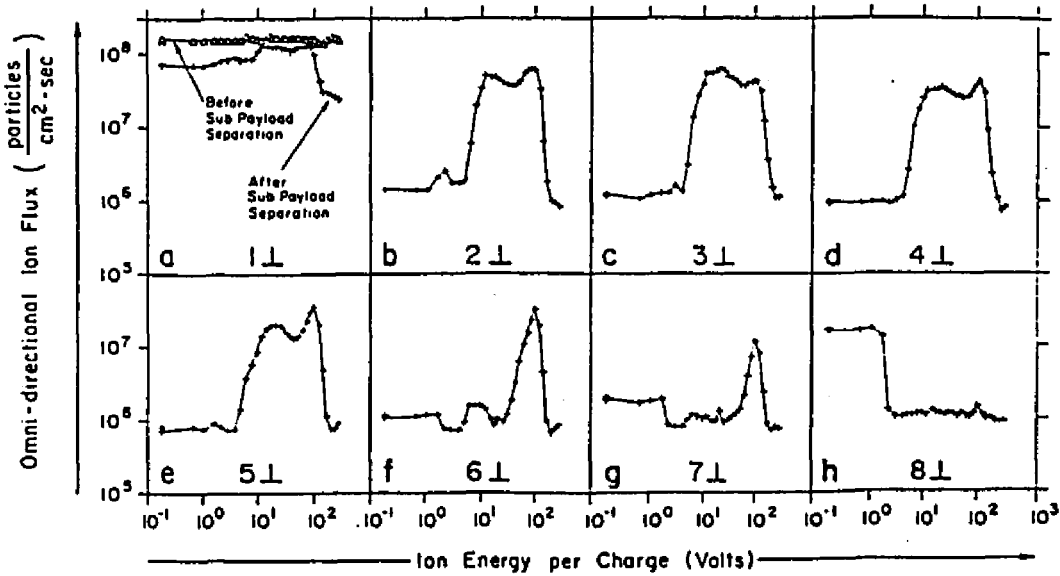
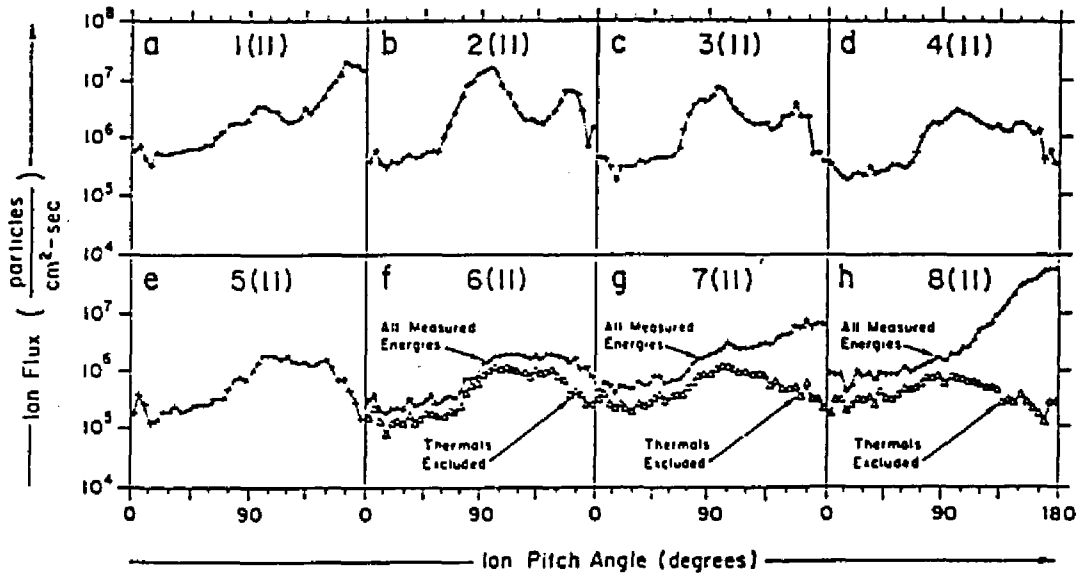


Fig. 1-2 Pitch Angle integrated Ion Flux Profiles

**ENERGY INTEGRATED
ION FLUX PROFILES**
(Parallel Beam Events)



**ENERGY INTEGRATED
ION FLUX PROFILES**
(Perpendicular Beam Events)

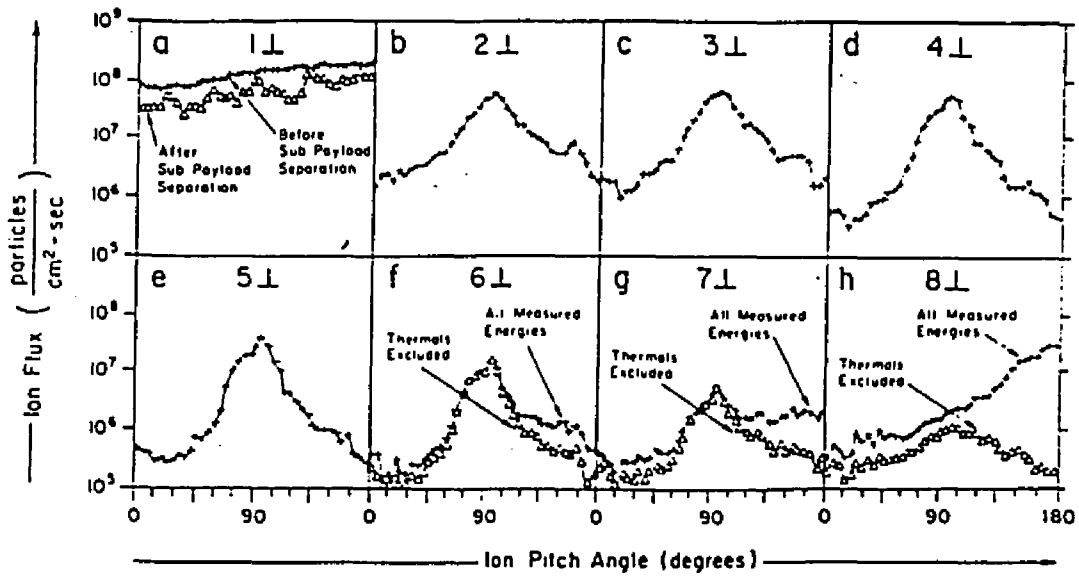


Fig. 1-3 Energy Integrated Ion Flux Profiles

Chapter 2

GEOMETRIC CONFIGURATIONS

The main payload housed a Attitude Control System (ACS) which was used to orient the payloads. About 100 seconds after the launching of the rocket ARCS3, the ACS system began flipping the payload assembly over, in order to deploy the sub payload downward. At 134.4 seconds after the launching the sub payload was ejected at a measured separation velocity of 2.17 m/s. After the separation, the main payload was re-oriented by the ACS gas such that the main payload spin axis formed an angle with B of $\sim 135^\circ$. Before the separation, the two payload together were spinning at a period of $\sim 360ms$. After the separation, the main payload and sub payload were spinning along different direction and at a slight different angular speed.

To study the dynamic processes of the artificial ions and the propagating processes of the plasma waves related to the argon ions, we must know the positions of the ion detectors or wave receivers relative to each ion gun, and we must know the directions of each ion detector, wave receiver and each ion gun. In this chapter, we will calculate the main payload acceleration and trajectory relative to the sub payload by using the ACS data. We will calculate the directions of each instruments on the main payload by using a technique of coordinate transformations which was developed in Appendix A. In chapter 3, the method to determine the direction of the ion guns on the sub payload will be given by using the single axis

magnetometer data. All the calculations which described above will be done in the local Geomagnetic system.

2.1 Separation Direction

In Appendix A, we gave the definitions of four coordinate systems related to rocket motion in the ionosphere. The four coordinate systems are the Rocket system - moving and spinning with the rocket, the Local Geographic system (LGG) - moving with the rocket but not spinning, Local Geomagnetic system (LGM) - moving with the rocket and aligned with the local magnetic field, and the Global Geographic system (GGG). If we know the coordinates of a vector in the Rocket system, R_x, R_y, R_z , then the coordinates of the vector in the Local Geomagnetic system will be

$$\begin{pmatrix} M_x \\ M_y \\ M_z \end{pmatrix} = \mathfrak{R} \begin{pmatrix} R_x \\ R_y \\ R_z \end{pmatrix} \quad (A.9)$$

where the matrixes of the transformations are

$$\mathfrak{R} = \mathfrak{R}_5 \mathfrak{R}_4 \mathfrak{R}_3 \mathfrak{R}_2 \mathfrak{R}_1 \quad (A.5)$$

According to the appendix A.1, where

$$\mathfrak{R}_1 = \begin{pmatrix} \cos \alpha & -\sin \alpha & 0 \\ \sin \alpha & \cos \alpha & 0 \\ 0 & 0 & 1 \end{pmatrix} \quad (A.6)$$

$$\mathfrak{R}_2 = \begin{pmatrix} \cos \beta & 0 & \sin \beta \\ 0 & 1 & 0 \\ -\sin \beta & 0 & \cos \beta \end{pmatrix} \quad (A.7)$$

$$\mathfrak{R}_3 = \begin{pmatrix} 1 & 0 & 0 \\ 0 & \cos \gamma & -\sin \gamma \\ 0 & \sin \gamma & \cos \gamma \end{pmatrix} \quad (A.8)$$

$$\mathfrak{R}_4 = \begin{pmatrix} 1 & 0 & 0 \\ 0 & \cos \delta & \sin \delta \\ 0 & -\sin \delta & \cos \delta \end{pmatrix} \quad (A.9)$$

and

$$\mathfrak{R}_5 = \begin{pmatrix} \cos \psi & 0 & \sin \psi \\ 0 & 1 & 0 \\ -\sin \psi & 0 & \cos \psi \end{pmatrix} \quad (A.10)$$

The angles α, β and the γ are the roll angle, pitch angle and elevation angle of the rocket nose respectively. The angle, $\delta = 40.1^\circ$ is the angle between LGG north and the projection of the local magnetic field \mathbf{B} on horizontal plane as shown in Fig. A-6, and the angle $\psi = 170.27^\circ$ is the angle between LGG zenith and the local \mathbf{B} field. When we have the coordinates of the rocket nose in the LGM system: M_x, M_y, M_z , we can find the pitch and azimuthal angle of the rocket nose in the LGM system:

$$\text{Pitch Angle} = \tan^{-1} \frac{\sqrt{M_y^2 + M_z^2}}{M_x} \quad (2.1)$$

and

$$\text{Azimuthal Angle} = 180^\circ + \tan^{-1} \frac{M_y}{M_x} \quad (2.2)$$

Note, in the LGM system the x axis is defined along the local \mathbf{B} direction, the y axis is defined along LGM East, and the z axis is defined along LGM south. The azimuthal angle in LGM system is measured from LGM North towards LGM West, This is different from the usual definition of azimuthal angle in the LGG system, because the local magnetic field \mathbf{B} is almost opposite to the local zenith. We know the separation time of the

sub payload from the main payload is 134.40s [R. Erlandson, 1986]. At this moment, the directional angles of the rocket nose in the LGG system were:

$$\textit{Elevation Angle} = 272.3^\circ$$

and

$$\textit{Azimuthal Angle} = 328.13^\circ$$

i.e. the rocket nose was almost upside down, pointing to the center of the Earth. According to the formulas (2.1) and (2.2), we calculated that the directional angles of the rocket nose in the LGM system were

$$\textit{Pitch Angle} = 7.457^\circ$$

and

$$\textit{Azimuthal Angle} = 182.54^\circ$$

i.e. the sub payload was almost parallel to the local magnetic field **B** and pointed towards to LGM south at separation time.

2.2 Main Payload Acceleration

In 1986, by using the directional angles of the separation obtained in the last section and the separation speed $\sim 2.17m/s$, we calculated the artificial ion trajectories and the locations of the detectors on the main payload relative to the ion guns located on the sub payload. The results did not match the observations.

For instance, the observations told us that we received high argon ion fluxes only until the 6_{\perp} gun firing, but the calculation said we should receive high argon ion flux until the 8_{\parallel} gun firing. To solve this puzzle R. L. Kaufmann proposed that the main payload was not following the expected trajectory relative to the sub payload. During the flight, some ACS gas pulses were used to control the main payload's direction. Those pulses produced a force on the main payload and resulted in its acceleration. Fig. 2-1a and 2-1b show the ACS pulses during the R29015 flight. We can see that most of the ACS gas came out during the first two perpendicular and parallel events. After 194 sec the ACS gases were almost terminated.

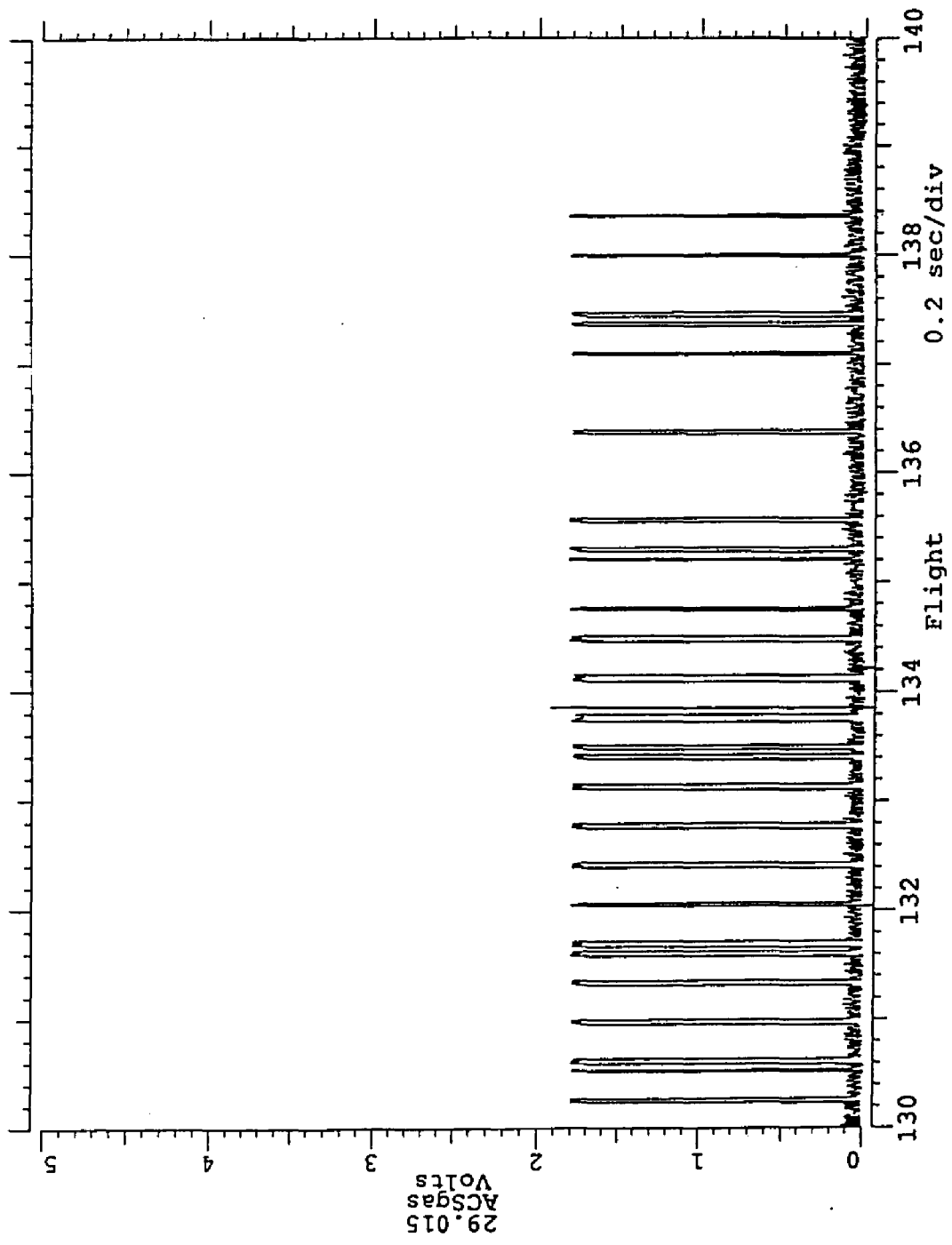


Fig. 2-1a ACS Gas Release (130s - 140s)

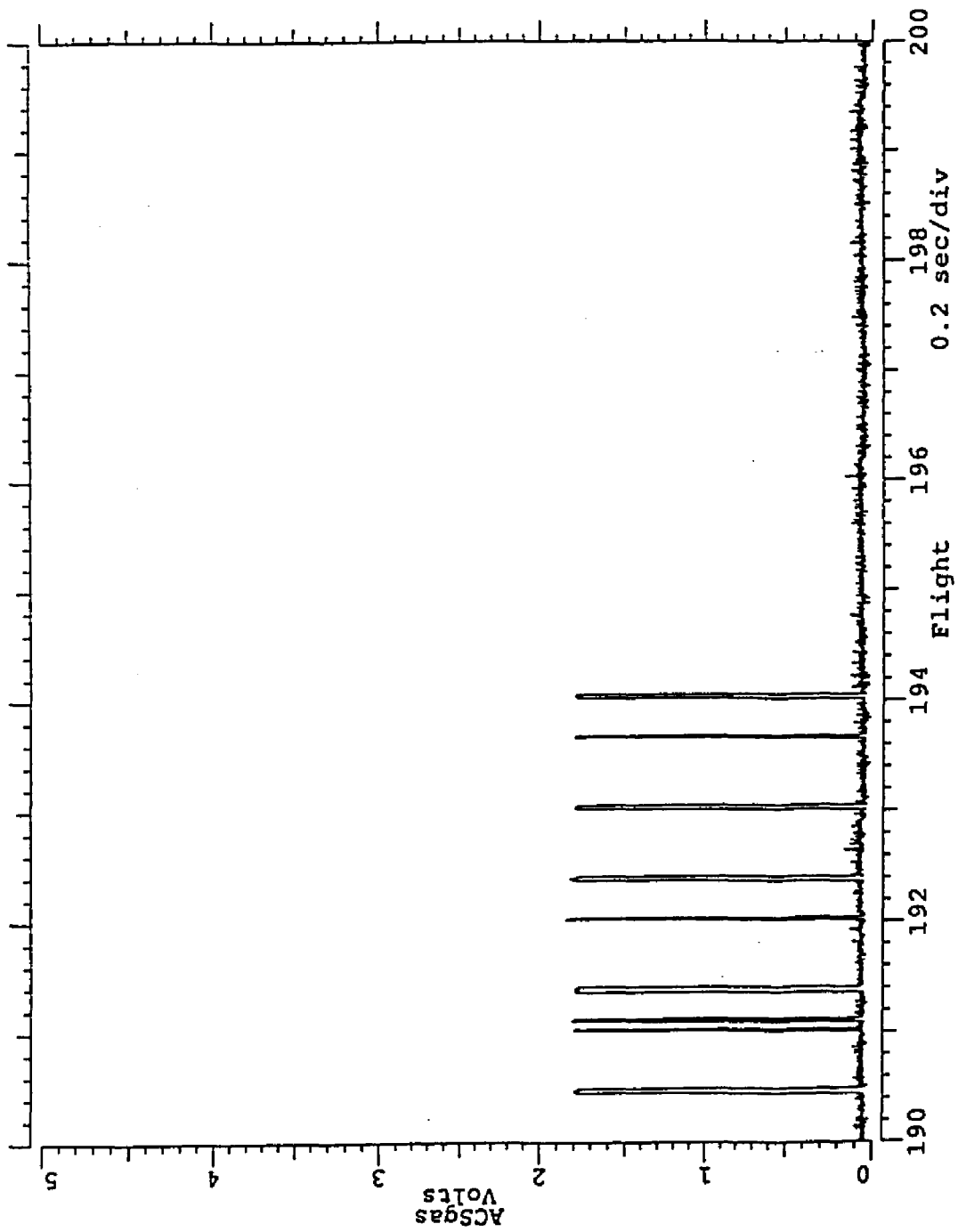


Fig. 2-1b ACS Gas Release (190s - 200s)

Based on this proposal and using the Gyroscope data, C. Pollock developed a model to calculate the acceleration of the main payload. His model was a two dimensional model, i.e. it assumed that the acceleration has only two components on the plane which was passing through the local magnetic field line. In his model, he used an average angular acceleration

$$\begin{cases} \frac{d\alpha}{dt} = 0, & \text{if } t \leq 145s \\ \frac{d\alpha}{dt} = 7.2^\circ, & \text{if } 145s \leq t \leq 163.5s \\ \frac{d\alpha}{dt} = 0, & \text{if } t \geq 163.5s \end{cases} \quad (2.3)$$

where α is the pitch angle of the spin axis. By using this model he calculated the main payload separation relative to the sub-payload shown in Table 2-2 and obtained much better agreement than without ACS acceleration considerations. Table 2-1 shows the original calculation for separation. We can see the results in Table 2-1 and 2-2 are quite different.

Table 2-1 ARCS3 Guns Operation Schedule

Event	On-Off time, s	Separation, m	Altitude, km
1⊥	122.6-150.9	0-36	232-281
1	161.5-178.6	60-97	296-318
2⊥	189.0-206.1	120-158	330-348
2	216.6-233.6	181-218	358-373
3⊥	244.1-261.2	241-279	380-390
3	271.7-288.8	302-340	395-401
4⊥	300.2-316.4	363-400	404-406
4	326.8-344.0	423-461	406-404
5⊥	354.4-371.6	484-522	402-395
5	382.1-399.2	545-583	390-380
6⊥	409.6-426.8	605-643	373-358
6	437.3-454.4	666-704	349-331
7⊥	464.9-482.1	727-765	318-295
7	492.6-509.8	788-826	281-252
8⊥	520.3-537.5	849-887	235-203
8	548.0-565.2	909-948	180-147
9⊥	575.7-592.9	971-1009	123-83

In table 2.1, the separation distances were calculated by R. Erlandson without any acceleration due to the ACS gases.

Table 2-2 Corrected Separation Distance (Pollock)

Event	On-off time, s	Distance, m	⊥ Distance, m
1⊥	122.6-150.9	0-36	0-5
1	161.5-178.6	59-96	12-30
2⊥	189.0-206.1	118-157	42-62
2	216.6-233.6	179-217	74-94
3⊥	244.1-261.2	239-276	106-126
3	271.7-288.8	299-337	138-158
4⊥	300.2-316.4	359-397	170-190
4	326.8-344.0	420-457	203-222
5⊥	354.4-371.6	479-517	235-254
5	382.1-399.2	539-577	267-286
6⊥	409.6-426.8	599-638	299-319
6	437.3-454.4	661-698	330-350
7⊥	464.9-482.1	719-757	363-383
7	492.6-509.8	781-819	395-415
8⊥	520.3-537.5	842-879	428-447
8	548.0-565.2	902-939	460-480
9⊥	575.7-592.9	962-1000	491-512

The || distance means the separation distance along the magnetic field, the ⊥ distance means the separation distance perpendicular to the B direction.

Because Pollock's model considers only two components of the acceleration due to the ACS gas action, and the model used an average angular

acceleration $7.2^\circ/s$ from 145s to 163.4s, it could cause some accumulated error. To verify the validity of the model, I considered all three possible components of the acceleration due to the ACS pulsation and used all gyroscope data from the separation time until the ACS release stopped ($\sim 194.0s$). The basic equation is

$$\mathbf{r} \times \mathbf{F} = I\omega \frac{d\hat{\omega}}{dt} \quad (2.4)$$

where \mathbf{r} is the vector from the mass center of the rocket to the ACS gas valve; $r = 63.5cm$ is the distance from the mass center to the ACS gas valve. \mathbf{F} is the force acting on the rocket as a result of ACS gas (see Fig. 2-1c: ACS Force acting on Rocket). I is the spin moment of inertia of the rocket, $\omega = 17.2rad/s$ is the magnitude of the spin angular velocity, and the $\hat{\omega}$ is the unit vector along the spin axis, i.e.

$$\hat{\omega} \equiv \frac{\vec{\omega}}{\omega}$$

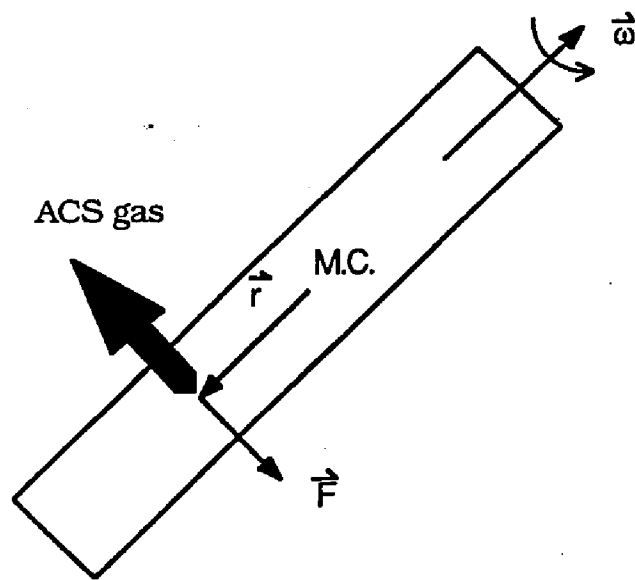


Fig. 2-1c ACS Force Acting on the Rocket

Use \mathbf{r} to cross Eq. (2.4), we have

$$\mathbf{F} = -\frac{I\omega}{r^2} \mathbf{r} \times \frac{d\hat{\omega}}{dt} \quad (2.5a)$$

or

$$\mathbf{F} = \frac{I\omega}{r} \hat{\omega} \times \frac{d\hat{\omega}}{dt} \quad (2.5b)$$

note here $\hat{\omega} = -\mathbf{r}/r$. So the acceleration which was caused by the ACS gas is

$$\mathbf{a} = \frac{I}{m} \frac{\omega}{r} \hat{\omega} \times \frac{d\hat{\omega}}{dt} \quad (2.6)$$

The three components are

$$a_x = \frac{I}{m} \frac{\omega}{r} \left(y \frac{d\hat{\omega}_z}{dt} - z \frac{d\hat{\omega}_y}{dt} \right) \quad (2.7a)$$

$$a_y = -\frac{I}{m} \frac{\omega}{r} \left(x \frac{d\hat{\omega}_z}{dt} - z \frac{d\hat{\omega}_x}{dt} \right) \quad (2.7b)$$

$$a_z = \frac{I}{m} \frac{\omega}{r} \left(x \frac{d\hat{\omega}_y}{dt} - y \frac{d\hat{\omega}_x}{dt} \right) \quad (2.7c)$$

In the calculations, I used $I/m = 1/2R^2 = 178\text{cm}^2$, where $R = 18.87\text{cm}$ is the average radius of the rocket cylinder.

Fig. 2-2a shows the three components of the main payload acceleration which were calculated by using formulas (2.7a), (2.7b) and (2.7c). The top frame shows the LGM south component, the middle shows the LGM East component, the bottom one gives the down component along the local \mathbf{B} direction. Fig. 2-2b shows the same thing after they were smoothed over one rocket spin period ($\sim 0.36\text{s}$). From the above figures we can see the acceleration was mostly along the LGM West direction and that after 168s the acceleration was almost terminated. Figure 2-3a shows the parallel and perpendicular separation distances up to 170s. The time interval from one

time mark to the next is 3 seconds. Figure 2-3b shows the parallel and perpendicular separation distances until 600s. The time interval from one time mark to the next is 30 seconds. In the two figures, the "Down" direction is along the direction of the local geomagnetic field. The "Horz" direction is the direction perpendicular to the local geomagnetic field.

Table 2-3 shows the parallel, perpendicular and total separation distances between the main payload and the sub payload. By comparing Table 2-3 with Table 2-2, we can find that the two sets of perpendicular distances are very close and the sets of parallel distances are a little bit different. However, one difference between the two models of calculation is that not shown here is the separation direction, because the actual number for Pollock's model is not available now. In general, Pollock's model works well.

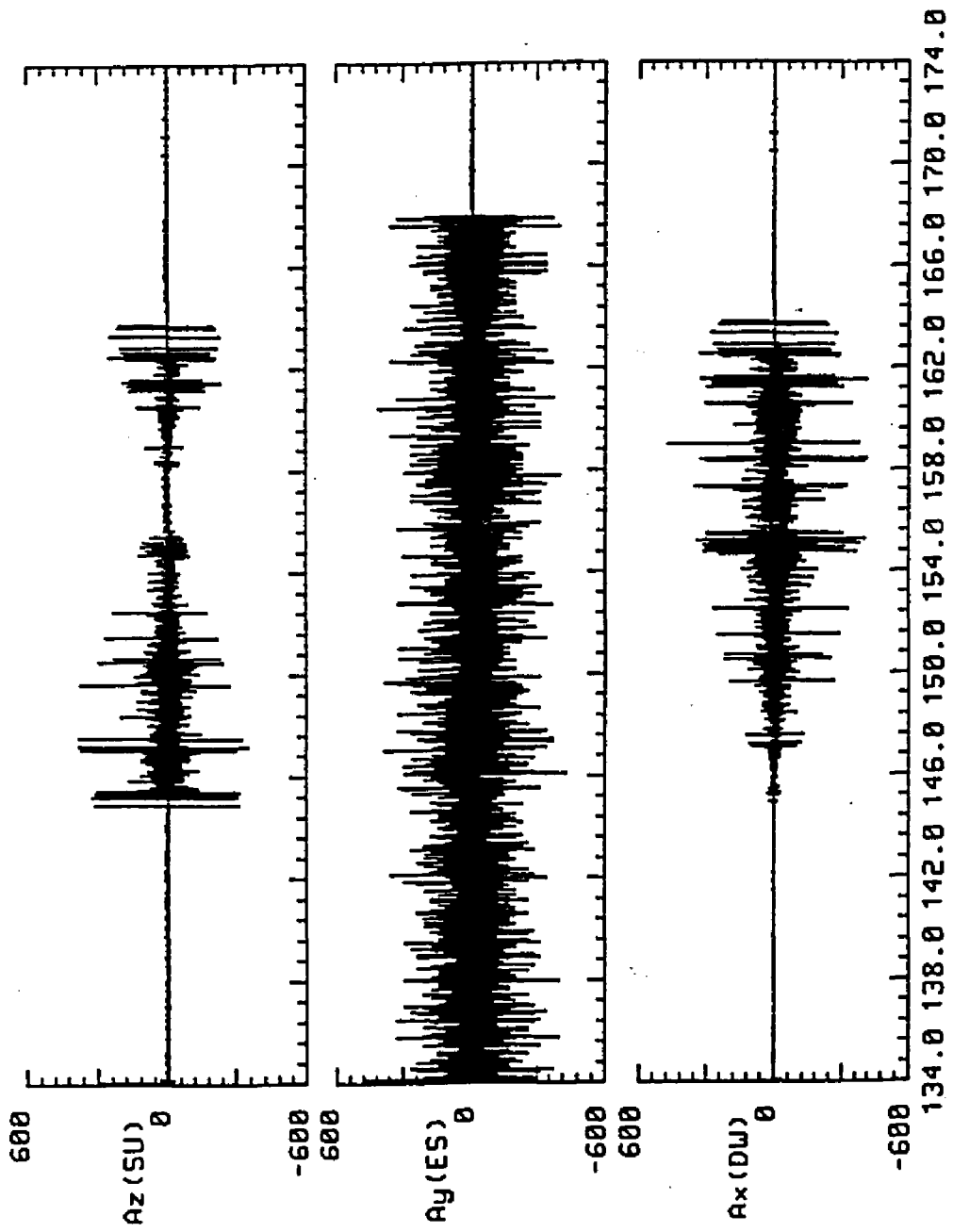


Fig. 2-2a Main payload Acceleration

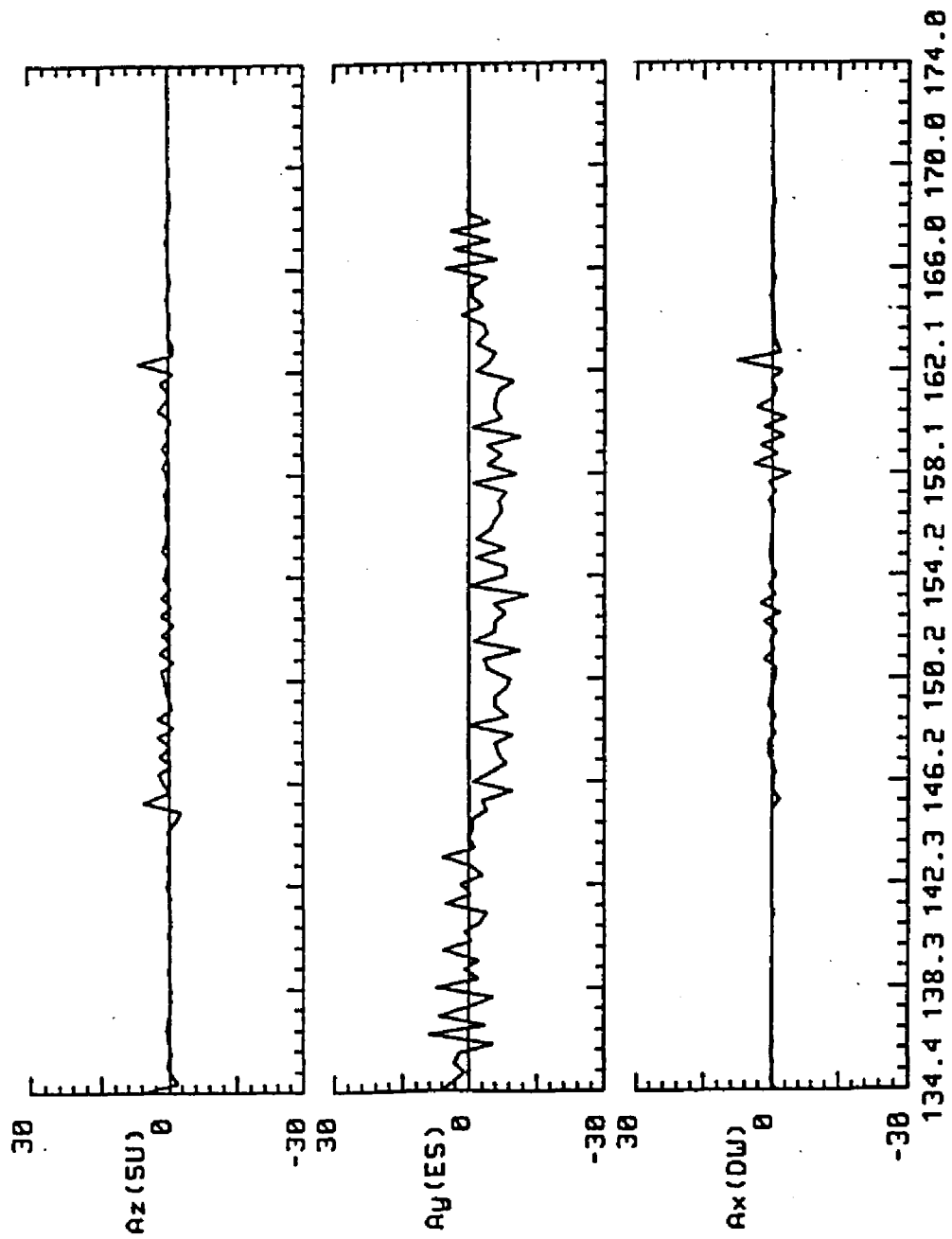
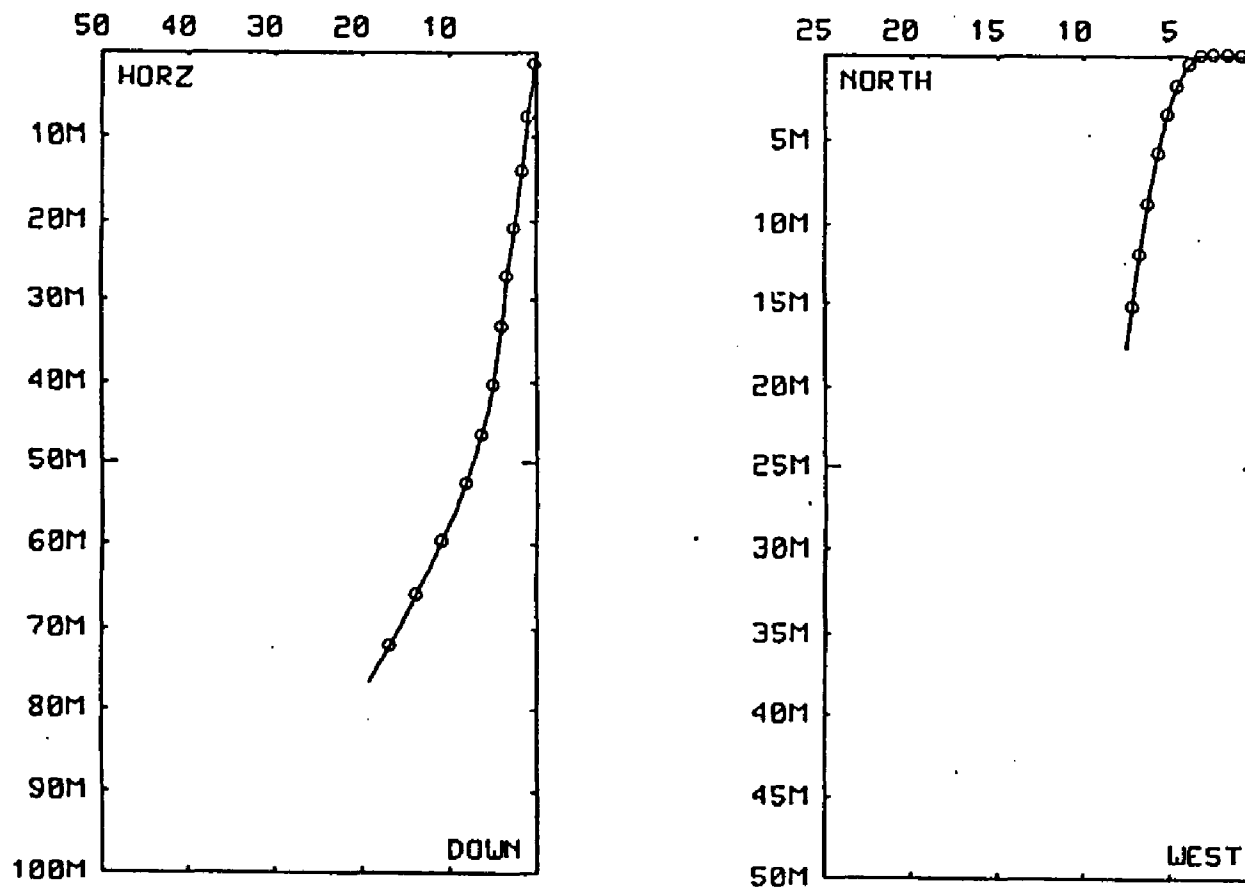


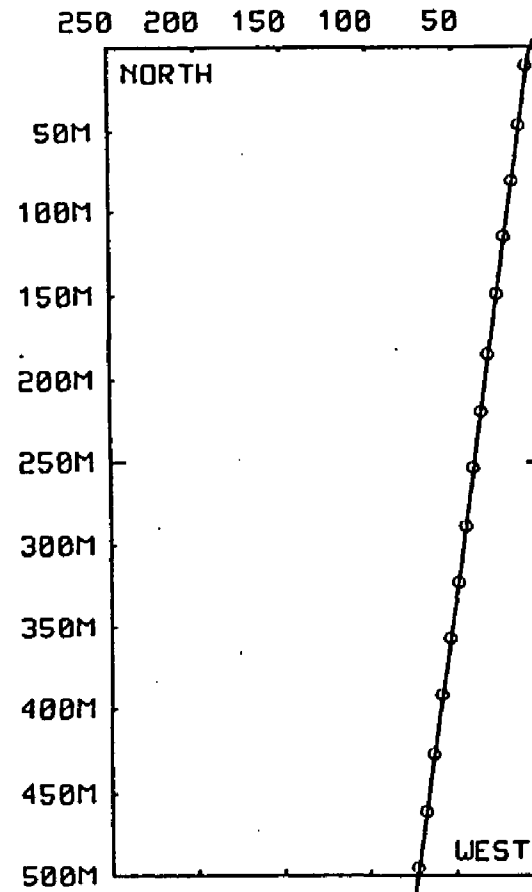
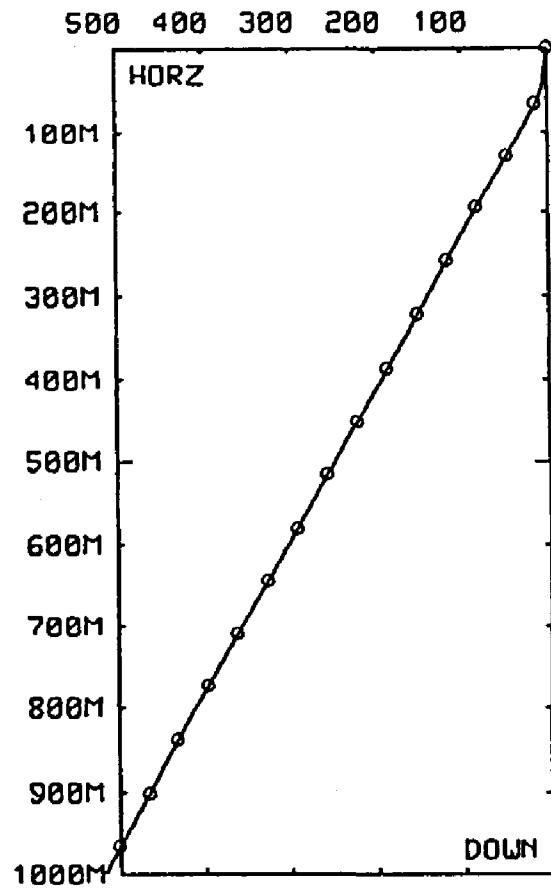
Fig. 2-2b Main payload Acceleration (smoothed)

Fig. 2-3a Separation Distances (up to 170s)



TFINAL = 170. TIME BETWEEN MARKERS = 3 SEC.

Fig. 2-3b Separation Distances (up to 600s)



TFINAL = 600. TIME BETWEEN MARKERS = 30 SEC.

Table 2-3 Real ACS Corrected Separation Distance,m

Event	On-off time, s	Distance	⊥ Distance	Total Distance
1⊥	122.6-150.9	0-36	0-4	0-36
1	161.5-178.6	59-96	11-29	60-100
2⊥	189.0-206.1	118-155	41-61	125-167
2	216.6-233.6	177-214	73-93	192-233
3⊥	244.1-261.2	236-273	105-125	259-300
3	271.7-288.8	296-332	137-157	326-367
4⊥	300.2-316.4	354-391	169-189	393-435
4	326.8-344.0	414-451	201-221	460-502
5⊥	354.4-371.6	473-510	233-253	527-569
5	382.1-399.2	532-569	266-286	595-636
6⊥	409.6-426.8	591-628	298-318	662-704
6	437.3-454.4	651-687	330-350	729-771
7⊥	464.9-482.1	710-747	362-382	797-839
7	492.6-509.8	769-806	394-414	864-906
8⊥	520.3-537.5	829-865	426-446	932-974
8	548.0-565.2	888-925	458-478	999-1041
9⊥	575.7-592.9	947-984	491-511	1067-1109

2.3 Coordinates of Instruments in Rocket Frame

To find the particle positions relative to the instruments on the payloads in LGM system, we must first know the coordinates of the instruments on the payloads in ROCKET frame. Table 2-4 shows the coordinates of the instruments in ROCKET frame. As we defined in appendix A, the z axis is defined along the rocket spin axis toward the nose, the x axis is defined towards the raceway, the y axis is defined according to right hand system, i.e.

$$\hat{y} = \hat{z} \times \hat{x}$$

Table 2-4 Coordinates of Instruments in Rocket Frame

Instruments	x - component	y - component	z - component
OCTO 2	$-\frac{1}{2}$	$\frac{1}{2}$	$-\frac{\sqrt{2}}{2}$
OCTO 4	$\frac{1}{2}$	$-\frac{1}{2}$	$\frac{\sqrt{2}}{2}$
Perp. Gun	1	0	0
Para. Gun	0	0	-1
Sub Magnetometer	$-\frac{1}{2}$	$\frac{1}{2}$	$\frac{\sqrt{2}}{2}$
Boom-	$\frac{\sqrt{2}}{2}$	$-\frac{\sqrt{2}}{2}$	0
Boom+	$-\frac{\sqrt{2}}{2}$	$\frac{\sqrt{2}}{2}$	0

Where the OCTO 2 and OCTO 4 are the two Octospheric electrostatic analyzers, they were opposite each other. The Boom- and Boom+ are the two electric Auto Gain Control receivers, which were also opposite

each other. Both OCTO detectors and Booms were located on the main payload. The perpendicular and parallel plasma guns were located on the sub payload. The sub magnetometer is the single axis magnetometer, which was located on the sub payload. I called it the sub magnetometer to distinguish it from the three axes magnetometer, which was located on the main payload.

Chapter 3

METHODS OF DATA ANALYSES

3.1 DCE Field Determination

As we mentioned before, two electric field antennas (Weitzmann booms) were mounted on the main payload. They were perpendicular to the rocket spin axis on opposite sides of the rocket. The spherical probes at the boom tips were separated by 3 meters from center to center. The DC-E experiment recorded the potential difference between the two spherical probes and derived the magnitude of the electric field along the vector from the positive boom to the negative boom. But these measurements were not the real electric field. They were the component of the real electric field on the spin plane in which the booms rotated. To find the magnitudes and directions of the real electric field, we must convert the two components of the electric field in the spin plane into a three component vector. There were several different ways to do this. Dr. Cahill has used the position of booms relative to the three - axis magnetometer to determine the direction of the electric field. In the LGM coordinate system, however, the relative angles of booms to the three - axis magnetometer are not linear. For example, in the spin plane the X axis of the magnetometer was 45° in front of the negative boom, but the angle between the projections of the X axis of the magnetometer and the negative boom was not a constant. So

it is not accurate to use the relative positions of booms relative the three - axis magnetometer to at one moment as the relative position of the X axis of the magnetometer and the negative boom at that time. My way to convert the spin component of the electric field into the real electric field is to use the "ZERO" position to determine the direction of the electric field.

On the rocket spin plane, I selected a special unit vector \hat{M} . When the negative boom rotates parallel to the vector \hat{M} , the potential difference between the two booms was zero. Of course this unit vector should be perpendicular to the real electric field, i.e.

$$\mathbf{E} \perp \hat{\mathbf{B}}$$

$$\mathbf{E} \perp \hat{\mathbf{M}}$$

or

$$\hat{\epsilon} = \hat{M} \times \hat{B} = -M_x \hat{y} + M_y \hat{z} \quad (3.1)$$

which implies

$$\epsilon_x = 0$$

$$\epsilon_y = -M_x \quad (3.2)$$

$$\epsilon_z = M_y$$

Here $\hat{\epsilon}$ is the unit vector along the electric field, and ϵ_x , ϵ_y , ϵ_z are the three components of the $\hat{\epsilon}$. The relationship between the unit vector \hat{s} along the spin axis, the electric field \mathbf{E} , the spin plane component \mathbf{E}_0 , and the special unit vector \hat{M} are shown in Fig. 3-1.

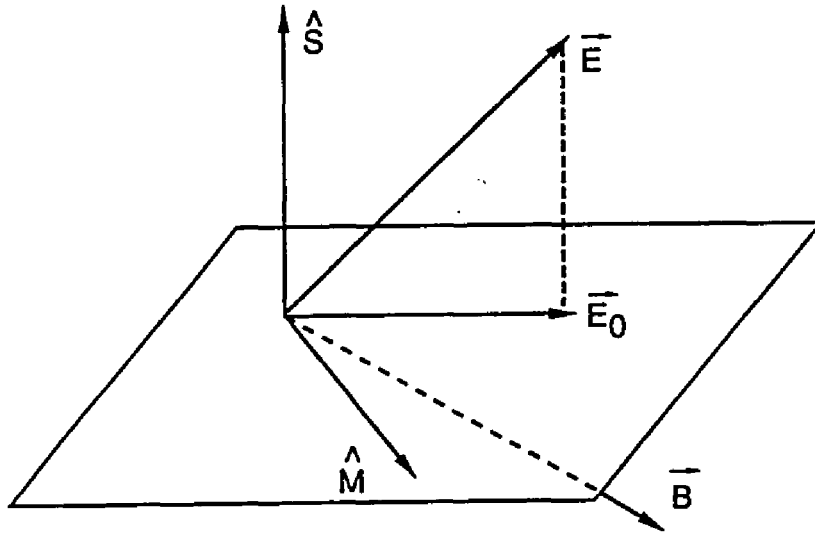


Fig. 3-1 Vector \vec{M} and Spin Plane
Component of the Electric Field

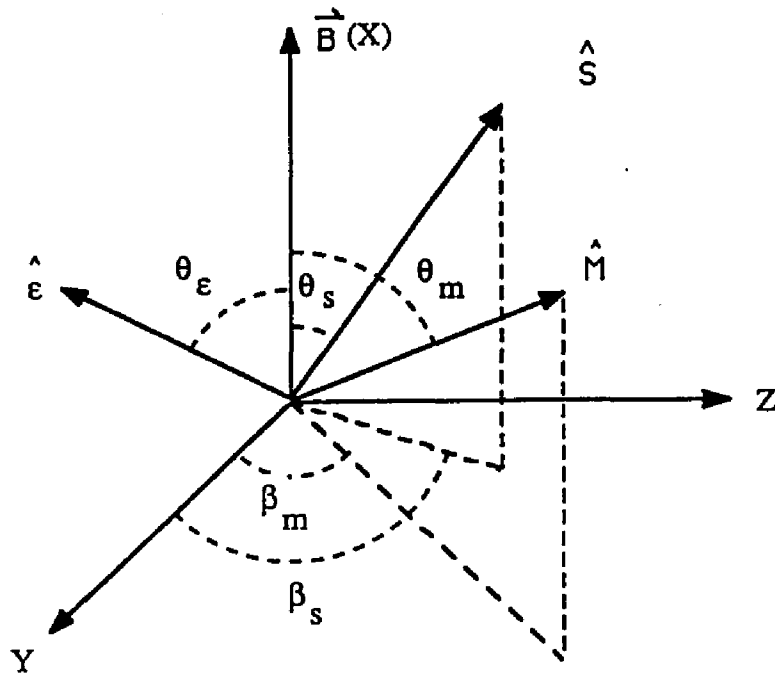


Fig. 3-2 Spin Axis, Vectors M and ϵ in LGM Frame

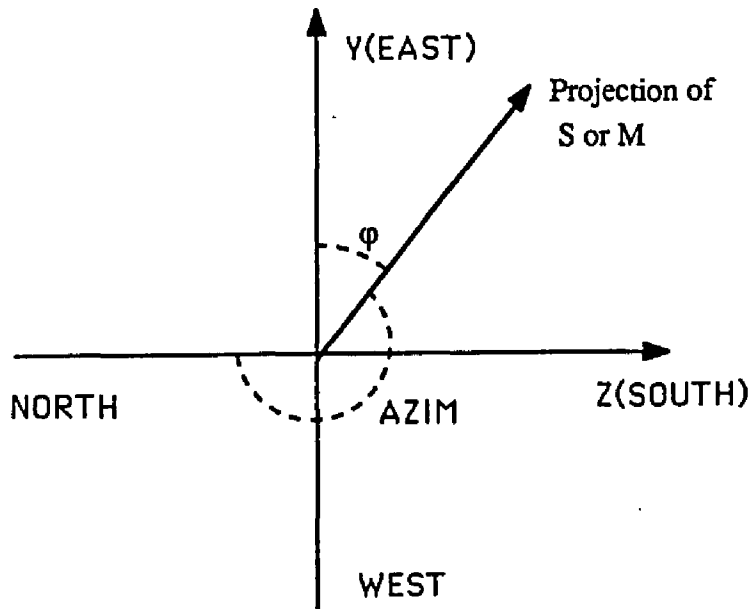


Fig. 3-3 Projection of Vector S or M on LGM Horizontal Plane

We know the spin plane component was the projection of the electric field \mathbf{E} on the spin plane

$$\begin{aligned}\mathbf{E}_0 &= \mathbf{E} - (\mathbf{E} \cdot \hat{s})\hat{s} \\ &= |\mathbf{E}|[\hat{e} - (\hat{e} \cdot \hat{s})\hat{s}]\end{aligned}\quad (3.3)$$

So, the magnitude of the real electric field is

$$\begin{aligned}|\mathbf{E}| &= \frac{|\mathbf{E}_0|}{|\hat{e} - (\hat{e} \cdot \hat{s})\hat{s}|} \\ &= \frac{E_0}{\sqrt{[-(\hat{e} \cdot \hat{s})s_x]^2 + [\epsilon_y - (\hat{e} \cdot \hat{s})s_y]^2 + [\epsilon_x - (\hat{e} \cdot \hat{s})s_z]^2}}\end{aligned}\quad (3.4)$$

where

$$\begin{aligned}s_x &= \cos \theta_s \\ s_y &= \sin \theta_s \cos \phi_s = -\sin \theta_s \sin AZ_s \\ s_z &= \sin \theta_s \sin \phi_s = -\sin \theta_s \cos AZ_s\end{aligned}\quad (3.5)$$

where s_x, s_y, s_z are the three components of the unit vector \hat{s} along the spin axis. Here θ_s, AZ_s are the pitch angle and azimuthal angle of the spin axis respectively, ϕ_s is the angle from the y axis (LGM east) to the z axis (LGM south). Also,

$$\begin{aligned}\epsilon_x &= 0 \\ \epsilon_y &= -M_x = \sin \theta_m \cos AZ_m \\ \epsilon_z &= M_y = -\sin \theta_m \sin AZ_m\end{aligned}\quad (3.6)$$

where θ_m, AZ_m are the pitch and azimuthal angles of the special unit vector \hat{M} defined earlier. The geometric configurations are shown in Fig. 3-2 and 3-3. So,

$$\hat{e} \cdot \hat{s} = -\sin \theta_s \sin AZ_s \sin \theta_m \cos AZ_m + \sin \theta_s \cos AZ_s \sin \theta_m \sin AZ_m \quad (3.7)$$

To evaluate the magnitude of the real electric field \mathbf{E} , substitute (3.5), (3.6) and (3.7) into (3.4). Finally we have the electric field

$$\mathbf{E} = |E|[\epsilon_y \hat{y} + \epsilon_z \hat{z}]$$

Here we again used the assumption that the electric field was perpendicular to the local magnetic field \mathbf{B} .

Now, the only questions left are how to find the E_0 , the magnitude of the spin plane component of the electric field, and how to determine the pitch angle θ_m and azimuthal angle AZ_m of the special unit vector \hat{M} . It is easy to understand that

$$E_0 = (E_{max} - E_{min})/2$$

where E_{max} and E_{min} are the maximum and minimum values of DCE measurements during a complete spin period. To determine the directional angle of the vector \hat{M} , we must use the technique developed in Appendix A and section 2.4. This technique finds the pitch and azimuthal angles of any instrument on the main payload at any time. Let's start out with

$$(E_{max} + E_{min})/2$$

as the "ZERO" point value. This value is not necessarily zero; it could be shifted from zero due to instrumental errors. The second step is to check the corresponding time from the record of the DCE measurements. At this time the DCE measurement equals the value of the "ZERO" point. Then we calculate the pitch angle θ_m and azimuthal angle AZ_m of the negative boom at that moment by using the coordinate transformation technique.

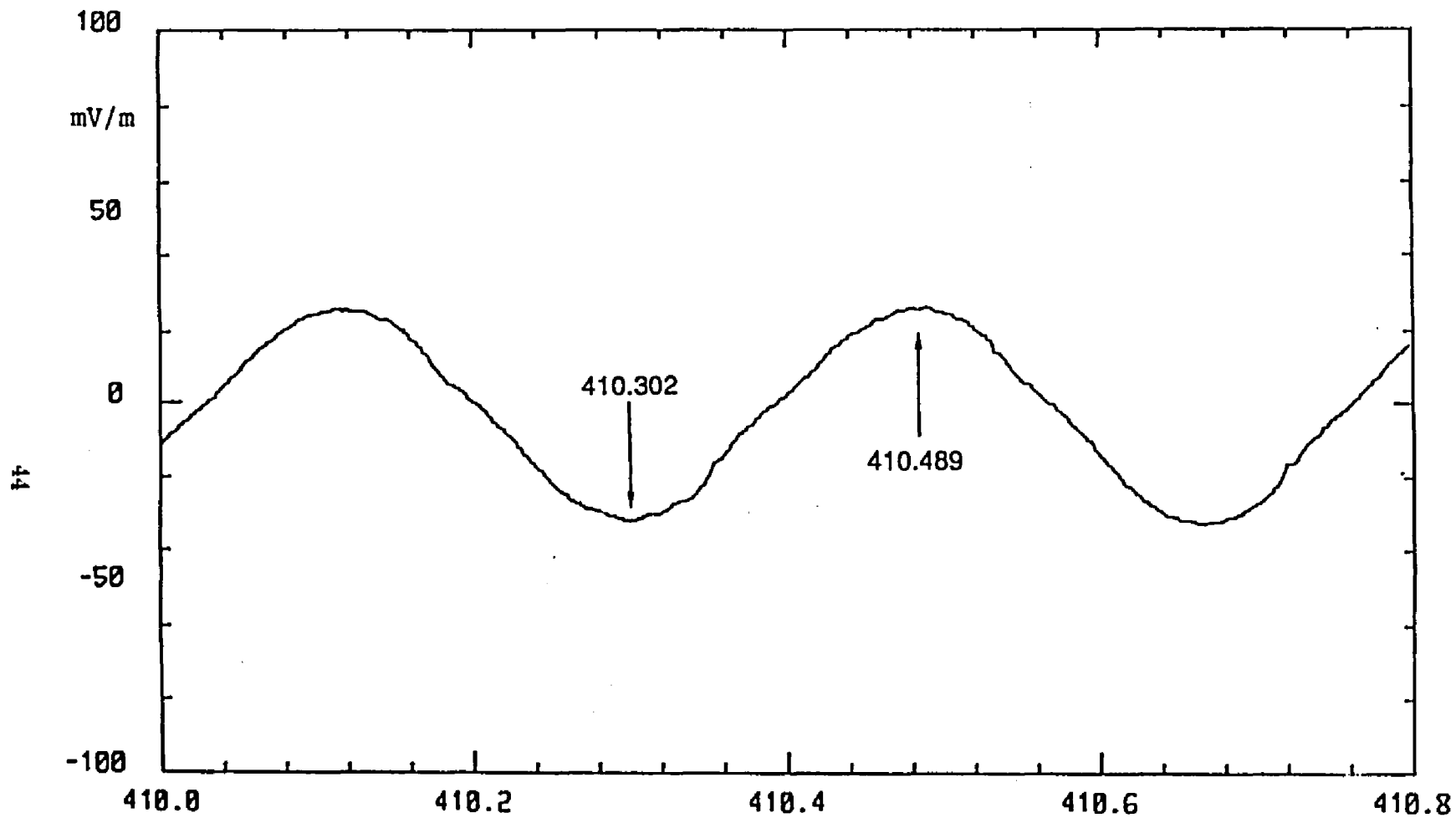


FIG. 3-4 SPIN PLANE COMPONENT OF DCE FIELD

Fig. 3-4 shows an example of how to determine E_0 and θ_m , AZ_m . This figure contains the DCE measurements from 410.0s to 410.8s. I take the first valley on the left as the minimum point, and the next peak to the right as the maximum point. From the printout I have

$$E_{min} = -16.0mV/m \text{ at time } t = 410.3019s$$

and

$$E_{max} = 13.167mV/m \text{ at time } t = 410.4890s$$

So,

$$E_0 = [13.167 - (-16.0)]/2 = 14.58(mV/m)$$

and

$$\text{"ZERO" value} = [13.167 + (-16.0)]/2 = -1.416(mV/m)$$

The printout showed that at $t = 410.385s$, the spin plane component was $\sim -1.416mV/m$. I use the direction of negative boom at $t = 410.385s$ as the direction of the special vector \hat{M} . By using coordinate transformations, I find that, at this moment,

$$\text{Pitch Angle of } \hat{M} = 48.72^\circ$$

and

$$\text{Azimuthal Angle of } \hat{M} = 193.7^\circ$$

By using the technique and procedure described here, I calculated the electric field, including the correction, for 9 different events. The results are shown in Table 3-1.

Table 3-1 Corrected Electric Field, mV/m

Event	Time	Pit/s	Az/s	Pit/m	AZ/m	E_{max}	E_{min}	E_{east}	E_{south}
1	180	137.4	180.5	127.7	33.5	10.2	-5.7	-7.1	4.7
2	189	137.0	181.0	127.9	34.6	12.8	-9.2	-9.8	6.7
3	220	138.3	180.9	104.2	74.2	3.3	-0.8	-0.7	2.6
4	300	135.7	179.9	58.2	230.1	11.2	-10.8	8.4	-10.0
5	340	138.0	179.9	59.7	228.9	15.8	-17.5	12.7	-14.6
6	410	137.8	179.9	48.7	193.7	13.2	-16.0	14.4	-3.5
7	470	138.1	179.4	52.3	211.4	16.5	-26.2	19.5	-11.9
8	500	136.2	177.7	47.0	163.5	15.7	-25.2	19.9	5.9
9	530	138.5	178.2	53.0	209.9	17.7	-31.8	22.9	-13.1

Where Pit/s, AZ/s are the pitch and azimuthal angles of the spin axis, Pit/m, AZ/m are the pitch and azimuthal angles of the special vector \hat{M} . E_{max} , E_{min} are the maximum and minimum values of DCE measurements, and E_{south} , E_{east} are the two components of the real electric field in the LGM system, in units of mV/m .

There is another slightly simpler way to convert the spin plane component of the electric field into the real electric field. It uses the formula

$$\mathbf{E} = \mathbf{E}_0 + \Delta\mathbf{E} \quad (3.8)$$

The magnitude of \mathbf{E}_0 can be found by using the same procedure which was used above. The direction of \mathbf{E}_0 is the direction of the negative boom at the moment the spin component had its maximum value. The vector $\Delta\mathbf{E}$ is parallel to the spin axis and its magnitude is given by

$$\Delta E = E_0 \cot(Pbm) \quad (3.9)$$

where Pbm is the pitch angle of the negative boom at the moment the spin plane component had its maximum value. But due to the pitch angle of the spin axis which was $\sim 135^\circ$ after $140s$, the minimum angle between the electric field and the booms was $\sim 45^\circ$ instead 0° . As a result, more than one boom position corresponded to a maximum DCE measurement, so it is hard to find the accurate position which corresponded to the same azimuthal angle as the real electric field. The earlier method I used may avoid this shortcoming, because in that method we don't need an accurate peak position; we only need the peak and valley values. That is the reason why I use it instead of the latter method.

3.2 Directional Response of OCTO Detectors

OCTO detectors have an opening angle of $20^\circ \times 30^\circ$. We thought that the whole cross section of the OCTO detector could receive the argon beam ions. The calculations show that only small portions of the detector can receive the artificial ions from the Argon gun, and these portions varied with time. The basic method we used in the calculations is to trace ion trajectories back from the detector towards the ion gun. Assume that the detector received a particle in a certain direction with an energy and mass determined by the ion generator. We trace the particle's trajectory back, i.e. use the method we developed in Appendix B to calculate the particle's position and direction at any time. If at any moment the minimum distance from the particle's trajectory to the ion gun is small enough (such as a tenth of a gyro radius of the particle, or 30 meters) and at that moment

the velocity vector of the particle points close enough to the direction of the ion gun (such as the angle between the particle's moving direction and the gun's direction is less than 60°) then we consider that particle could have come from the gun. In other words, we say that the detector at that moment can really receive particles from the artificial ion gun. Otherwise we conclude that no particle entering the detector aperture could have come from the artificial ion gun.

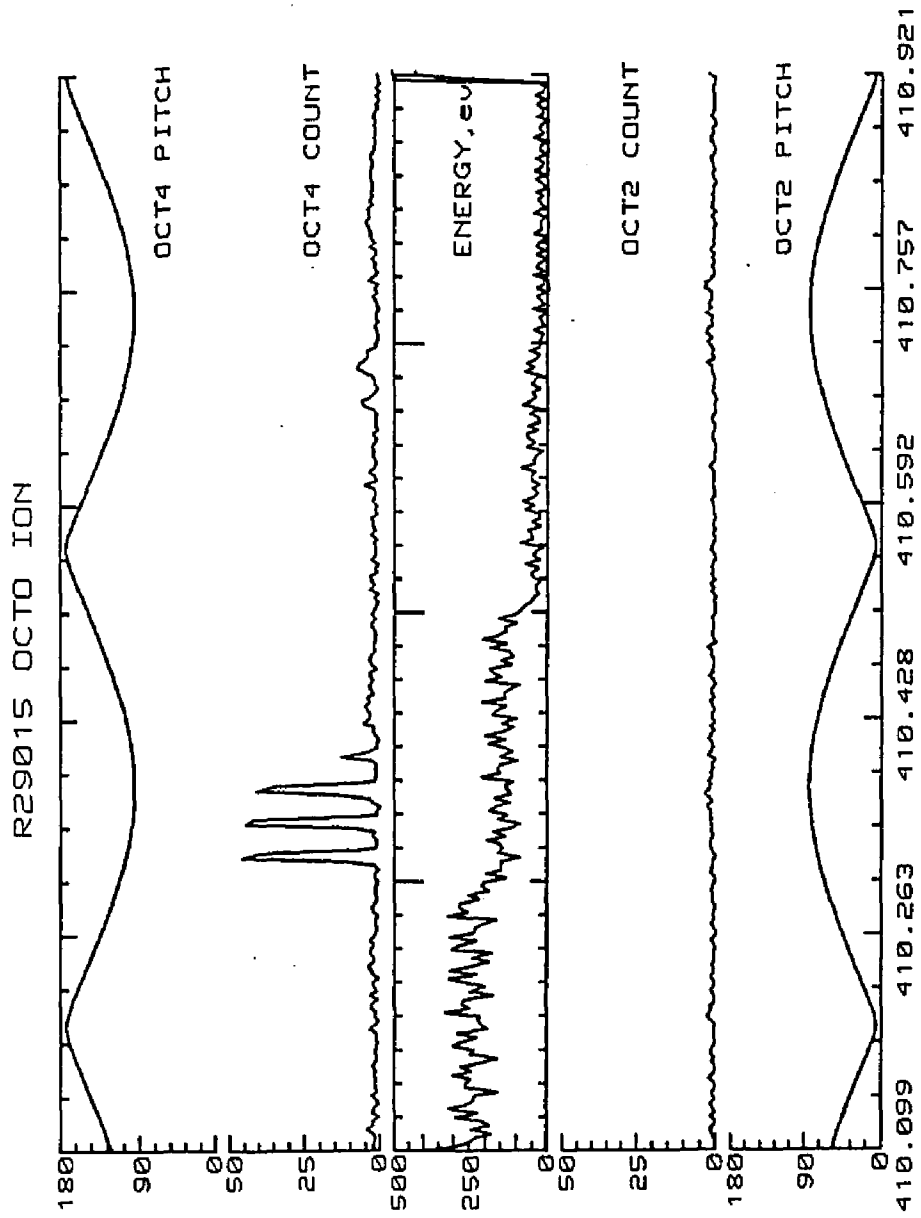


Fig. 3-5 Counting Rates of OCTO4, 410.1-410.9s

Fig. 3-5 shows the pitch angles and the ion counting rates of the two OCTO detectors from 410.1s to 410.92s. The top two patterns show the pitch angle and counting rate of the OCTO4 detector. The middle pattern shows the detectors sweep energies from a few ev to a few hundred ev. The bottom two patterns show the pitch angle and counting rate of the OCTO2 detector. We can see four peaks in the counting rate at $t=410.322s$, $410.348s$, $410.374s$ and $410.399s$. At $t=410.425s$, a lower flux peak can be seen also. At $t=410.451s$, $410.476s$ and $410.502s$, the ion fluxes are very low. At those eight moments, the counts received by the OCTO detectors, and the pitch and azimuthal angles of the center line of the OCTO detectors are listed in Table 3-2.

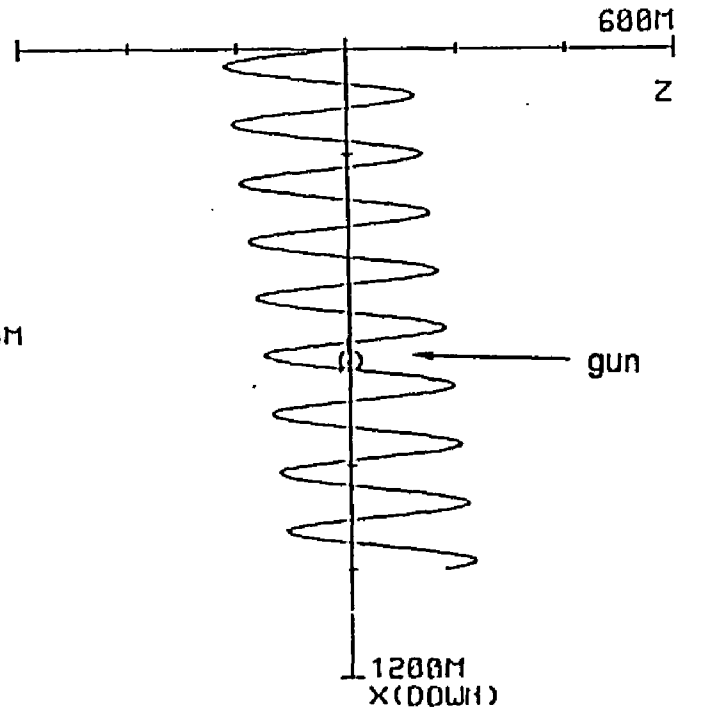
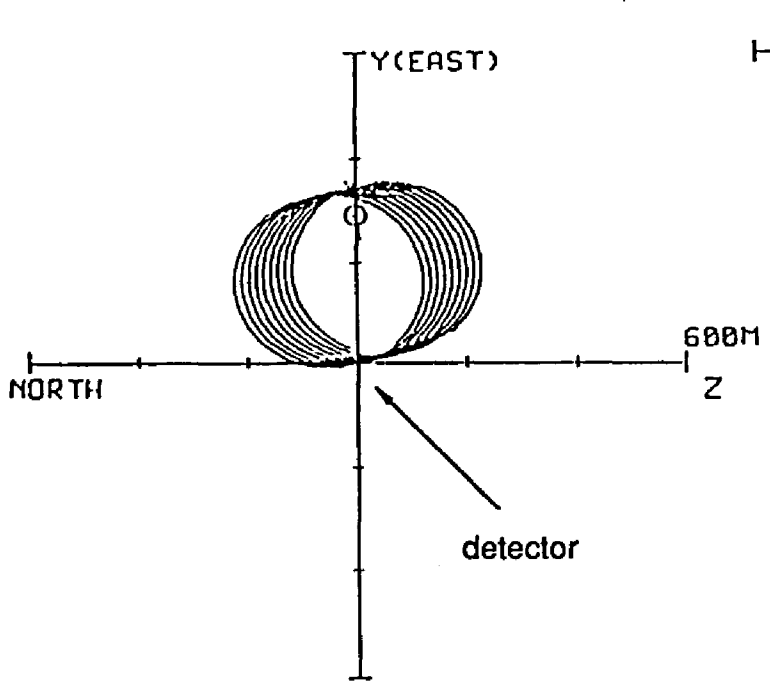
Table 3-2 Direction of OCTO Detectors

Time	OCTO2			OCTO4		
	Counts	Pitch	Azimuth	Counts	Pitch	Azimuth
410.322	0.0	106.0	146	45.6	73.97	214
410.348	1.6	98.8	164	44.7	81.7	196
410.374	2.2	96.1	181	40.6	83.9	179
410.399	2.2	98.1	198	12.8	81.8	162
410.425	0.3	104.8	214	5.9	75.2	146
410.451	1.2	115.1	228	3.1	64.9	132
410.476	1.6	128.1	242	3.1	51.9	118
410.508	0.3	146.6	259	2.8	33.4	101

In this table the pitch angles are from the 3-Axis magnetometer data, the azimuthal angles are calculated by using the coordinate transformation

technique. The directional angle of the ion entering OCTO4 detector along the center line of the OCTO4 at any moment should equal the directional angle of the center line pointing out of OCTO2, because the two detectors were opposite each other. From this table we can see that the OCTO4 detector received high ion fluxes when the pitch angles of the detector were less than 90° but close to 90° . The OCTO2 detector received very low counts at those times. This feature is understandable because the aperture of the OCTO2 detector was not pointing towards to the direction of the artificial ion source. Fig. 3-6 shows the trajectory of the 100eV ions which had same directions as the center line of the OCTO2 detector at detection times. The trajectory included the influence of $\mathbf{E} \times \mathbf{B}$ drifts, where the DC electric field used was $E_{east} = 14.4 \text{ mV/m}$, $E_{north} = 3.5 \text{ mV/m}$, as calculated in section 3.1. Fig. 3-6 shows that the minimum distance from the trajectory to perpendicular ion gun is $\leq 50 \text{ meter}$ and at that position the angles between the direction of the ion and the gun on both $Y - Z$ plane and $X - Z$ plane are $\leq 75^\circ$.

Fig. 3-6 Ion Tracing Trajectory, 410.402s



GEO MAGNETIC SYSTEM, AZIMUTH: NORTH-WEST
 $B=0.5348$ GAUSS, $\Omega=128.893$
 $U(\text{GUN TO ROCKET})=2.17\text{M}$

$E_{\text{east}}=14.40\text{MV/M}$ $E_{\text{south}}=-3.50$
 $\text{ENERGY}=100.\text{eV}$ $U_{\text{ION}}=21887.\text{M/S}$

	TDET	PADET	AZDET	GYRO R
2	410.402	95.969	199.598	16994.

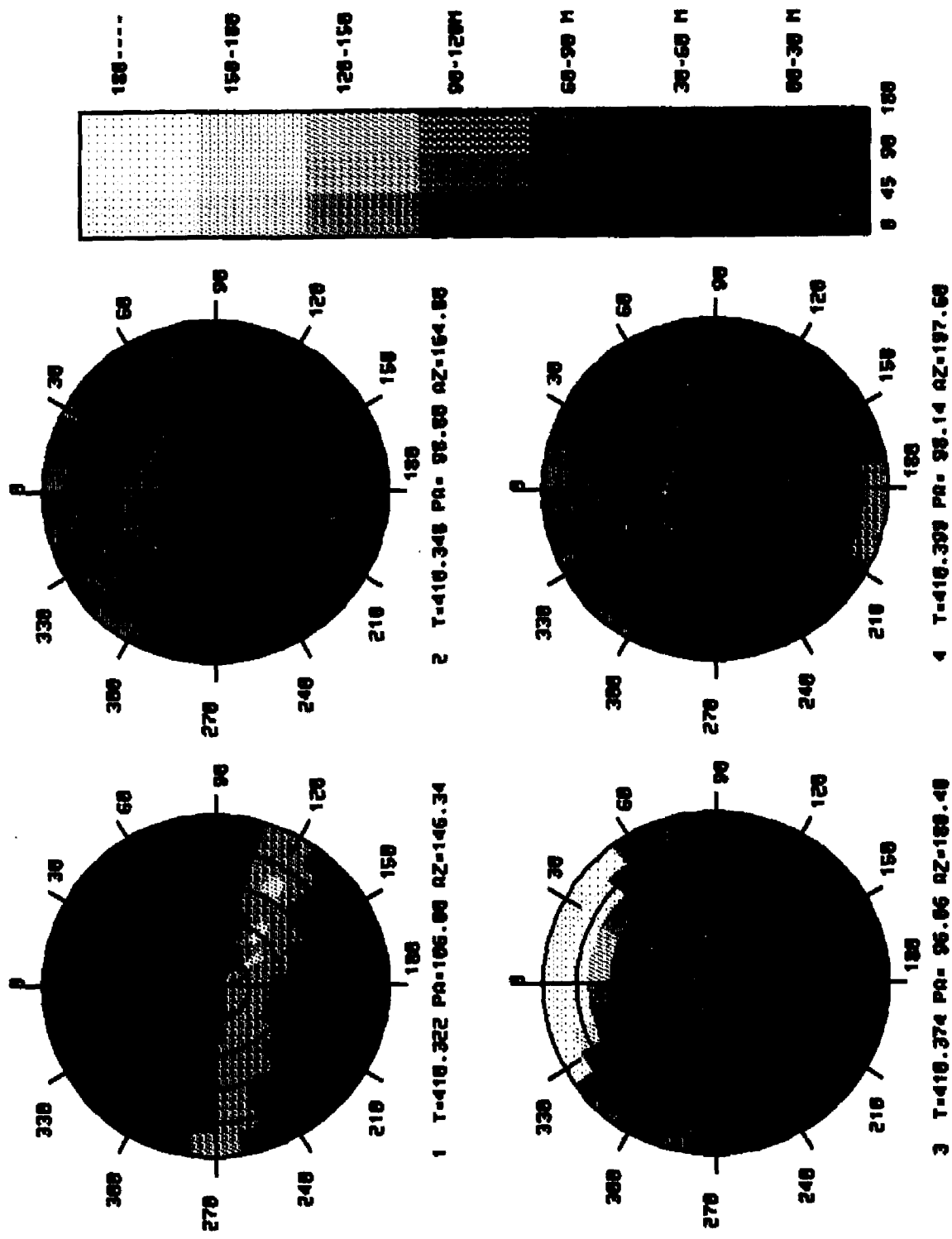


FIG. 3-7A DIRECTIONAL RESPONSE OF OCT04, 410.322-410.399s

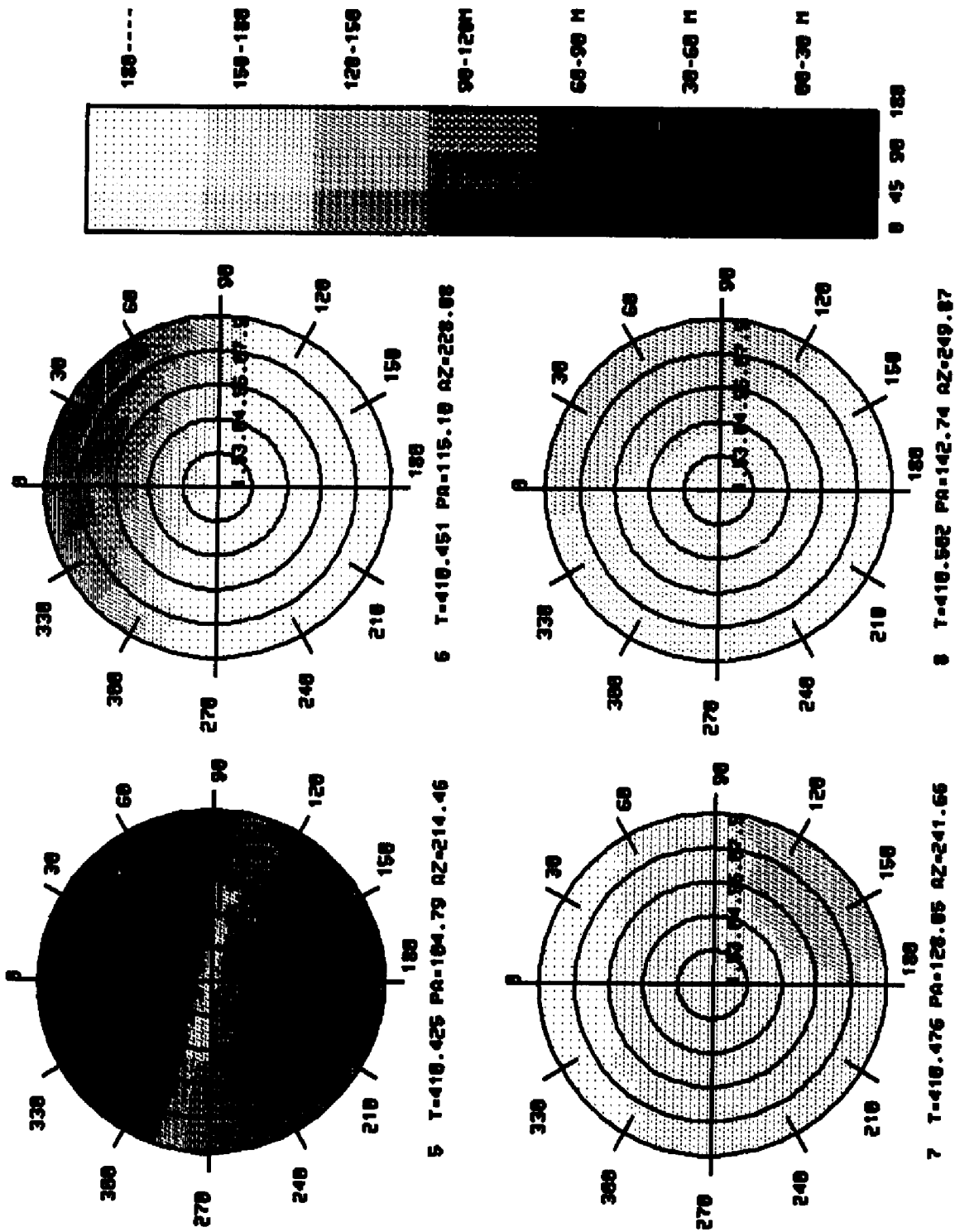


FIG. 3-7B DIRECTIONAL RESPONSE OF DCT04, 410.425-410.508s

The method we used above to trace the trajectories of the ions from the center of the detector back to the ion source can be further developed to find out the directional response of the OCTO detectors. We divide the whole OCTO detector aperture into many small portions by using the same method I developed in Appendix B.3. Then we carried out similar calculations to trace ion trajectories back from each portion. If the trajectory from an aperture portion can match well with the location and direction of the artificial ion gun, we consider that portion of the detector can receive ions that came from the argon ion gun at that moment. Otherwise we consider that portion of the OCTO detector aperture can not receive the argon ions which came from the ion gun at that moment. Fig. 3-7a and 3-7b shows the directional responses of the OCTO4 detector for the 6 \perp event. I divided the aperture of the OCTO4 detector into 201 small portions, each portion is 1.5° wide along radial direction and 9° wide along azimuthal direction. The center circle is 0.5° wide along the radial direction. The "T" represents the time of detection. The "PA" , "AZ" represent the pitch and azimuthal angles of the centerline of the OCTO4 detector at the corresponding times. The spectrum on the right side of Fig. 3-7a, 3-7b shows the encoding scheme, in which different distances from $\leq 30\text{meter}$ to $\leq 200\text{meter}$ represented by different colors from dark blue to red. The distances indicated are the minimum distances from the ion trajectories to the perpendicular argon gun. The spectrum shows also the different deviation angles from $\leq 45^\circ$ to $\leq 180^\circ$, indicated by the three different lightness levels. The solid hue (left row in spectrum) is used when the angle between ion and gun is $\leq 45^\circ$. The lightest hue (right row in the spectrum) indicated that the angle between ion and gun is $\leq 180^\circ$ and

$\geq 90^\circ$. The middle row of the spectrum indicates that the angle between ion and gun is $\geq 45^\circ$ and $\leq 90^\circ$.

Fig. 3-7a shows that the OCTO detector had some portions (near dark blue, dark hue) which can receive the artificial argon ions at the $t=410.322, 410.348, 410.374$ and 410.399 s. These results are consistent with the observations of the OCTO4 detector. Fig. 3-7b shows that the OCTO detector did not have any portions which are near dark blue and dark hue at the times of $t=410.451, 410.476$ and 410.502 s. These results indicate that the OCTO4 detector cannot receive a high artificial argon ion flux at these moments. This finding also is in agreement with the observations of the OCTO4 detector. The only exceptional case is for the time $t=410.425$. At that moment, OCTO4 received a low ion flux peak, but the calculation shown in Fig. 3-7b indicates that the OCTO4 detector should receive a high argon ion flux. In general, we should say that the calculations on directional response of the OCTO4 detector are in agreement with the observations.

3.3 Evolution of Ion Beam

It is hard to find the exact paths for all ions at an arbitrary time or the evolution of the artificial ion beam because the ions inside the beam have different initial velocities (speeds and directions). The ions will follow extremely different trajectories, so the shape of the beam will become very complicated, especially long after the ions are ejected from the guns. *Häsuler et al.* [1986] calculated the shape of the beam for different times

after injection. They assumed free gyration of the ions with a constant convection electric field of $20mV/m$. Their calculations only gave the shape of the ion beam for the very short time period (10msec to 195msec) after gun was turned on. Because their calculated shape of the beam shows only three lines, the front line and two edge lines, the shape of the beam can not be visualized in this presentation at a longer time period after ejection.

I developed a different way to calculate the shape of the ion beam. The major difference between my way and *Häusler et al.* is that I calculated all particles (or all portions) inside the beam instead of the three lines. In the Appendix B.3, I divided the ion beam into many small portions, each portion has different pitch and azimuthal angle. In the Appendix C, I generated an ion distributions for any given time. The distributions include the contribution of beam expansion and the nonuniform distribution of ions. Using my way we can calculate the shape for any time during the flight. The second difference is that *Häusler et al.* calculated the shape of the ion beam with 90° pitch angle only. My technique included all possible pitch angles. Another difference is that I used a more or less realistic model distribution for ion beam. In that model, the ions inside the beam are distributed non uniformly. According the Erlandson and Pollock's calibration, the density of the ions received by a detector at $\sim 30^\circ$ from the center line of the ion gun is about half of the density of ions received by the detector at the center line.

There is another problem we must solve before calculating the exact evolution of the ion beam. The problem is how to determine the directional angle of the ion gun, because the beam's position depends on the direction

of the ions at the moment when the ions were ejected from the gun. We previously described a series of techniques to determine the directions of all instruments on main payload, using the gyroscope data. Unfortunately, we can not use those techniques to determine the direction of the instruments on the sub payload, because there is no gyroscope on the subpayload. Of course, we can assume the spinning and separation were uniform. Then, by using the angular and linear velocity of the sub payload at the separation time, we can determine the pointing direction of any instruments on the sub payload, such as the two ion guns. In fact, the angular velocity of the sub payload was not constant after the separation. Using the above assumption therefore will allow serious errors to accumulate, so that the calculated pointing direction will not be correct at late times. It may even cause errors up to 180° .

Fortunately, a single axis magnetometer was mounted on the sub payload and recorded a sin/cos curve of magnetic field data, which is the projection of the local magnetic field on the vector along the single axis magnetometer. Figures 3-8 (134s -135s, 195s - 196s), and 3-9 (314s - 315s, 410s -411s) show the magnetic field data curves for four different time periods. From those figures we can determine the reference time and calculate the spin rate. First we note that at the peak times (for the time of 314-315s, use valley times, since the data was inverted) the submagnetometer points to the LGM north, i.e. the LGM azimuthal angle of the submagnetometer is zero. We call those times reference times. Secondly we calculated the azimuthal angle difference between submagnetometer and perpendicular gun just before separation, it was 269° , so we can think that the azimuthal angle of the centerline of the perpendicular gun was

269° at the reference times. The formula to calculate the azimuthal angles for perpendicular gun is

$$\text{Azimuthal angle} = 269^\circ - (t_{ejc} - t_{ref}) \times \text{spin rate}$$

Where the spin rate is the spinning angular speed in units of degrees per second, as shown in table 3-3. The t_{ref} is the reference time defined above and shown in table 3-3. The t_{ejc} is the time when an ion was ejected out of the perpendicular ion gun. It can be determined from the time when the ion was detected by the detector and the parallel velocity of the ion, i.e

$$t_{ejc} = t_{det} - \frac{D_{\parallel}}{v_{\parallel,ion}} \quad (3.10)$$

where t_{det} is the time when an ion was detected by the detector, D_{\parallel} is the parallel separation distance between the main payload and the sub payload, and $v_{\parallel,ion}$ is the parallel component of the ion velocity.

Table 3-3 Reference Time and Spin Rate

period, s	reference time, s	spin rate, degree/s
≤ 150	134.38	998.2±2
150 - 250	194.965	993.96±1
250 - 390	314.49	993.65±1
≥ 390	409.375	1000.±2

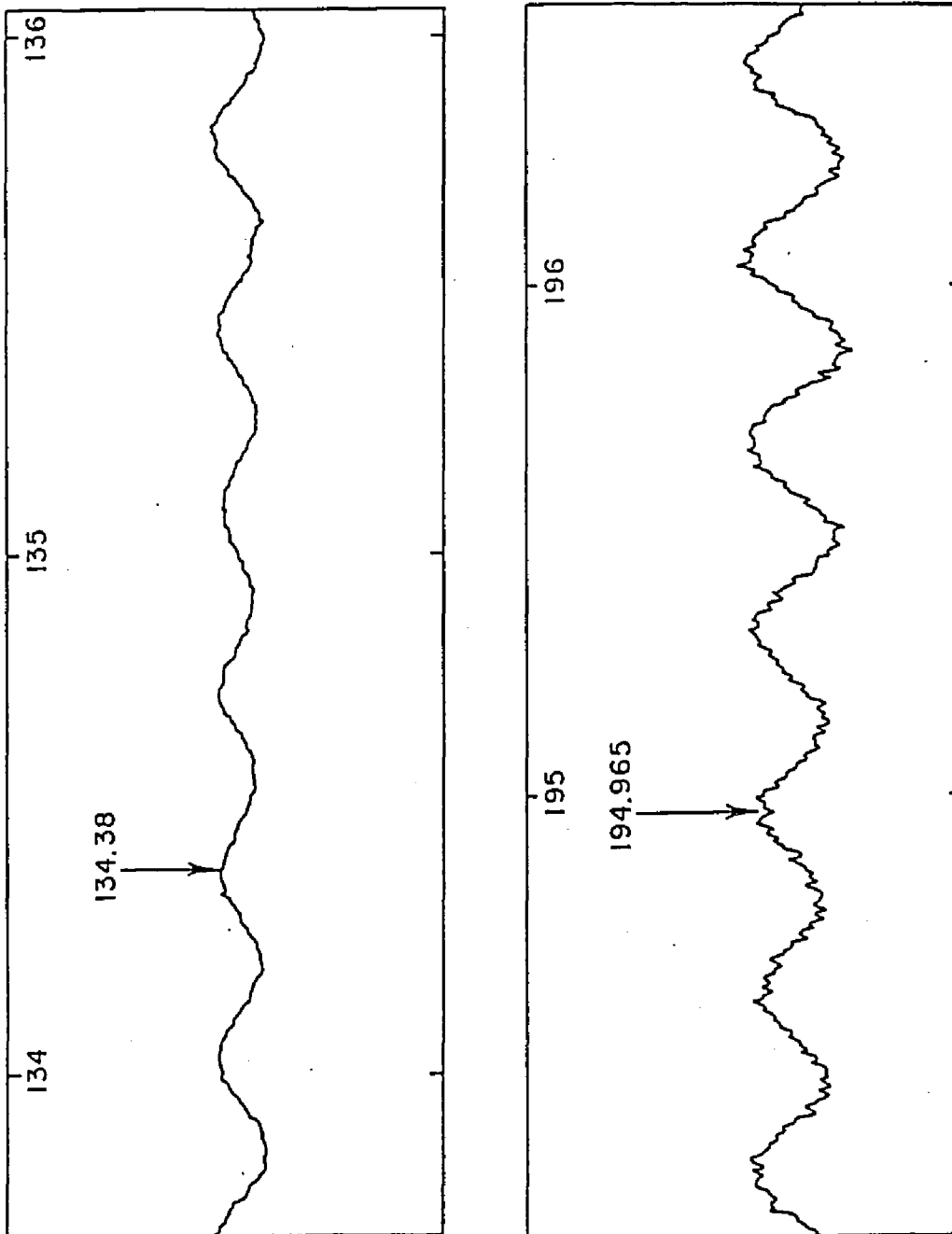


Fig. 3-8 Sub-magnetometer Data and Reference Time, (a,b)

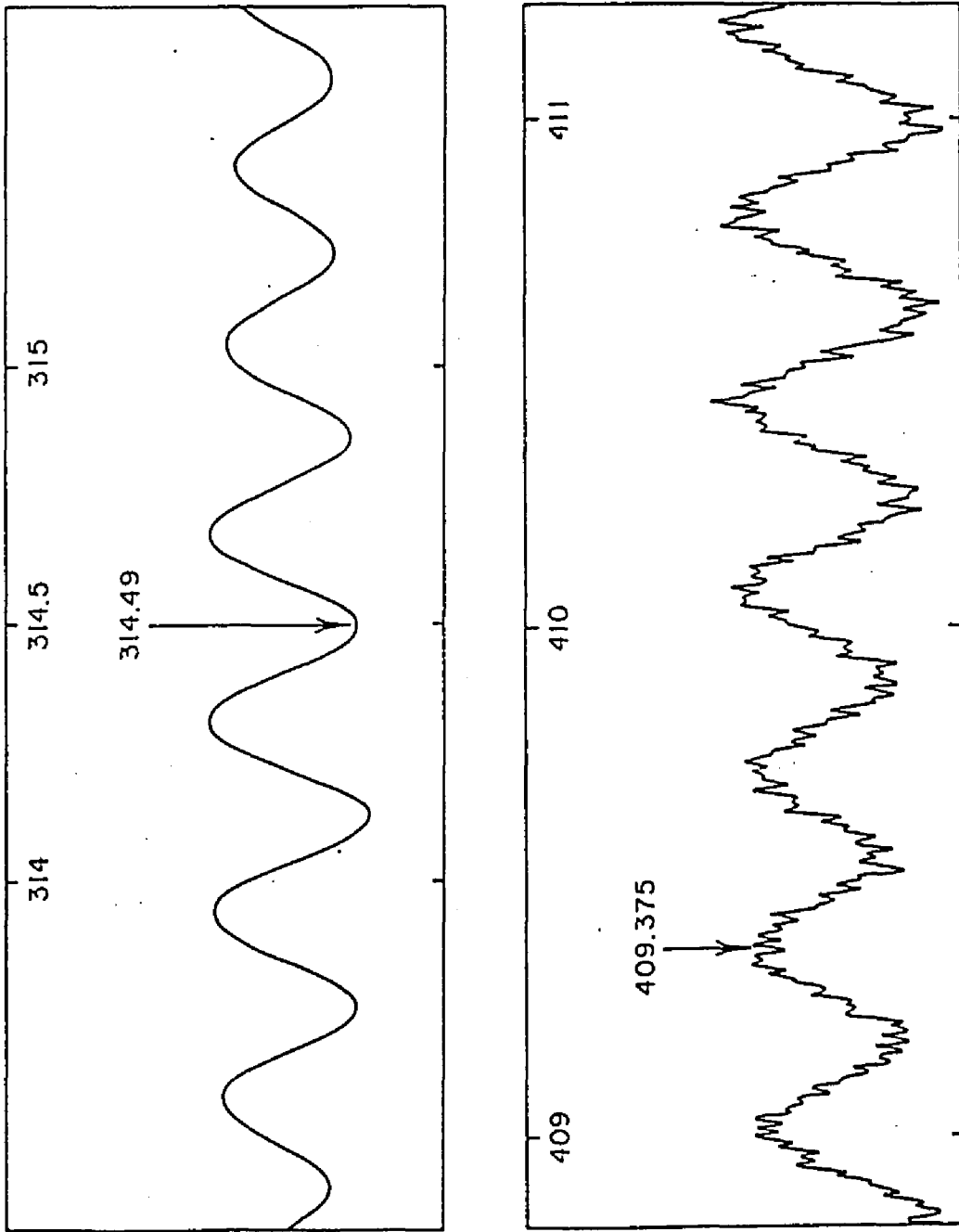


Fig. 3-9 Sub-magnetometer Data and Reference Time, (c,d)

We calculated the ion beam shapes and evolutions for several events by using my ion beam model and the reference times in Table 3-3. Fig. 3-10 shows that the evolution of the ion beam on the detector plane for the 2_{\perp} event. The detector plane is perpendicular to the local geomagnetic field and passes through the detector. Each dot represents the projection of a portion of the ion beam on the detector plane. The short line from each dot represents the projection of the direction of the ion portion on the detector plane at the detection time. The origin is the projection of the ion gun, the magnetic field points towards the paper. The small circle represents an area with a radius of 30 meter around the detector. The "DNS" and the "F" indicate the average density and flux of the ion beam inside the detector circle. We can see that the time required for the ion beam to make a full sweep is $\sim 360ms$, which equals the spin period of the sub payload. In Fig. 3-10, the dark portion of the beam is produced by ions during their first gyro period. We can see few particles outside the main portion of the beam; these ions were ejected more than one gyro period ago. Similarly, Fig. 3-11 shows the evolution of the ion beam for the 4_{\perp} (310 -312s) event. Figures 3-12, and 3-13 show the beam shapes from the 1_{\perp} event to the 8_{\perp} event. From those figures, we can see that the ion beam was expanding with time, i.e. the opening width of the beam was increasing from $\sim 70^{\circ}$ to more than 200° . We can see that the number of ions outside the main beam was increasing too. This means that more and more ions must have made more than one complete gyration before reaching the detector plane.

Fig. 3-10 Ion Beam Evolution, 21

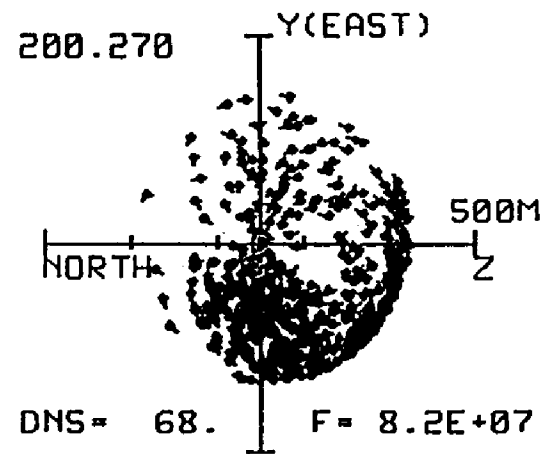
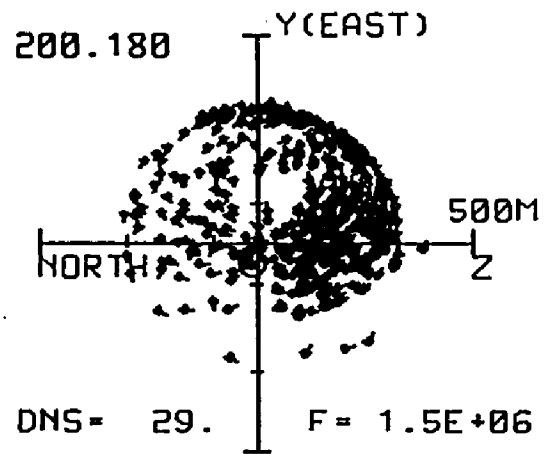
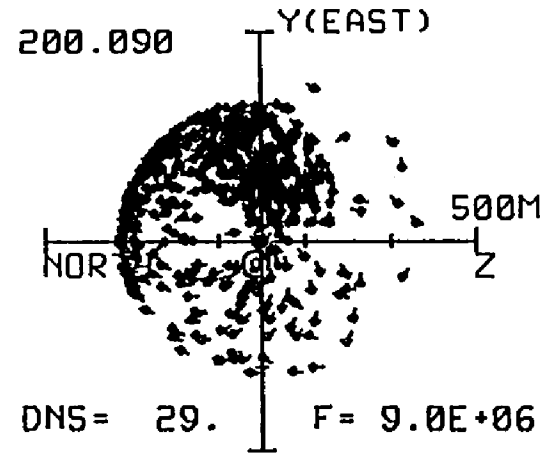
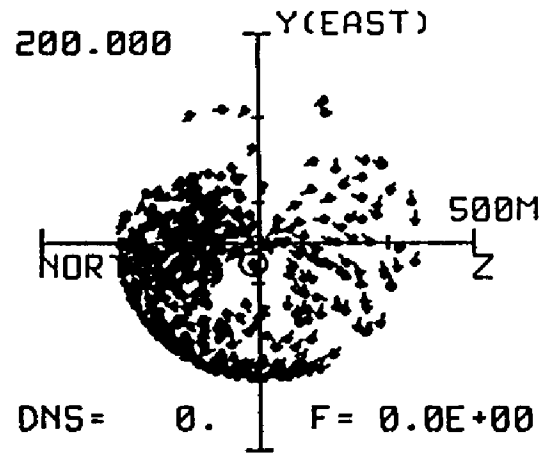


Fig. 3-11 Ion Beam Evolution, 41

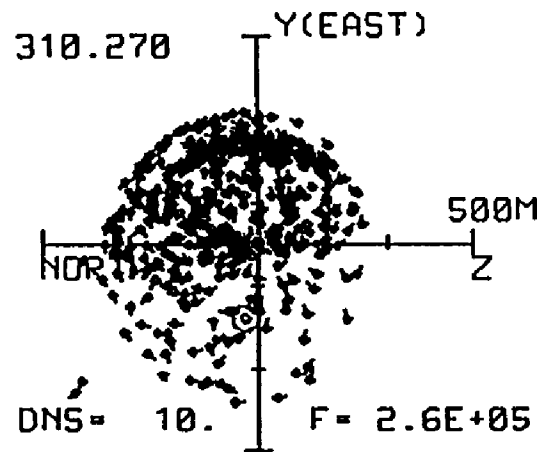
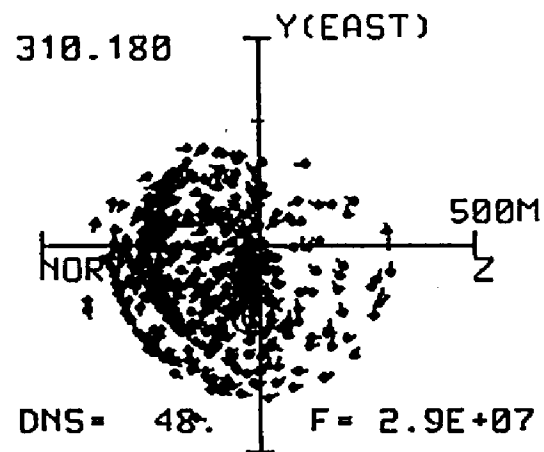
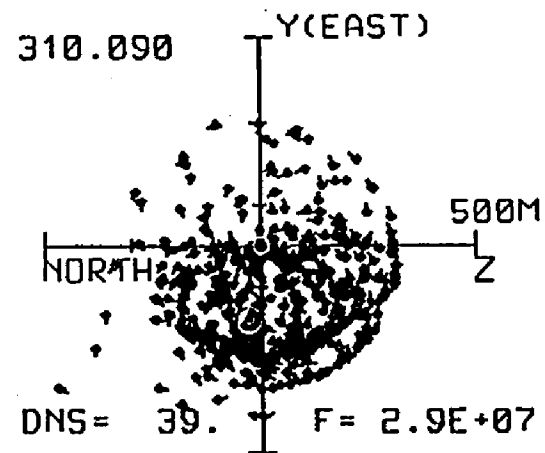
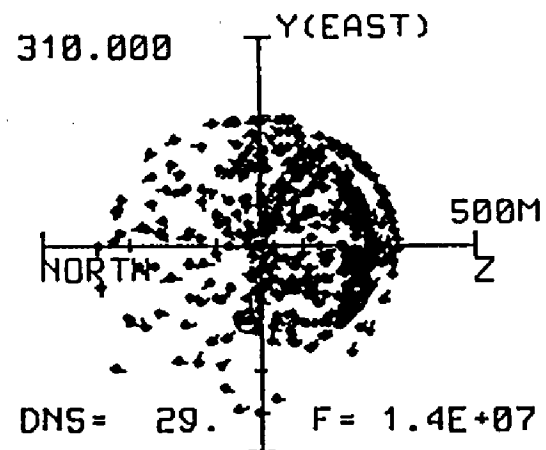


Fig. 3-12 Ion Beam Evolution, 1₁ to 4₁

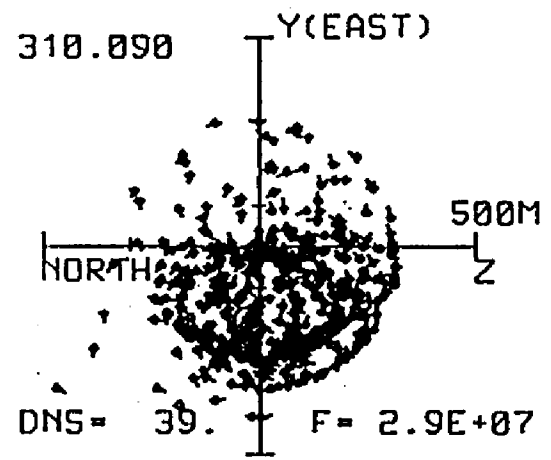
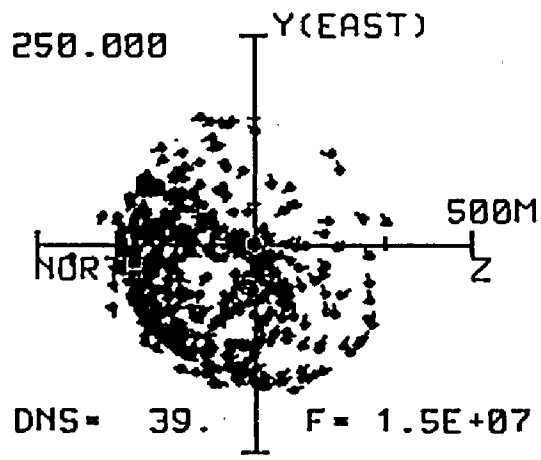
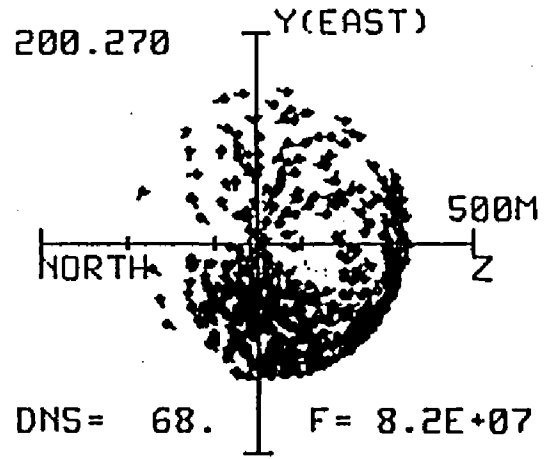
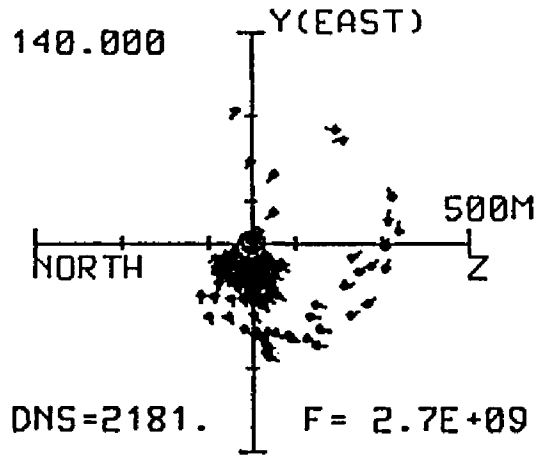
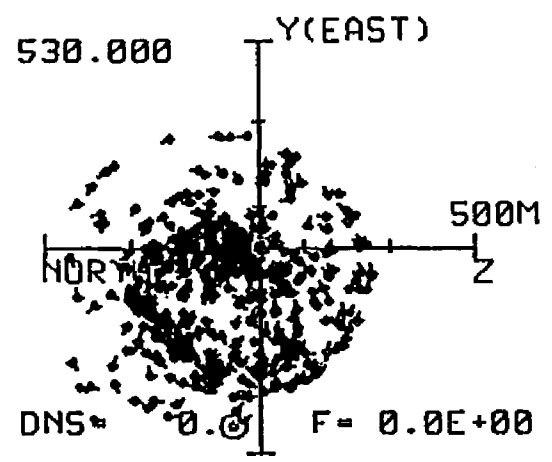
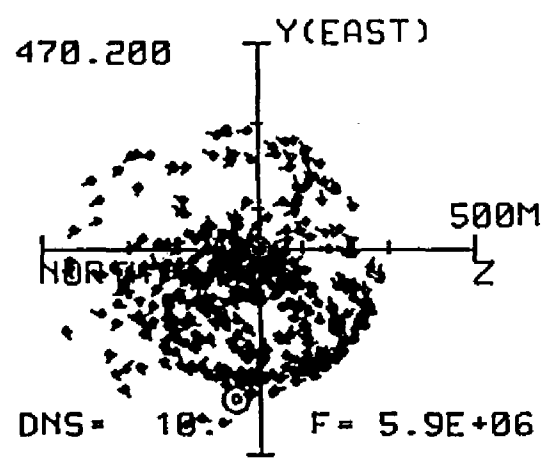
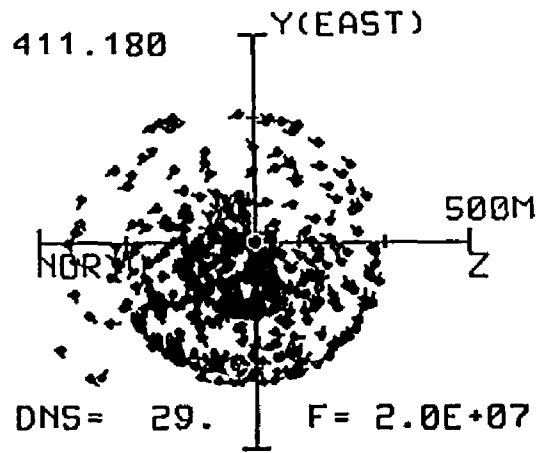
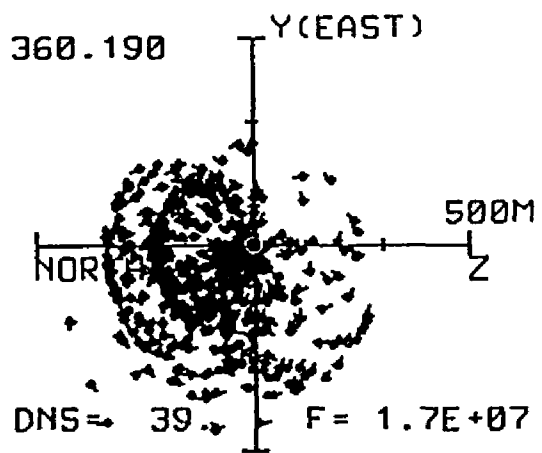


Fig. 3-13 Ion Beam Evolution, 5L to 8L



3.4 Density and flux of Argon Ions

In the last section we developed a technique to locate the beam. After a simple modification of this technique, we can calculate the density and flux of the ions near the detector. As we described before, we divided the whole ion beam into many small portions. The ions in each portion have different directional angles and speeds. The contribution from a portion of ion to the ion flux is

$$|\mathbf{J}_i| = \frac{6.0 \times 10^{17}}{N_p Area} \quad (3.11)$$

where 6.0×10^{17} is the number of the ions generated by the ion gun per second (100mA), N_p is the number of the ion portions for whole ion beam, Area is the area in the detector plane and around the detector (in my calculation, it is a circle with a 30 meter radius).

The parallel component of the $|\mathbf{J}_i|$ is

$$|\mathbf{J}_{i,\parallel}| = |\mathbf{J}_i| \cos \theta \quad (3.11b)$$

where the $\cos \theta$ is the pitch angle of the ion. the total parallel flux of ions which come form the ion gun is

$$|\mathbf{J}_{\parallel}| = \sum_i |\mathbf{J}_{i,\parallel}| \quad (3.11c)$$

Where the summation is over all ion portions which enter the area of 30 meters radius around the detector. So the contribution of this portion to the ion density is

$$\rho_i = \frac{|\mathbf{J}_i|}{v} \quad (3.12)$$

where v is the magnitude of the velocity of the ions. The total density contributed from all portions is

$$\rho = \sum_i \rho_i \quad (3.13)$$

According the formulas (3.11), (3.12), (3.13) and the technique to find the location of the ions, I calculated the average argon ion density in the sphere of 30 meters radius from the detector and the flux of ions passing the cross section of the detector with the radius of 30 meters. For the perpendicular artificial ion gun firings, the results are shown in table 3-4.

Table 3-4 Argon Beam Density and Flux

event	Time, s	density, cm^{-3}	flux/T, $cm^{-2}s^{-1}$	flux/H, $cm^{-2}s^{-1}$
1 \perp	140.00	2200	3×10^9	3×10^8
2 \perp	200.00	70	8×10^7	5×10^7
3 \perp	250.00	40	2×10^7	5×10^7
4 \perp	310.00	40	3×10^7	5×10^7
5 \perp	360.00	40	2×10^7	4×10^7
6 \perp	411.00	30	2×10^7	2×10^7
7 \perp	470.00	10	6×10^6	6×10^6
8 \perp	530.00	0	0	1×10^6

Where the times are the times in which 100ev ions were received. The density and flux/T are my calculated densities and fluxes, the flux/H are the 100ev ion fluxes received by the HEEPS detector, it was shown in Fig. 1-2. From table 3-4, we can see that the calculated densities and the fluxes didn't change too much from the 2 \perp to the 6 \perp events. The

calculated density, flux and observed flux dropped dramatically after the 7_{\perp} event. In general, the calculated densities and fluxes matched well with the observations. This provides a good evidence that the model of the ion beam which I used is reasonable.

Part II

Artificial Ion Beam and Kinetic Theory of Plasma Thermal Fluctuations

INTRODUCTION

Several interesting papers recently discussed theories, simulations and observations of thermal noise in the Earth- planetary plasma. Following the methods described by Akhiezer et al.[1975], D. D. Sentman [1982] systematically discussed plasma fluctuation theory and made comparisons with the diffuse electrostatic thermal noise commonly observed in the dayside magnetosphere. His paper concluded that for typical dayside conditions the observed waves are weakly damped Bernstein-Harris modes whose spectral density is around $10^{-8} V^2/m^2 - Hz$. The polarization of these waves perpendicular to the ambient magnetic field can be accounted for by his theory. His analysis considered a magnetized plasma composed of cold and hot electrons and ions. M. K. Hudson and I. Roth [1983, 1984] studied thermal fluctuations on the sounding rocket flights: ARCS1, 2 and 3. Their work included simulations, and was able to explain several of the observations. For ARCS1 and 2 they concentrated their discussion on two bands of electrostatic wave emissions: one around the upper hybrid frequency, one at the lower hybrid frequency. They found that the latter was enhanced by the argon beam in their simulation, in agreement

with observations on ARCS2. Their analytical analysis included an unmagnetized, single-temperature argon beam moving in the $\mathbf{B} - \mathbf{k}$ plane, perpendicular to the local magnetic field \mathbf{B} . They performed a large number of one dimensional simulations with three velocity components using periodic boundary conditions to model the actual experimental conditions at the time of the ARCS1 and 2 rocket flights. In the simulations they didn't use actual masses for electrons and ions. They used the mass ratios $m_{oxygen}/m_{electron} = 800, m_{argon}/m_{oxygen} = 2.5$, and considered a wide range of angles for \mathbf{k} and the argon beam streaming direction. The density ratios were $n_{argon} = n_{oxygen} = 0.5n_{electron}$. The temperatures T were taken to be $T_{oxygen} = T_{electron} = 0.2ev, T_{argon} = 5ev$ and the argon beam energy was taken to be 25ev. They concluded that the noise-like emissions were thermal fluctuations, that the thermal fluctuation level should be 0.01 - 0.1 mV/m without the argon beam, and that this level should be enhanced by factors of 50 and 5 for ARCS2 and 1 respectively.

The original purpose of our project was to try to use a form of plasma fluctuation theory similar to that used by Sentman, Hudson and Roth to deal with similar observations on the R29015 (ARCS3) flight. During the second perpendicular Argon Ion gun firing of R29015 (ARCS3), the DC-E detectors measured the electric field power spectra shown in Fig. 4-1. The spectra in Fig. 4-1b, 4-1c and 4-1d show spikes superimposed on a smooth background. Our goal is to determine what caused the spikes, and to see if the noise - like background represents thermal fluctuations excited by the artificial argon ion beam. R. E. Erlandson[1987], who studied the wave measurements, proposed that noise may be drift waves excited by a density gradient in the Argon ion beam.

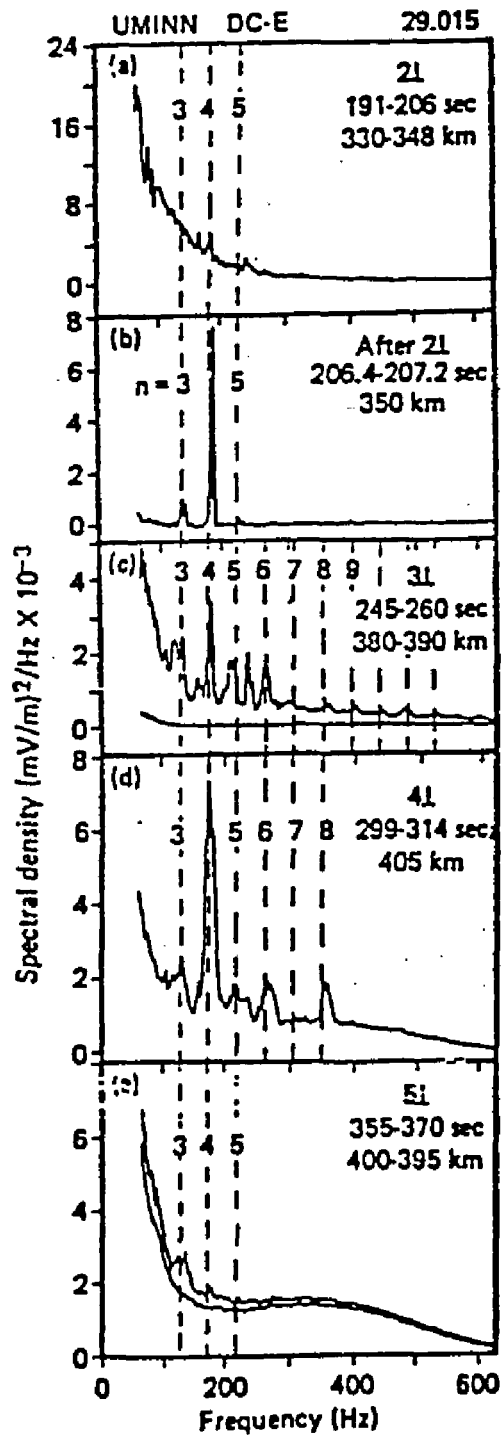


Fig. 4-1 Measured Spectral Density, 50Hz to 625Hz

First of all, to answer those questions, we checked the fluctuation theory used by Sentman and Hudson *et al.* We found the kinetic theory of fluctuations Sentman used was correct for the special cases (magnetized species, no streaming, one temperature) he studied. We had to extend this treatment to include an unmagnetized beam streaming in an arbitrary direction with respect to \mathbf{B} and \mathbf{k} in order to model the experimental conditions. The argon beam ejected by the perpendicular gun covered a pitch angle range from 20 to 160 degrees and azimuthal angles from 0 to 360 degrees with respect to the $\mathbf{B} - \mathbf{k}$ plane. Streaming which is not along the magnetic field required us to introduce the unmagnetized species, as described in chapter 6. Next I attempted to derive a correct analytic expression for an unmagnetized two temperature beam moving in any direction. The final step was applying my kinetic theory of plasma thermal fluctuations to a plasma representative of the R29015 flight (ARCS3).

Chapter 4

GENERAL THEORY OF THERMAL FLUCTUATIONS

In general, plasmas are in a quasi neutral state, and they obey Poisson's equation,

$$\nabla^2 \phi = -4\pi q(n_i - n_e) \quad (4.1)$$

where the net charge density is almost zero. If we consider each particle's motion in detail, the time averaged charge density of all species is zero, but at any given moment the microscopic charge density for all species is not exactly zero. In fact, the density of electrons and the density of ions always deviate from their mean values. This kind of deviation is called a density fluctuation.

Due to number density or charge density fluctuations in a plasma, fluctuations of some related physics quantities, such as the electric field, magnetic field, and radiated power, will simultaneously take place.

In this section we will only discuss thermal fluctuations, the fluctuations caused by thermal motion of particles in a plasma. Before going further, let us clearly define the two concepts –“thermal velocity” and “temperature”.

4.1 Thermal Velocity and Temperature

Experiments tell us that thermal phenomena involve the collective

behavior of a great number of particles moving irregularly, so people refer to irregular motion of a great number of particles as thermal motion. When a particle system is in a thermal equilibrium state, the system contains particles with a range of velocities, The most probable velocity distribution of particles is a Maxwellian distribution. The normalized Maxwellian distribution function is

$$f_m = \left(\frac{m}{2\pi KT} \right)^{3/2} \exp \left(\frac{-mv^2}{2KT} \right) \quad (4.2)$$

where v is the speed of particle, T is the temperature, and K is the Boltzmann constant. Taking an average of the kinetic energy $K.E. = (1/2)mv^2$ over all velocity space, it is easy to find that the average energy per particle per degree of freedom is $(1/2)KT$. We will use energy units to express temperature. When we say a particle's temperature is 2ev, it means its KT equals 2ev, or its 3-dimensional average energy is 3ev. For an anisotropic plasma, if we say the x - component of the temperature is 1ev, it does not mean that $(1/2)KT_x = 1ev$, but that $KT_x = 1ev$. We know that

$$1ev = 11600^\circ K \quad (4.3)$$

For convenience we can define v_{th} , or the thermal speed. Different people use different definitions for thermal speed. For example, many authors use

$$v_{th} \equiv \sqrt{\frac{KT}{m}} \quad (4.3a)$$

Francis F. Chen[1974] uses

$$v_{th} \equiv \sqrt{\frac{2KT}{m}} \quad (4.3b)$$

and H. Alfvén and Kenneth R. Lang [1980] use

$$v_{th} \equiv \sqrt{\frac{3KT}{m}} \quad (4.3c)$$

I will use Chen's definition because this choice simplifies the definition of a Maxwellian distribution function, which becomes:

$$f_m = \left(\frac{1}{\pi v_{th}^2} \right)^{3/2} \exp\left(-\frac{v^2}{v_{th}^2} \right) \quad (4.4)$$

To avoid confusion with the wave vector \mathbf{k} , we choose to use units in which Boltzmann's constant is equal to 1, and therefore the temperature T will be an energy.

4.2 Test Charges and Fluctuations

The Vlasov equation treats a plasma as a fluid in position-velocity space. The plasma state is described in terms of a continuous distribution function $f(\mathbf{v})$. Vlasov theory therefore can not answer the following questions:

1. What is the fluctuation level of electric or magnetic fields in a plasma?
2. What is the emission rate and spectrum of radiation from a thermal plasma?

These questions are connected in a basic way with the discreteness of a plasma, i.e., the fact that a plasma is a collection of individual particles. Normally we treat an ideal plasma in the limit $1/n\lambda_D^3 \rightarrow 0, q \rightarrow 0$

corresponding to a system in which the discreteness of the particles is lost and coupling of individual particles to the radiation field is lost. Where n is the number density of the plasma species, q is the charge per particle, and λ_D is the Debye length of the plasma species. To recover the effects of individual particles, we have several choices. One is to keep more than one order of $1/n\lambda_D^3$ in the BBGKY hierarchy; another is to use a very appealing physical approach, the test-particle picture, introduced by N. Rostoker and M. Rosenbluth [1960]. We will use the test particle approach later in this section. In the test-particle picture, a plasma is made up of a collection of discrete uncorrelated dressed test particles, distributed in position-velocity space according to the distribution function f_s . Each test-particle leads a double life. On the one hand, it is a test particle, moving about in a Vlasov fluid. On other hand, it is a part of the Vlasov fluid. The test-particle picture is a physical way to calculate fluctuations in density, fields and other plasma properties that depends on particle discreteness.

Now we are going to derive an expression for the plasma fluctuation spectrum by the using the test-particle picture. The test charge density can be represented by a delta function

$$\rho_{test} = q\delta(\mathbf{r} - \mathbf{r}'(t)) \quad (4.5)$$

where q is the charge on each test particle, \mathbf{r} is the observation position and $\mathbf{r}'(t)$ is the location of the test charge at time t . The test charge density is a function of time t . We are using the following basic equations:

Maxwell's equations:

$$\nabla \cdot (\mathbf{E}_0 + \mathbf{E}_1) = 4\pi(\rho_{plasma} + \rho_{test}) \quad (4.6)$$

$$\nabla \times (\mathbf{E}_0 + \mathbf{E}_1) = -\frac{1}{c} \frac{\partial \mathbf{B}_1}{\partial t} \quad (4.7)$$

$$\nabla \cdot (\mathbf{B}_0 + \mathbf{B}_1) = 0 \quad (4.8)$$

$$\nabla \times (\mathbf{B}_0 + \mathbf{B}_1) = \frac{4\pi}{c} (\mathbf{J}_{test} + \mathbf{J}_{plasma}) + \frac{1}{c} \frac{\partial \mathbf{E}_1}{\partial t} \quad (4.9)$$

Here we assume that the plasma net charge density and plasma net current density would be zero if test charges didn't exist, so that ρ_{plasma} , \mathbf{J}_{plasma} are the charge density and current density induced by test charges. Here E_0 and B_0 are time averaged values of the electric and magnetic field respectively, while E_1 and B_1 represent fluctuations of the electric and magnetic field, respectively.

Continuity Equations:

$$\frac{\partial \rho_{plasma}}{\partial t} + \nabla \cdot \mathbf{J}_{plasma} = 0 \quad (4.10)$$

$$\frac{\partial \rho_{test}}{\partial t} + \nabla \cdot \mathbf{J}_{test} = 0 \quad (4.11)$$

Ohm's law for (induced) plasma current:

$$\mathbf{J}_{plasma}(\mathbf{r}, t) = \int d\mathbf{r}' \int_{-\infty}^t dt' \vec{\sigma}(\mathbf{r}, \mathbf{r}'; t, t') \cdot \mathbf{E}(\mathbf{r}', t') \quad (4.12)$$

Taking Fourier transforms, i.e. carrying out the integration

$$\int d\mathbf{r} \int_{-\infty}^{\infty} dt e^{-i(\mathbf{k} \cdot \mathbf{r} - \omega t)}$$

on Eq. (4.6) to (4.11), note that the operators

$$\frac{\partial}{\partial t} \Rightarrow -i\omega$$

$$\nabla \Rightarrow i\mathbf{k}$$

where \Rightarrow means equivalent to. Then (4.6) to (4.11) reduce to

$$\mathbf{k} \cdot \mathbf{E}(\mathbf{k}, \omega) = -4\pi i(\rho_{plasma}(\mathbf{k}, \omega) + \rho_{test}(\mathbf{k}, \omega)) \quad (4.6f)$$

$$\mathbf{k} \times \mathbf{E}(\mathbf{k}, \omega) = \frac{\omega}{c} \mathbf{B}(\mathbf{k}, \omega) \quad (4.7f)$$

$$\mathbf{k} \cdot \mathbf{B}(\mathbf{k}, \omega) = 0 \quad (4.8f)$$

$$\mathbf{k} \times \mathbf{B}(\mathbf{k}, \omega) = -\frac{4\pi i}{c}(\mathbf{J}_{test}(\mathbf{k}, \omega) + \mathbf{J}_{plasma}(\mathbf{k}, \omega)) - \frac{\omega}{c} \mathbf{E}(\mathbf{k}, \omega) \quad (4.9f)$$

$$\rho_{plasma}(\mathbf{k}, \omega) = \frac{1}{\omega} \mathbf{k} \cdot \mathbf{J}_{plasma}(\mathbf{k}, \omega) \quad (4.10f)$$

$$\rho_{test}(\mathbf{k}, \omega) = \frac{1}{\omega} \mathbf{k} \cdot \mathbf{J}_{test}(\mathbf{k}, \omega) \quad (4.11f)$$

Note that we must be careful with Ohm's law (4.12) when we attempt to transform it. It is quite different from (4.6) to (4.11), because Ohm's law involves the concept of causality. The time integration starts from an unperturbed state at $t = -\infty$ to extends to the current time t . The plasma current J_{plasma} is gradually induced in the system due to the application of the perturbation. In (4.12) the conductivity tensor $\vec{\sigma}(\mathbf{r}, \mathbf{r}'; t, t')$ describes the response to the perturbation. Here the (\mathbf{r}', t') are the position and time the perturbation is applied, and (\mathbf{r}, t) are the position and time at which an induced plasma current is observed. The induced current is a response from all positions in the system and from times $t = -\infty$ to the current time t .

It is hard to complete the Laplace-Fourier transformation of (4.12) without a further assumption. To carry out the transformation and to get an expression in the \mathbf{k}, ω domain for Ohm's law, we now assume that the unperturbed state of the plasma system is homogeneous in space and stationary in time, i.e. the conductivity tensor is a function of $(\mathbf{r} - \mathbf{r}')$ and $(t - t')$ only.

With this assumption we can rewrite (4.12) as

$$\mathbf{J}_{plasma}(\mathbf{r}, t) = \int d\mathbf{r}' \int_{-\infty}^t dt' \vec{\sigma}(\mathbf{r} - \mathbf{r}', t - t') \cdot \mathbf{E}(\mathbf{r}', t') \quad (4.12a)$$

This is a convolution integral of the functions σ and \mathbf{E} . The Laplace-Fourier transformation of (4.12a) is

$$\mathbf{J}_{plasma}(\mathbf{k}, \omega) = \vec{\sigma}(\mathbf{k}, \omega) \cdot \mathbf{E}(\mathbf{k}, \omega) \quad (4.12f)$$

according to the convolution theorem. We should notice the difference between the transformations of the conductivity tensor $\vec{\sigma}$ and the electric field \mathbf{E} ,

$$\mathbf{E}(\mathbf{k}, \omega) = \int d\mathbf{r} \int_{-\infty}^{\infty} dt \mathbf{E}(\mathbf{r}, t) e^{-i(\mathbf{k} \cdot \mathbf{r} - \omega t)} \quad (4.13)$$

$$\vec{\sigma}(\mathbf{k}, \omega) = \int d\mathbf{r} \int_0^{\infty} dt \vec{\sigma}(\mathbf{r}, t) e^{-i(\mathbf{k} \cdot \mathbf{r} - \omega t)} \quad (4.14)$$

This is called a two sided Fourier transformation for the electric field and a one-side Fourier transformation or a Laplace transformation for the conductivity in the time domain since

$$\vec{\sigma}(\mathbf{r}, t) = 0, \quad \text{for } t \leq 0$$

Here $t \leq 0$ means the observation time is earlier than the perturbation time. This difference reflects causality of the propagation characteristics of disturbances. Note that we have changed variables by letting

$$(\mathbf{r} - \mathbf{r}') \Rightarrow \mathbf{r}$$

and

$$(t - t') \Rightarrow t$$

Now we will eliminate most induced plasma quantities, such as $\rho_{plasma}(\mathbf{k}, \omega)$, $\mathbf{J}_{plasma}(\mathbf{k}, \omega)$, and $\mathbf{B}(\mathbf{k}, \omega)$ but will keep $\mathbf{E}(\mathbf{k}, \omega)$. After some complicated but not very difficult algebraic operations, we are left with the following two equations,

$$\mathbf{k} \cdot \vec{\epsilon}(\mathbf{k}, \omega) \cdot \mathbf{E}(\mathbf{k}, \omega) = -4\pi i \rho_{test}(\mathbf{k}, \omega) \quad (4.15)$$

$$\left(\vec{\epsilon}(\mathbf{k}, \omega) - \frac{c^2 k^2}{\omega^2} \vec{I}_T \right) \cdot \mathbf{E}(\mathbf{k}, \omega) = -\frac{4\pi i}{\omega} \mathbf{J}_{test}(\mathbf{k}, \omega) \quad (4.16)$$

where

$$\vec{\epsilon}(\mathbf{k}, \omega) \equiv \vec{I} + \frac{4\pi i}{\omega} \vec{\sigma}(\mathbf{k}, \omega)$$

it is the dielectric tensor of the plasma, and

$$\vec{I}_T \equiv \vec{I} - \vec{I}_L$$

is the transverse component of the unit tensor. This is defined using the definition of the $\mathbf{k}\mathbf{k}$ or longitudinal component of the unit tensor:

$$\vec{I}_L \equiv \frac{\mathbf{k}\mathbf{k}}{k^2} = \begin{pmatrix} 0 & 0 & 0 \\ 0 & 0 & 0 \\ 0 & 0 & 1 \end{pmatrix}$$

Where the matrix elements are defined in the \mathbf{k} frame, i.e, the Z axis is along \mathbf{k} . In this frame, it is easy to see

$$\vec{I}_T = \begin{pmatrix} 1 & 0 & 0 \\ 0 & 1 & 0 \\ 0 & 0 & 0 \end{pmatrix}$$

We can also define

$$\vec{\epsilon}(\mathbf{k}, \omega) - \frac{c^2 k^2}{\omega^2} \vec{I}_T \equiv \vec{\Delta}$$

the dispersion tensor. This tensor describes the dispersion properties of a plasma through the expression (4.16), i.e.,

$$\vec{\Delta} \cdot \mathbf{E}(\mathbf{k}, \omega) = -\frac{4\pi i}{\omega} \mathbf{J}_{test}(\mathbf{k}, \omega)$$

We will only use longitudinal wave modes, that is, we are discussing the situation in which induced electric field is along the direction of wave vector, $\mathbf{E} \parallel \mathbf{k}$. In this event we can rewrite $\mathbf{E}(\mathbf{k}, \omega)$ as $E \frac{\mathbf{k}}{k}$, where E is the magnitude of the induced plasma electric field and $\frac{\mathbf{k}}{k}$ is a unit vector along the wave vector \mathbf{k} . Now (4.15) becomes

$$kE(\mathbf{k}, \omega)\varepsilon(\mathbf{k}, \omega) = -4\pi i \rho_{test}(\mathbf{k}, \omega)$$

or

$$E(\mathbf{k}, \omega) = -\frac{4\pi i \rho_{test}(\mathbf{k}, \omega)}{k \varepsilon(\mathbf{k}, \omega)} \quad (4.18)$$

where

$$\varepsilon(\mathbf{k}, \omega) = \frac{\mathbf{k} \cdot \vec{\varepsilon}(\mathbf{k}, \omega) \cdot \mathbf{k}}{k^2} \quad (4.19)$$

is the $\mathbf{k}\mathbf{k}$ component of the dielectric tensor, or the **longitudinal dielectric function**. This function will be used throughout the thesis. It is necessary to make a statement about $\rho_{test}(\mathbf{k}, \omega)$: the test charge is just a concept introduced to describe the excitation of fluctuations. It comes from all species in the plasma. From here on we don't need the concept of double life for the plasma particles. We can just throw the subscript *test* away, and denote $\rho_{test}(\mathbf{k}, \omega)$ as $\rho(\mathbf{k}, \omega)$. Taking the complex conjugate of (4.18), multiplying by (4.18), and evaluating the statistical average, we have

$$\langle E^2(\mathbf{k}, \omega) \rangle \equiv \langle \mathbf{E}(\mathbf{k}, \omega) \cdot \mathbf{E}^*(\mathbf{k}, \omega) \rangle = \frac{16\pi^2 \langle \rho^2(\mathbf{k}, \omega) \rangle}{k^2 |\varepsilon(\mathbf{k}, \omega)|^2} \quad (4.20)$$

The expressions (4.18) and (4.20) are the most fundamental expressions to evaluate fluctuations of the electric field. They relate the electric field fluctuations to the distribution of charge densities and to the dielectric characteristics of the plasma. From (4.20), we can see that the spectrum

of plasma charge density ($\rho^2(\mathbf{k}, \omega)$) and the longitudinal dielectric function $\epsilon(\mathbf{k}, \omega)$ are the two essential physical quantities one must calculate. In the next few sections I will provide the basics needed to calculate the density spectrum and the longitudinal dielectric function of a plasma.

4.3 Klimontovich Distribution Function

Consider a group of identical particles contained in the volume V . Each particle is characterized by an electric charge q and a mass m . We assume a smeared out background of opposite charges so that the zero order electric field of the system is zero. The average particle number density of the system is n .

Introduce the 6 dimensional phase space coordinates:

$$\mathbf{X}_i(t) \equiv (\mathbf{r}_i(t), \mathbf{v}_i(t))$$

Where i denotes for the i th particle. Now consider a unit volume containing exactly n particles, where n is the average number density of the whole system. In phase space, the microscopic density can be expressed as a summation of six - dimensional δ functions

$$N(\mathbf{X}; t) \equiv \frac{1}{n} \sum_{i=1}^n \delta[\mathbf{X} - \mathbf{X}_i(t)] \quad (4.21)$$

where $\mathbf{X} \equiv (\mathbf{r}, \mathbf{v})$, is the observation phase point. The function $N(\mathbf{X}; t)$ may be called the **Klimontovich Distribution Function**. It is normalized

according to

$$\begin{aligned}
 \int N(\mathbf{X}, t) d\mathbf{X} &= \frac{1}{n} \int \sum_{i=1}^n \delta(\mathbf{X}(t) - \mathbf{X}_i(t)) d\mathbf{X} \\
 &= \frac{1}{n} n \\
 &= 1
 \end{aligned} \tag{4.22}$$

This function describes the macroscopic probability of finding one particle in a unit phase space volume at phase point \mathbf{X} .

4.4 Single and Two Particle Distribution Functions

A macroscopic system with specified macroscopic physical properties can be in any of an infinite number of different microscopic states. Take an ensemble average of the Klimontovich distribution function,

$$\langle N(\mathbf{X}, t) \rangle = \left\langle \frac{1}{n} \sum_{i=1}^n \delta(\mathbf{X} - \mathbf{X}_i(t)) \right\rangle$$

Where the brackets $\langle \rangle$ denote the ensemble average. Define

$$\langle N(\mathbf{X}, t) \rangle \equiv f_1(\mathbf{X}, t) \tag{4.23}$$

This function gives the probability of finding a particle at the position \mathbf{X} and at the time t , averaged over all the possible microscopic states. We call $\langle N(\mathbf{X}, t) \rangle$ or $f_1(\mathbf{X}, t)$ the single particle distribution function. The single particle distribution function adequately describes a plasma in which all particles are independent or uncorrelated. If the particles are not completely independent, for example, if there are correlations between

particle pairs, then we must also introduce the two-particle distribution function. Consider the product

$$\sum_{i=1}^n \delta(\mathbf{X} - \mathbf{X}_i(t)) \sum_{j=1}^n \delta(\mathbf{X}' - \mathbf{X}_j(t)) \quad (4.24)$$

This product describes the joint distribution in which i th particle appears at \mathbf{X} and the j th particle appears at \mathbf{X}' simultaneously, i.e. the particle pair is separated by $\mathbf{X}_i(t) - \mathbf{X}_j(t)$. We can expand the expression above as follows

$$\begin{aligned} N(\mathbf{X}; t)N(\mathbf{X}'; t) &= \frac{1}{n^2} \sum_{i=1}^n \delta(\mathbf{X} - \mathbf{X}_i(t)) \sum_{j=1}^n \delta(\mathbf{X}' - \mathbf{X}_j(t)) \\ &= \frac{1}{n^2} \sum_{i=1}^n \delta(\mathbf{X} - \mathbf{X}') \delta(\mathbf{X} - \mathbf{X}_i(t)) \\ &\quad + \frac{1}{n^2} \sum_{i \neq j}^n \delta(\mathbf{X} - \mathbf{X}_i(t)) \delta(\mathbf{X}' - \mathbf{X}_j(t)) \end{aligned} \quad (4.25)$$

Take the ensemble average of (4.25). The average of the first summation on the right hand side reduces to the single particle distribution function, i.e. (4.23). The second summation defines the two-particle distribution function $f_2(\mathbf{X}, \mathbf{X}'; t)$, so

$$\langle N(\mathbf{X}, t)N(\mathbf{X}'; t) \rangle = \frac{1}{n} \delta(\mathbf{X} - \mathbf{X}') f_1(\mathbf{X}, t) + f_2(\mathbf{X}, \mathbf{X}', t) \quad (4.26)$$

The ensemble average of the second summation in (4.25) gave us a definition of the two-particle distribution function

$$\frac{1}{n^2} \langle \sum_{i \neq j}^n \delta(\mathbf{X} - \mathbf{X}_i(t)) \delta(\mathbf{X}' - \mathbf{X}_j(t)) \rangle \equiv f_2(\mathbf{X}, \mathbf{X}', t) \quad (4.27)$$

From (4.25),(4.26) and (4.27) it is clear that to describe a system in which particle pairs are correlated requires a combination of a single particle distribution function and a two-particle distribution function.

4.5 Static and Dynamic Form Factors

There are number of different ways to treat plasma fluctuation phenomena. In my opinion, using form factors and particle correlations, like Setsuo Ichimaru[1973] did, is one of the clearest ways. It therefore is necessary to give a brief review of the **static form factor, the dynamic form factor, and correlation functions**. As we did in the section on the Klimontovich distribution function, we consider a classical system with an average number density n , i.e. there are n identical particles in each unit volume. The microscopic charge density of the system of point charges may be expressed as

$$\rho(\mathbf{r}, t) = e \sum_{i=1}^n \delta[\mathbf{r} - \mathbf{r}_i(t)] \quad (4.28)$$

where the $\mathbf{r}_i(t)$ represents the spatial trajectory of the i th particle. The deviation of the charge density from the mean value n is

$$\begin{aligned} \delta\rho(\mathbf{r}, t) &= \rho(\mathbf{r}, t) - en \\ &= e \sum_{i=1}^n \delta[\mathbf{r} - \mathbf{r}_i(t)] - en \end{aligned} \quad (4.29)$$

Taking the spatial Fourier transformation of (4.29) yields

$$\delta\rho(\mathbf{k}, t) = \int d^3r \delta\rho(\mathbf{r}, t) e^{-i\mathbf{k}\cdot\mathbf{r}}$$

$$= e \sum_{i=1}^n e^{-i\mathbf{k} \cdot \mathbf{r}_i(t)} - en\delta_{\mathbf{k},0} \quad (4.30.)$$

where

$$\delta_{\mathbf{k},0} \equiv \begin{cases} 1, & \text{if } \mathbf{k} = 0 \\ 0, & \text{otherwise} \end{cases}$$

This is the three - dimensional extension of Kronecker's delta function. Spectral functions are defined through statistical averages. As a first example, consider the spectral distribution function of the density fluctuation

$$S(\mathbf{k}) = \frac{1}{n} \langle \delta\rho(\mathbf{k}, t)\delta\rho(-\mathbf{k}, t) \rangle \quad (4.31)$$

the mean square value of the function defined in Eq.(4.30). As in the single particle distribution definition, the angular brackets denote a statistical average. The new function is named the **static form factor**. The static form factor represents a power spectrum of density fluctuations in \mathbf{k} space. As a example of evaluating the ensemble statistical average, let's try to calculate the static form factor $S(\mathbf{k})$. Substituting the Eq. (4.30) into the Eq. (4.31), we have

$$\begin{aligned} S(\mathbf{k}) &= \frac{e^2}{n} \langle \left(\sum_{i=1}^n e^{-i\mathbf{k} \cdot \mathbf{r}_i(t)} - n\delta_{\mathbf{k},0} \right) \left(\sum_{j=1}^n e^{+i\mathbf{k} \cdot \mathbf{r}_j(t)} - n\delta_{\mathbf{k},0} \right) \rangle \\ &= \frac{e^2}{n} \langle \sum_{i=j}^n 1 - n\delta_{\mathbf{k},0} \left(\sum_{i=1}^n e^{-i\mathbf{k} \cdot \mathbf{r}_i(t)} + \sum_{j=1}^n e^{+i\mathbf{k} \cdot \mathbf{r}_j(t)} \right) \right. \\ &\quad \left. + n^2\delta_{\mathbf{k},0}^2 \right\rangle + \frac{e^2}{n} \langle \sum_{i \neq j}^n e^{-i\mathbf{k} \cdot (\mathbf{r}_i - \mathbf{r}_j)} \rangle \end{aligned} \quad (4.32)$$

Inside of the brackets, the first term equals n , the second term will average to $-2n^2\delta_{\mathbf{k},0}^2$. In the second and third term we may use $\delta^2 = \delta$, The fourth

term describes the pair correlations. When the positions of two different particles are uncorrelated, the fourth term yields $n(n-1)\delta_{\mathbf{k},0}$ and finally

$$\begin{aligned} S(\mathbf{k}) &= e(1 - n\delta_{\mathbf{k},0} + (n-1)\delta_{\mathbf{k},0}) \\ &= e(1 - \delta_{\mathbf{k},0}) \end{aligned} \quad (4.32a)$$

The static form factor represents the power spectrum of the charge density fluctuations in \mathbf{k} space, as you see above, but does not exhaust all the information contained in the random variable $\delta\rho(\mathbf{k}, t)$. Significantly, it does not describe the time-dependent behavior or the dynamical structure of the random variable. Such information is described by the **dynamic form factor** defined by

$$S(\mathbf{k}, \omega) = \frac{1}{2\pi} \int_{-\infty}^{\infty} dt \langle \delta\rho(\mathbf{k}, t + t') \delta\rho(-\mathbf{k}, t') \rangle e^{i\omega t} \quad (4.33)$$

This is a time-domain Fourier transform of the power spectrum of charge density fluctuations in \mathbf{k} space. It represents the time correlation of the charges. Note that t' does not explicitly appear in $S(\mathbf{k}, \omega)$ because we have assumed time independence.

We need to evaluate the power spectrum of density fluctuations $\delta\langle\rho^2(\mathbf{k}, \omega)\rangle$ or neglecting the uniform background, we may evaluate the power spectrum of the charge density $\langle\rho^2(\mathbf{k}, \omega)\rangle$ and the longitudinal dielectric function $\varepsilon(\mathbf{k}, \omega)$. As a simple analogue of the definition of the dynamic form factor, we could define the power spectrum of the plasma charge density as

$$\langle\rho^2(\mathbf{k}, \omega)\rangle = \langle \rho(\mathbf{k}, \omega) \rho^*(\mathbf{k}, \omega) \rangle \equiv \frac{1}{2\pi} \int_{-\infty}^{\infty} dt \langle \rho(\mathbf{k}, t + t') \rho(-\mathbf{k}, t') \rangle e^{i\omega t} \quad (4.34)$$

where the integration variable is the time difference between the two phase space points, and t' is the current time. The variable t' again does not appear on the left side of (4.34) because we have assumed this function is time independent. We have already seen that

$$\rho(\mathbf{k}, t) = e \sum_{i=1}^n e^{-i\mathbf{k}\cdot\mathbf{r}_i(t)} \quad (4.35)$$

This is similar to Eq. (4.30). Substituting (4.35) into (4.34) we have

$$\begin{aligned} \langle \rho(\mathbf{k}, t + t')\rho(-\mathbf{k}, t') \rangle &= e^2 \left\langle \sum_{i=1}^n e^{-i\mathbf{k}\cdot\mathbf{r}_i(t+t')} \sum_{j=1}^n e^{+i\mathbf{k}\cdot\mathbf{r}_j(t')} \right\rangle \\ &= e^2 \left\langle \sum_{i=j=1}^n e^{-i\mathbf{k}\cdot(\mathbf{r}_i(t+t')-\mathbf{r}_j(t'))} \right\rangle \\ &+ e^2 \left\langle \sum_{i \neq j}^n e^{-i\mathbf{k}\cdot(\mathbf{r}_i(t+t')-\mathbf{r}_j(t'))} \right\rangle \end{aligned} \quad (4.36)$$

The second term involves the two - particle distribution function, and we neglect it here. For our uniform time stationary distribution, we can chose a coordinate system in which $t'=0$ and the current position is the origin, $\mathbf{r}(t')=0$. Then (4.36) yields

$$\langle \rho(\mathbf{k}, t + t')\rho(-\mathbf{k}, t') \rangle = ne^2 e^{-i\mathbf{k}\cdot\mathbf{r}(t)} \quad (4.37)$$

Where $\mathbf{r}(t)$ is the trajectory of a particle that arrives at the origin at $t'=0$. If we use the normalized single-particle distribution function $f_1(\mathbf{X}, t)$ to express number density n , i.e.

$$n = n \int d^3v f_1(\mathbf{X}, t)$$

and now take the ensemble average,

$$\langle \rho(\mathbf{k}, t + t')\rho(-\mathbf{k}, t') \rangle = ne^2 \int d^3v f_1(\mathbf{X}, t) e^{-i\mathbf{k}\cdot\mathbf{r}(t)} \quad (4.38)$$

Substituting Eq. (4.38) into the definition of the power spectrum of plasma density (4.34) and using the uniform plasma assumption we have

$$\langle \rho^2(\mathbf{k}, \omega) \rangle = ne^2 \int d^3v f_s(\mathbf{v}) \int_{-\infty}^{\infty} e^{-i(\mathbf{k} \cdot \mathbf{r}(t) - \omega t)} dt \quad (4.39)$$

This is the general expression of the power spectrum of plasma charge density fluctuations, where $f_s(\mathbf{v})$ is the normalized distribution function of the s species, and $\mathbf{r}(t)$ is the unperturbed particle trajectory. In the following sections we will discuss it in detail for magnetized and unmagnetized plasma species.

Chapter 5

FLUCTUATIONS IN A MAGNETIZED PLASMA

5.1 Charge Density of Power Spectrum

For a magnetized species, the trajectories of particles will involve gyro motion around magnetic field lines plus straight motion along the \mathbf{B} field lines. Therefore, the exponent in Eq. (4.39) becomes

$$\begin{aligned}
 \omega t - \mathbf{k} \cdot \mathbf{r}(t) &= \omega t - k_x x(t) - k_z z(t) \\
 &= \omega t - k_{\perp} x(t) - k_{\parallel} v_{\parallel} t \\
 &= \omega t - k_{\perp} \int_0^t v_{\perp} \cos \phi(t') dt' - k_{\parallel} v_{\parallel} t \\
 &= \omega t - \frac{k_{\perp} v_{\perp}}{\omega_s} [\sin(\omega_s t + \phi_0) - \sin \phi_0] - k_{\parallel} v_{\parallel} t \quad (5.1)
 \end{aligned}$$

where ω_s is the gyro frequency of the particle for species s , and ϕ_0 is the initial phase angle of the particle. The charge density spectrum $\langle \rho^2(\mathbf{k}, \omega) \rangle$ equals

$$n_s e^2 \int d^3v f_s(\mathbf{v}) \int_{-\infty}^{\infty} dt e^{i(\omega t - k_{\parallel} v_{\parallel} t)} \exp\left[i \frac{k_{\perp} v_{\perp}}{\omega_s} (\sin \phi_0 - \sin(\omega_s t + \phi_0))\right] \quad (5.2)$$

for a magnetized species. The expansion formula

$$e^{iz \sin y} = \sum_{n=-\infty}^{\infty} J_n(x) e^{iny}$$

give

$$\begin{aligned}
& \exp\left[i\frac{k_{\perp}v_{\perp}}{\omega_s}(\sin\phi_0 - \sin(\omega_s t + \phi_0))\right] \\
&= \sum_{n=-\infty}^{\infty} J_n\left(\frac{k_{\perp}v_{\perp}}{\omega_s}\right) e^{in\phi_0} \sum_{m=-\infty}^{\infty} J_m\left(\frac{k_{\perp}v_{\perp}}{\omega_s}\right) e^{-im(\phi_0 + \omega_s t)} \\
&= \sum_{n=-\infty}^{\infty} J_n\left(\frac{k_{\perp}v_{\perp}}{\omega_s}\right) \sum_{m=-\infty}^{\infty} J_m\left(\frac{k_{\perp}v_{\perp}}{\omega_s}\right) e^{i(n-m)\phi_0} e^{-im\omega_s t} \quad (5.3)
\end{aligned}$$

Integrating over initial phase angle ϕ_0 and using the selection rule

$$\int_0^{2\pi} d\phi_0 e^{i(n-m)\phi_0} = 2\pi\delta_{nm} \quad (5.4)$$

where

$$\delta_{nm} = \begin{cases} 1, & \text{if } n=m \\ 0, & \text{otherwise} \end{cases}$$

Eq. (4.39) becomes

$$\langle \rho^2(\mathbf{k}, \omega) \rangle = n_s e^2 \int d^3v f_s(\mathbf{v}) \sum_{n=-\infty}^{\infty} J_n^2\left(\frac{k_{\perp}v_{\perp}}{\omega_s}\right) \int_{-\infty}^{\infty} e^{i(\omega t - k_{\parallel}v_{\parallel} t - n\omega_s t)} dt \quad (5.5)$$

or

$$\langle \rho^2(\mathbf{k}, \omega) \rangle = 2\pi n_s e^2 \sum_{n=-\infty}^{\infty} \int d^3v f_s(\mathbf{v}) J_n^2\left(\frac{k_{\perp}v_{\perp}}{\omega_s}\right) \delta(\omega - k_{\parallel}v_{\parallel} - n\omega_s) \quad (5.6)$$

In the last step we used the definition of the *Dirac Delta* function

$$\int_{-\infty}^{\infty} e^{izt} dt = 2\pi\delta(z)$$

Eq. (5.6) is a most basic formulation for evaluating the fluctuations excited by a magnetized species. It's easy to see that (5.6) will reduce to

$$\langle \rho^2(\mathbf{k}, \omega) \rangle = 2\pi n_s e^2 \int d^3v f_s(\mathbf{v}) \delta(\omega - k_{\parallel} v_{\parallel}) \quad (5.7)$$

when $k_{\perp} = 0$. Sentman [1982] used this expression for $k_{\perp} = 0$ and for the unmagnetized case $\mathbf{B} = 0$. For an unmagnetized plasma (ion beam) in a magnetized plasma, it is easy to derive that the charge density fluctuations should be

$$\langle \rho^2(\mathbf{k}, \omega) \rangle = 2\pi n_s e^2 \int d^3v f_s(\mathbf{v}) \delta(\omega - \mathbf{k} \cdot \mathbf{v}) \quad (5.8)$$

This expression is easy to prove by using the fact that the trajectory of an unmagnetized particle is a straight line, i.e.

$$\begin{aligned} \omega t - \mathbf{k} \cdot \mathbf{r}(t) &= \omega t - \mathbf{k} \cdot \mathbf{v}t \\ &= (\omega - \mathbf{k} \cdot \mathbf{v})t \end{aligned} \quad (5.9)$$

Inserting (5.9) into (4.39), gives (5.8). For a magnetized plasma species with a Maxwellian distribution function

$$f_s(v_{\parallel}, v_{\perp}) = \frac{1}{\pi^{3/2} a_{s\perp}^2 a_{s\parallel}} \exp \left[- \left(\frac{v_{\perp}^2}{a_{s\perp}^2} + \frac{v_{\parallel}^2}{a_{s\parallel}^2} \right) \right] \quad (5.10)$$

where $a_{s\parallel}, a_{s\perp}$ represent two components of thermal velocity of the s -species. Inserting (5.10) into (5.6) and carrying out the integration, we found the charge density power spectrum is

$$\langle \rho^2(\mathbf{k}, \omega) \rangle = \sum_s \frac{2\sqrt{\pi} e^2 n_s}{a_{s\parallel} |k_{\parallel}|} \sum_{n=-\infty}^{\infty} \Lambda_n \left(\frac{k_{\perp}^2 a_{s\perp}^2}{2\omega_s^2} \right) e^{-\left(\frac{\omega - n\omega_s}{k_{\parallel} a_{s\parallel}} \right)^2} \quad (5.11)$$

where we used the relations

$$\delta(\omega - k_{\parallel} v_{\parallel} - n\omega_s) = \frac{1}{|k_{\parallel}|} \delta\left(v_{\parallel} - \frac{\omega - n\omega_s}{k_{\parallel}}\right)$$

and

$$\int_0^\infty v_\perp J_n^2\left(\frac{k_\perp v_\perp}{\omega_s}\right) \exp\left(-\left(\frac{v_\parallel}{a_{s\perp}}\right)^2\right) dv_\perp = \frac{a_{s\perp}^2}{2} \Lambda_n\left(\frac{k_\perp^2 a_{s\perp}^2}{2\omega_s^2}\right) \quad (5.12)$$

The lambda function is defined as

$$\Lambda(x) \equiv e^{-x} I_n(x)$$

Using almost the same procedure as we did here, we can find the power spectrum of the charge density of the *s*th plasma species including streaming along the magnetic field **B** direction. This is a common case used in analytic calculations by many authors:

$$\langle \rho^2(\mathbf{k}, \omega) \rangle = \sum_s \frac{2\sqrt{\pi} e^2 n_s}{a_{s\parallel} |k_\parallel|} \sum_{n=-\infty}^{\infty} \Lambda_n\left(\frac{k_\perp^2 a_{s\perp}^2}{2\omega_s^2}\right) e^{-\left(\frac{\omega - k_\parallel u_\parallel - n\omega_s}{k_\parallel a_{s\parallel}}\right)^2} \quad (5.13)$$

where the u_\parallel is the parallel component of the streaming velocity.

5.2 Dielectric Function for Magnetized Species

To evaluate the power spectrum of electric field fluctuations, we must know the longitudinal dielectric function of the magnetized species, $\epsilon(\mathbf{k}, \omega)$, in addition to the power spectrum of the charge density. In Ichimaru [1973], as well as many classical plasma textbooks, an expression is given for the dielectric tensor. The general integral expression is

$$\vec{\epsilon}(\mathbf{k}, \omega) = \left(1 - \frac{\omega_p^2}{\omega^2}\right) \vec{I} - \sum_s \frac{\omega_{p,s}^2}{\omega^2} \sum_{n=-\infty}^{\infty} \int d^3v \left(\frac{n\omega_s}{v_\perp} \frac{\partial f_s}{\partial v_\perp} + k_\parallel \frac{\partial f_s}{\partial v_\parallel} \right)$$

$$\times \frac{\Pi_s(v_\perp, v_\parallel; n)}{n\omega_s + k_\parallel v_\parallel - \omega - i\eta} \quad (5.14)$$

where

$$\omega_p^2 \equiv \sum_s \omega_{p,s}^2$$

is the plasma frequency, ω_s is the cyclotron frequency of the species S particle, ω is a complex frequency, η is a positive infinite small parameter, and f_s is the distribution function of the s species. The tensor $\Pi_s(v_\perp, v_\parallel; n)$ is defined by

$$\Pi_s(v_\perp, v_\parallel; n) = \begin{pmatrix} \frac{n^2 \omega_s^2}{k_\perp^2} J_n^2 & i v_\perp \frac{n \omega_s}{k_\perp} J_n J_n' & v_\parallel \frac{n \omega_s}{k_\perp} J_n^2 \\ -i v_\perp \frac{n \omega_s}{k_\perp} J_n J_n' & v_\perp^2 (J_n')^2 & -i v_\parallel v_\perp J_n J_n' \\ v_\parallel \frac{n \omega_s}{k_\perp} J_n^2 & i v_\parallel v_\perp J_n J_n' & v_\parallel^2 J_n^2 \end{pmatrix} \quad (5.14a)$$

where

$$\int d^3v \equiv 2\pi \int_0^\infty v_\perp dv_\perp \int_{-\infty}^\infty dv_\parallel$$

$$J_n \equiv J_n \left(\frac{k_\perp v_\perp}{\omega_s} \right)$$

is the Bessel Function, and

$$J_n' \equiv \frac{dJ_n \left(\frac{k_\perp v_\perp}{\omega_s} \right)}{d \left(\frac{k_\perp v_\perp}{\omega_s} \right)}$$

For our case, we only discuss the excitation and propagation of the longitudinal wave, so we need the expression of the longitudinal dielectric function; it is easy to get from (5.14) with the aid of (4.19). This is

$$\epsilon(\mathbf{k}, \omega) = 1 - \sum_s \left(\frac{\omega_{p,s}}{k} \right)^2 \sum_{n=-\infty}^{\infty} \int d^3v \left(\frac{n \omega_s}{v_\perp} \frac{\partial f_s}{\partial v_\perp} + k_\parallel \frac{\partial f_s}{\partial v_\parallel} \right) \frac{J_n^2 \left(\frac{k_\perp v_\perp}{\omega_s} \right)}{n \omega_s + k_\parallel v_\parallel - \omega - i\eta} \quad (5.15)$$

The integration has a singularity at

$$v_{\parallel} = \frac{\omega + i\eta - n\omega_s}{k_{\parallel}}$$

For an isotropic plasma species with Maxwellian velocity distribution (4.4), $a_{s\perp} = a_{s\parallel} = a_s$, (5.15) yields

$$\varepsilon(\mathbf{k}, \omega) = 1 + \sum_s \frac{k_s^2}{k^2} \left(1 + \sum_{n=-\infty}^{\infty} \frac{\omega}{\omega - n\omega_s} \left[W \left(\frac{\omega - n\omega_s}{|k_{\parallel}| a_s / \sqrt{2}} \right) - 1 \right] \right) \Lambda_n \left(\frac{k_{\perp}^2 a_s^2}{2\omega_s^2} \right) \quad (5.16)$$

For the magnetized species with a parallel beam, the longitudinal dielectric function similarly is

$$\varepsilon(\mathbf{k}, \omega) = 1 + \sum_s \frac{k_s^2}{k^2} \left(1 + \sum_{n=-\infty}^{\infty} \frac{\omega - k_{\parallel} u}{\omega - k_{\parallel} u - n\omega_s} \left[W \left(\frac{\omega - k_{\parallel} u - n\omega_s}{|k_{\parallel}| a_s / \sqrt{2}} \right) - 1 \right] \right) \Lambda_n \left(\frac{k_{\perp}^2 a_s^2}{2\omega_s^2} \right) \quad (5.16a)$$

Where the $k_s = 1/\lambda_s$ is the inverse of the Debye length of the s species, the Λ function is defined as before, and the W function is defined as

$$W(\beta) = \frac{1}{\sqrt{2\pi}} \int_{-\infty}^{\infty} \frac{x}{x - \beta - i\eta} e^{-\frac{x^2}{2}} dx \quad (5.17)$$

[Ichimaru, 1973], The relation between the W function and the regular plasma dispersion function or the Z function (B. D. Fried, S. D. Conte, the Plasma Dispersion Function) is

$$W(\beta) = 1 + \frac{\beta}{\sqrt{2}} Z \left(\frac{\beta}{\sqrt{2}} \right)$$

The W function also can be written

$$W(x) = 1 + \frac{x}{\sqrt{2\pi}} \int_{-\infty}^{\infty} \frac{\exp(-y^2)}{y - x/\sqrt{2}} + i\sqrt{\frac{\pi}{2}} x e^{-x^2} \quad (5.18)$$

so, the imaginary part of the W function is

$$W_i(x) = \sqrt{\frac{\pi}{2}} x e^{-x^2} \quad (5.19)$$

Inserting this expression into the expression for the longitudinal dielectric function (5.16), we have

$$\epsilon_i(\mathbf{k}, \omega) = \sum_s \frac{\sqrt{\pi} k_s^2}{k^2} \sum_{n=-\infty}^{\infty} \frac{\omega}{|k_{\parallel}| a_s} \Lambda_n \left(\frac{k_{\perp}^2 a_{s\perp}^2}{2\omega_s^2} \right) \exp \left[- \left(\frac{\omega - n\omega_s}{k_{\parallel} a_s} \right)^2 \right] \quad (5.20)$$

As we did above, we give the expression of the imaginary part of the longitudinal dielectric function for a plasma species with a streaming velocity parallel to the magnetic field \mathbf{B} :

$$\epsilon_i(\mathbf{k}, \omega) = \sum_s \frac{\sqrt{\pi} k_s^2}{k^2} \sum_{n=-\infty}^{\infty} \frac{\omega - k_{\parallel} u}{|k_{\parallel}| a_s} \Lambda_n \left(\frac{k_{\perp}^2 a_{s\perp}^2}{2\omega_s^2} \right) \exp \left[- \left(\frac{\omega - k_{\parallel} u - n\omega_s}{k_{\parallel} a_s} \right)^2 \right] \quad (5.20a)$$

where the k_s is the inverse of the Debye length of the s - species and u is the parallel streaming speed, so $\omega - k_{\parallel} u$ is the Doppler shifted frequency. Of course, this expression is very complicated. In order to see the rough shape of the power spectra, we can take the principal term ($n=0$ only) for a single species. We find that

$$\epsilon_i(\mathbf{k}, \omega, n=0) = \frac{\sqrt{\pi} k_s^2}{k^2} \frac{\omega}{|k_{\parallel}| a_{s\parallel}} \Lambda_0 \left(\frac{k_{\perp}^2 a_{s\perp}^2}{2\omega_s^2} \right) \exp \left[- \left(\frac{\omega}{k_{\parallel} a_{s\parallel}} \right)^2 \right] \quad (5.21)$$

$$\langle \rho^2(\mathbf{k}, \omega) \rangle = \frac{2\sqrt{\pi} e^2 n_s}{|k| a_{s\parallel}} \Lambda_0 \left(\frac{k_{\perp}^2 a_{s\perp}^2}{2\omega_s^2} \right) \exp \left[- \left(\frac{\omega}{k_{\parallel} a_{s\parallel}} \right)^2 \right] \quad (5.22)$$

Inserting (5.21) and (5.22) into Eq. (4.20), we have found that the power spectrum of the electric field fluctuation approximately obeys

$$\langle E^2(\mathbf{k}, \omega) \rangle = 8\pi \frac{T_s}{\omega} \pi \delta(\epsilon_r) \quad (5.23)$$

Here T_s is the temperature of the s species, and we used the relation

$$\lim_{\varepsilon_i \rightarrow 0} \frac{\varepsilon_i(\mathbf{k}, \omega)}{\varepsilon_r^2 + \varepsilon_i^2} = \pi \delta(\varepsilon_r) \quad (5.24)$$

According to the expression (5.23), we can see that the plasma fluctuation is roughly proportional to the plasma temperature T_s . Plasma fluctuations are due to the particle's thermal motion; without thermal motion, i.e. if $T_s = 0$, we will not observe this kind of fluctuation. This is the reason we call $\langle E^2(\mathbf{k}, \omega) \rangle$ the plasma thermal fluctuation spectrum.

Chapter 6

FLUCTUATIONS IN AN UNMAGNETIZED PLASMA

6.1 Power Spectrum of Charge Density

In the last chapter, we discussed the fluctuations due to the thermal motion of magnetized particles. We noticed that a magnetized plasma system with no DC electric field permits streaming only in the direction parallel to the magnetic field. This fluctuation theory of the magnetized species requires symmetry about the magnetic field \mathbf{B} . But for our situation, our perpendicular argon gun is directed almost perpendicular to the local magnetic field \mathbf{B} . The beam spreads over a wide pitch angle range, extending from almost 30° to 150° , or even wider. The existence of this kind of beam destroys the symmetry of the plasma system. To deal with this kind of problem, we must introduce one unmagnetized species into a magnetized plasma. This unmagnetized component provides a reasonable approximation to the perpendicular beam during the first gyration period ($\sim 50\mu s$) after the argon beam leaves the gun. During this interval, most particles are located around the field lines which pass the gun and the main payload, and the ion distribution function is approximately beam-like. At first, an unmagnetized species appears easier to analyze than a magnetized species. This is true if we don't include oblique streaming. For an unmagnetized plasma species which is not streaming along the lo-

cal magnetic field, the analysis will become complicated. It will be much more difficult if the streaming component has two temperatures. In fact, this is a common situation. The temperature along the streaming direction often is different from the temperature perpendicular to the streaming direction. In this section, we try to use some special techniques to solve this problem. First, we will choose a special coordinate frame to carry out the integration of the charge density and the longitudinal dielectric function. Then we will try to find a transformation from the beam frame to the frame of the wave vector \mathbf{k} . This transforms the two temperature distribution function of the streaming species into the \mathbf{k} frame.

We know that the charge density power spectrum for the unmagnetized species is

$$\langle \rho^2(\mathbf{k}, \omega) \rangle = 2\pi n_s e^2 \int d^3v f_s(\mathbf{v}) \delta(\omega - \mathbf{k} \cdot \mathbf{v}) \quad (5.8)$$

For a Maxwellian with a streaming velocity distribution function

$$f_s = \frac{1}{\pi^{3/2} a_x a_y a_z} \exp \left[- \left(\frac{(v_x - u_x)^2}{a_x^2} + \frac{(v_y - u_y)^2}{a_y^2} + \frac{(v_z - u_z)^2}{a_z^2} \right) \right] \quad (6.1)$$

where a_x, a_y, a_z are the three thermal speed components of the unmagnetized species; v_x, v_y, v_z are the three velocity components of the unmagnetized particles, and u_x, u_y, u_z are the streaming components of the unmagnetized species. Because we now don't have the magnetic field, we can further choose the \mathbf{k} direction as the z direction for convenience.

Now writing $\mathbf{k} \cdot \mathbf{v} = kv_{\parallel}$, substituting (6.1) into (5.8), and noticing that

$$\delta(\omega - \mathbf{k} \cdot \mathbf{v}) = \frac{\delta(v_{\parallel} - \omega/k)}{|\mathbf{k}|}$$

we get

$$\langle \rho^2(\mathbf{k}, \omega) \rangle = \frac{2\sqrt{\pi}n_s e^2}{ka_{s\parallel}} \exp \left[- \left(\frac{\omega - \mathbf{k} \cdot \mathbf{u}}{ka_{s\parallel}} \right)^2 \right] \quad (6.2)$$

This result shows us that the power spectrum of the charge density of the unmagnetized species depends only on the temperature along the \mathbf{k} direction $-a_{s\parallel}$.

6.2 Longitudinal Dielectric Function

The contribution to the longitudinal dielectric function from an unmagnetized species can be obtained through the integration of

$$\epsilon(\mathbf{k}, \omega) = -\frac{\omega_{p,s}^2}{k^2} \int d^3v \frac{1}{\mathbf{k} \cdot \mathbf{v} - \omega - i\eta} \mathbf{k} \cdot \frac{\partial f_s}{\partial \mathbf{v}} \quad (6.3)$$

where f_s is the normalized distribution function of the unmagnetized species. The integration in (6.3) is a three dimensional integration and with a singularity at

$$\mathbf{k} \cdot \mathbf{v} = \omega + i\eta$$

Normally, this integration is not easy to carry out. The problem can be understood by introducing three coordinates frames: beam \mathbf{u} frame, wave vector \mathbf{k} frame and, of course, the local magnetic field \mathbf{B} frame. We are treating one species with non - parallel streaming as in an unmagnetized plasma, and other species without streaming or with parallel streaming as

in a magnetized plasma. The question is: In which frame should we carry out the integration? In general, we have three choices, but the best one is the \mathbf{k} frame. We will see that in this frame the 3 - dimensional integration will be separated into three 1 - dimensional integrations. In the \mathbf{k} frame

$$\mathbf{k} \cdot \mathbf{v} = kv_z \quad (6.4)$$

and

$$\mathbf{k} \cdot \frac{\partial f_s}{\partial \mathbf{v}} = k \frac{\partial f_s}{\partial v_z} = -\frac{2k(v_z - u_z)}{a_z^2} f_s \quad (6.5)$$

Substituting (6.4), (6.5) and the definition of a normalized distribution function of an unmagnetized species (6.1) into (6.3), we have

$$\begin{aligned} \varepsilon(\mathbf{k}, \omega) = & \frac{2\omega_{p,s}^2}{\pi^{3/2} k a_x a_y a_z^3} \int_{-\infty}^{\infty} dv_x \exp\left(-\frac{(v_x - u_x)^2}{a_x^2}\right) \\ & \int_{-\infty}^{\infty} dv_y \exp\left(-\frac{(v_y - u_y)^2}{a_y^2}\right) \\ & \int_{-\infty}^{\infty} dv_z \frac{v_z - u_z}{kv_z - \omega - i\eta} \exp\left(-\frac{(v_z - u_z)^2}{a_z^2}\right) \end{aligned} \quad (6.6)$$

It is easy to see the results of integrations over v_x and v_y are

$$\sqrt{\pi} a_x \sqrt{\pi} a_y = \pi a_x a_y \quad (6.7)$$

For the third integration, over v_z

$$\int_{-\infty}^{\infty} dv_z \frac{v_z - u_z}{kv_z - \omega - i\eta} \exp\left(-\frac{(v_z - u_z)^2}{a_z^2}\right) \quad (6.8)$$

There is a singularity at

$$v_z = \frac{\omega + i\eta}{k}$$

It is easy to imagine a relationship between it and the plasma dispersion function, Z , or the W function. Here we will try to find the relationship to the W function. First we will change variables by letting

$$X \equiv \frac{\sqrt{2}(v_z - u_z)}{a_z}$$

Then

$$v_z - u_z = \frac{a_z X}{\sqrt{2}}$$

and

$$dv_z = \frac{a_z dX}{\sqrt{2}}$$

Then substitute these into the integration (6.8). After few steps of algebraic operations, we find that the integral equals

$$\frac{a_z}{k} W\left(\frac{\omega - ku_z}{ka_z/\sqrt{2}}\right)$$

Finally putting the three integrals together, the longitudinal dielectric function for an unmagnetized species is

$$\varepsilon(\mathbf{k}, \omega) = \frac{2\omega_{p,s}^2}{\sqrt{\pi}k^2 a_z^2} W\left(\frac{\omega - ku_z}{ka_z/\sqrt{2}}\right) = \frac{k_s^2}{\sqrt{\pi}k^2} W\left(\frac{\omega - ku_z}{ka_z/\sqrt{2}}\right) \quad (6.9)$$

where

$$k_s^2 = \frac{2\omega_p^2}{a_z^2} = \frac{1}{\lambda_d^2}$$

From this result, we find that as in the expression for the charge density spectrum (6.2), the dependence on the thermal speed or temperature involves components only along the direction of wave vector \mathbf{k} . Incidentally, the imaginary part of the longitudinal dielectric function for an unmagnetized species is

$$\varepsilon_i(\mathbf{k}, \omega) = \frac{\sqrt{\pi}\omega_{p,s}^2}{k^3 a_z^3} (\omega - ku_z) \exp\left(-\frac{(\omega - ku_z)^2}{ka_z^2}\right) \quad (6.10)$$

6.3 Temperature Transformation

At this point, we have found expressions for the charge density spectrum and the longitudinal dielectric function for an unmagnetized species. The expressions seem pretty simple because both of them depend on the z component or parallel (to \mathbf{k}) component of the thermal speed of the unmagnetized particles. A remaining question is, what is a_z ? Do we already know the thermal speed along the \mathbf{k} direction? The answer is no. Actually, it is almost impossible to measure the thermal speeds along all possible \mathbf{k} directions, and on the R29015 flight, we have only very limited thermal speed measurements. In general, when we say we know the properties of a beam that is streaming along a certain direction, we mean that we know the average velocity of the species and that we also know the components of the thermal speed of the species in three dimensional space. For example, a two temperature plasma distribution function can be written as

$$f_s(v_{\parallel}, v_{\perp}) = \frac{1}{\pi^{3/2} a_{s\perp}^2 a_{s\parallel}} \exp \left[- \left(\frac{v_{\perp}^2}{a_{s\perp}^2} + \frac{(v_{\parallel} - U)^2}{a_{s\parallel}^2} \right) \right] \quad (6.11)$$

This means $a_{s\parallel}, a_{s\perp}$ are the thermal speeds along the directions parallel and perpendicular to the streaming direction, respectively, and u is the bulk velocity of the beam. This description of the distribution function is valid in the beam or u frame. Normally we measure the components of the temperature of a streaming species along the streaming direction and perpendicular to the direction of streaming. What is the relationship between the temperature in the u frame and the \mathbf{k} frame? How can we use the distribution function of the unmagnetized species in the u frame

to express the distribution function of this species in the \mathbf{k} frame. Frankly there does not exist an explicit way to carry the transformation of the distribution function from the \mathbf{u} frame to the \mathbf{k} frame. The use of distributions such as (6.1) or (6.11) implies that all distributions are *Maxwellian*. Unfortunately, this is not always true. If a distribution is a *Maxwellian* in the \mathbf{u} frame, it is in general not a *Maxwellian* distribution in the \mathbf{k} frame. However, if the two temperature components of the species in \mathbf{u} frame are not dramatically different, then we can still approximate the distribution function of the species as a *Maxwellian* with new temperature components in the \mathbf{k} frame. The relationship between the three frames: the \mathbf{B} frame, the \mathbf{k} frame and the \mathbf{u} frame, is shown in Fig D-1.

As was noted in chapter 4, the thermal speed is determined by the mean value of the kinetic energy of the all particles. The \hat{z} component of the temperature is

$$T_z = 2 \int_{-\infty}^{\infty} \frac{1}{2} m v_z^2 f_s dv_x dv_y dv_z \quad (6.12)$$

where v_z is the velocity along the \mathbf{k} direction. This velocity can be obtained by transforming from the \mathbf{u} frame through the \mathbf{B} frame to the \mathbf{k} frame. The matrix of the transformation is (see Appendix D):

$$\mathfrak{R} = \begin{pmatrix} \cos \theta \cos \beta \cos \alpha + \sin \theta \sin \alpha & -\cos \theta \sin \beta & \cos \theta \cos \beta \sin \alpha - \sin \theta \cos \alpha \\ \sin \beta \cos \alpha & \cos \beta & \sin \beta \sin \alpha \\ \sin \theta \cos \beta - \cos \theta \sin \alpha & \sin \theta \sin \beta & \sin \theta \cos \beta \sin \alpha + \cos \theta \cos \alpha \end{pmatrix} \quad (6.13)$$

If we call the elements in the last row of the matrix above

$$A = \sin \theta \cos \beta - \cos \theta \sin \alpha$$

$$B = \sin \theta \sin \beta$$

$$C = \sin \theta \cos \beta \sin \alpha + \cos \theta \cos \alpha \quad (6.13a)$$

then

$$v_z = Aw_x + Bw_y + Cw_z \quad (6.14)$$

Then

$$v_z^2 = A^2 w_x^2 + B^2 w_y^2 + C^2 w_z^2 + ABw_x w_y + ACw_x w_z + BCw_y w_z \quad (6.14a)$$

where w_x, w_y, w_z are the three components of the velocity of the unmagnetized species in the U frame. Substituting (6.14a) and the distribution function (6.11) into the integration (6.12), we can drop the all mixed terms and that find the temperature along the k direction obeys

$$\begin{aligned} T_z &= \frac{m}{\pi^{3/2} a_{s\perp}^2 a_{s\parallel}} \\ &\times [A^2 \int_{-\infty}^{\infty} w_x^2 \exp\left(-\frac{w_x^2}{a_{\perp}^2}\right) dw_x \int_{-\infty}^{\infty} \exp\left(-\frac{w_y^2}{a_{\perp}^2}\right) dw_y \int_{-\infty}^{\infty} \exp\left(-\frac{w_z^2}{a_{\parallel}^2}\right) dw_z \\ &+ B^2 \int_{-\infty}^{\infty} \exp\left(-\frac{w_x^2}{a_{\perp}^2}\right) dw_x \int_{-\infty}^{\infty} w_y^2 \exp\left(-\frac{w_y^2}{a_{\perp}^2}\right) dw_y \int_{-\infty}^{\infty} \exp\left(-\frac{w_z^2}{a_{\parallel}^2}\right) dw_z \\ &+ C^2 \int_{-\infty}^{\infty} \exp\left(-\frac{w_x^2}{a_{\perp}^2}\right) dw_x \int_{-\infty}^{\infty} \exp\left(-\frac{w_y^2}{a_{\perp}^2}\right) dw_y \int_{-\infty}^{\infty} w_z^2 \exp\left(-\frac{w_z^2}{a_{\parallel}^2}\right) dw_z] \end{aligned} \quad (6.15)$$

It is easy to find that

$$\begin{aligned} T_z &= \frac{m}{\pi^{3/2} a_{s\perp}^2 a_{s\parallel}} [A^2 \frac{\sqrt{\pi}}{2} a_{\perp}^3 \sqrt{\pi} a_{\perp} \sqrt{\pi} a_{\parallel} \\ &+ B^2 \sqrt{\pi} a_{\perp} \frac{\sqrt{\pi}}{2} a_{\perp}^3 \sqrt{\pi} a_{\parallel} \\ &+ C^2 \sqrt{\pi} a_{\perp}^3 \sqrt{\pi} a_{\perp} \frac{\sqrt{\pi}}{2} a_{\parallel}^3] \end{aligned} \quad (6.16)$$

or

$$T_z = \frac{m}{2} [(A^2 + B^2) a_{\perp}^2 + C^2 a_{\parallel}^2] = (A^2 + B^2) T_{\perp} + C^2 T_{\parallel} \quad (6.16a)$$

and that the streaming speed along the \mathbf{k} direction is

$$u_z = CU \quad (6.17)$$

Now we have found all the parameters which we need to evaluate the longitudinal dielectric function of an unmagnetized plasma species by inserting (6.16) or (6.16a) and (6.17) into (6.9) and (6.10). For convenience, we will now summarize our results for the unmagnetized plasma species.

SUMMARY:

An unmagnetized two - temperature species streaming in an arbitrary direction, is described by the distribution function

$$f_s(v_{\parallel}, v_{\perp}) = \frac{1}{\pi^{3/2} a_{s,\perp}^2 a_{s,\parallel}} \exp \left[- \left(\frac{v_{\perp}^2}{a_{s,\perp}^2} + \frac{(v_{\parallel} - U)^2}{a_{s,\parallel}^2} \right) \right] \quad (6.11)$$

The power spectrum of electric field fluctuations from this species is

$$\langle E^2(\mathbf{k}, \omega) \rangle = \frac{16\pi^2 \langle \rho^2(\mathbf{k}, \omega) \rangle}{k^2 |\epsilon(\mathbf{k}, \omega)|^2} \quad (4.20)$$

where the charge density spectrum is

$$\langle \rho^2(\mathbf{k}, \omega) \rangle = \frac{2\sqrt{\pi} n_s e^2}{k a_{s,\perp}} \exp \left[- \left(\frac{\omega - \mathbf{k} \cdot \mathbf{u}}{k a_{s,\parallel}} \right)^2 \right] \quad (6.2)$$

The contribution of this species to the longitudinal dielectric function is

$$\epsilon(\mathbf{k}, \omega) = \frac{2\omega_{p,s}^2}{\sqrt{\pi} k^2 a_z^2} W \left(\frac{\omega - k u_z}{k a_z / \sqrt{2}} \right) = \frac{1}{k^2 \lambda_d^2} W \left(\frac{\omega - k u_z}{k a_z / \sqrt{2}} \right) \quad (6.9)$$

The imaginary part of the unmagnetized species contribution to the longitudinal dielectric function is

$$\epsilon_i(\mathbf{k}, \omega) = \frac{\sqrt{\pi} \omega_{p,s}^2}{k^3 a_z^3} (\omega - k u_z) \exp \left(- \frac{(\omega - k u_z)^2}{k a_z^2} \right) \quad (6.10)$$

where a_z is the thermal speed along the \mathbf{k} direction

$$a_z = (A^2 + B^2)a_{\perp} + C^2 a_{\parallel} \quad (6.18)$$

and u_z is the streaming component along \mathbf{k}

$$u_z = CU \quad (6.17)$$

Here U is the streaming speed, and the transformation coefficients are given by (6.13a)

$$\begin{aligned} A &= \sin \theta \cos \beta - \cos \theta \sin \alpha \\ B &= \sin \theta \sin \beta \\ C &= \sin \theta \cos \beta \sin \alpha + \cos \theta \cos \alpha \end{aligned} \quad (6.13a)$$

As we see in the Fig. D-1, θ and α are the pitch angles of the wave vector \mathbf{k} , and the streaming vector U respectively, and the β is the azimuthal angle of the streaming vector U from the $\mathbf{B} - \mathbf{k}$ plane. At this point, we have found a complete kinetic theory of plasma thermal fluctuations. According to this theory, we can calculate the power spectrum of the charge density $\langle \rho^2(\mathbf{k}, \omega) \rangle$, the longitudinal dielectric function $\epsilon(\mathbf{k}, \omega)$ and the power spectrum of the electric field fluctuations due to thermal motions. In the next chapter, we will use the theory to study waves detected by electric field antennas on rocket flight R29015 rocket.

Chapter 7

O^+ ACOUSTIC WAVES AND FLUCTUATIONS

In Chapters 4, 5 and 6, we found a complete kinetic theory of plasma thermal fluctuations. According to this theory, we can calculate the power spectrum of the charge density $\langle \rho^2(\mathbf{k}, \omega) \rangle$, the longitudinal dielectric function $\epsilon(\mathbf{k}, \omega)$ and the power spectrum of the electric field fluctuation $\langle E^2(\mathbf{k}, \omega) \rangle$ due to the thermal motions of the plasma species. The theory can deal with a magnetized species with or without streaming parallel to the magnetic field \mathbf{B} , and this theory is also valid for unmagnetized two-temperature plasma species with streaming in any direction.

From Fig. 4-1, we can see that there is a smooth background noise exists for the $2 \perp$, $3 \perp$, $4 \perp$ and $5 \perp$ events. For the $2 \perp$ event, the spectral density level was pretty high, around $10^{-2}(mv/m)^2/Hz$. After the gun was turned off, the spectral density of the noise dropped to almost zero. For the $3 \perp$ and $5 \perp$ events, the spectral densities of the noise were about $10^{-4}(mv/m)^2/Hz$. For all the perpendicular events, the intense noise was seen in the frequency range from 50Hz to 400Hz. In this chapter, we will use the fluctuation theory to give a quantitative answer to the question: was the background noise produced by thermal fluctuations?

7.1 Isofrequency Contours

Before carrying out the actual calculations, we introduce a necessary and useful concept -- that of an isofrequency contour. According to expression (4.20), we can evaluate the power spectrum of the electric field fluctuations. This is the power in electric field fluctuations per unit wave vector and per unit angular frequency. However the experiment didn't obtain any wavelength information. The actual observations were of total power in the electric fluctuations per unit angular frequency from all possible wave vectors. To make a comparison with the observations, we must take an inverse Fourier Transformation on the power spectrum of electric field fluctuations, i.e.

$$\langle E^2(\omega) \rangle = \left| \frac{1}{8\pi^3} \int d\mathbf{k} \sqrt{\langle E^2(\mathbf{k}, \omega) \rangle} e^{i\mathbf{k} \cdot \mathbf{r}} \right|^2 \quad (7.1)$$

where

$$\int d\mathbf{k} = \int_0^{2\pi} d\phi \int_0^\infty k_\perp dk_\perp \int_{-\infty}^\infty dk_\parallel$$

For a spatially uniform plasma, the electric field fluctuations are independent of \mathbf{r} , so we can pick $\mathbf{r} = 0$. Then (7.1) reduces to

$$\langle E^2(\omega) \rangle = \left| \frac{1}{8\pi^3} \int d\mathbf{k} \sqrt{\langle E^2(\mathbf{k}, \omega) \rangle} \right|^2 \quad (7.1a)$$

where the integrated function

$$\sqrt{\langle E^2(\mathbf{k}, \omega) \rangle} = \frac{4\pi}{k} \frac{\sqrt{\langle \rho^2(\mathbf{k}, \omega) \rangle}}{\sqrt{\epsilon_r^2 + \epsilon_i^2}} \quad (7.1b)$$

We know that

$$\lim_{\epsilon_i \rightarrow 0} \frac{\epsilon_i}{\epsilon_r^2 + \epsilon_i^2} = \pi \delta(\epsilon_r)$$

For small ϵ_i , the integral (7.1a) is equivalent to

$$\langle E^2(\omega) \rangle = \left| \int d\mathbf{k} \frac{\sqrt{\langle \rho^2(\mathbf{k}, \omega) \rangle}}{k} \frac{\delta(\epsilon_r)}{2\pi} \frac{\sqrt{\epsilon_r^2 + \epsilon_i^2}}{\epsilon_i} \right|^2$$

or

$$\langle E^2(\omega) \rangle = \frac{1}{4\pi^2} \left| \int d\mathbf{k} \frac{\sqrt{\langle \rho^2(\mathbf{k}, \omega) \rangle}}{k} \frac{\delta(\mathbf{k} - \mathbf{k}_0)}{\left| \frac{\partial \epsilon_r}{\partial \omega} \right| |v_g|} \frac{\sqrt{\epsilon_r^2 + \epsilon_i^2}}{\epsilon_i} \right|^2 \quad (7.2)$$

Where $v_g = \frac{\partial \omega}{\partial \mathbf{k}}$ is the group velocity of the wave, and the \mathbf{k}_0 is the value of \mathbf{k} which corresponding to the normal modes, i.e. $\epsilon_r(\mathbf{k}, \omega) = 0$. Due to the delta function in the integral (7.2), the two dimensional integration on the $k_{\parallel} - k_{\perp}$ plane will further reduce to a line integral along the isofrequency contour of a normal mode. The final expression for the electric field power spectrum is

$$\langle E^2(\omega) \rangle = \frac{1}{4\pi^2} \left| \int_0^{2\pi} d\phi \int_{\epsilon_r=0} \frac{k_{\perp}}{k} \frac{\sqrt{\langle \rho^2(\mathbf{k}, \omega) \rangle}}{\left| \frac{\partial \epsilon_r}{\partial \omega} \right| |v_g|} dk_l \right|^2 \quad (7.3)$$

This is the power spectrum of electric field fluctuations per angular frequency. If we want to express the frequency in Hz , Eq. (7.3) becomes

$$E^2(f) = \frac{1}{8\pi^3} \left| \int_0^{2\pi} d\phi \int_{\epsilon_r=0} \frac{k_{\perp}}{k} \frac{\sqrt{\langle \rho^2(\mathbf{k}, \omega) \rangle}}{\left| \frac{\partial \epsilon_r}{\partial \omega} \right| |v_g|} dk_l \right|^2 \quad (7.4)$$

Where dk_l is the integration element along the isofrequency contour. This is the expression that will be used to calculate the power of electric field fluctuations per unit frequency. Fig. 7-1 shows the isofrequency integration contour, where dk_l is the integration element along the isofrequency contour.

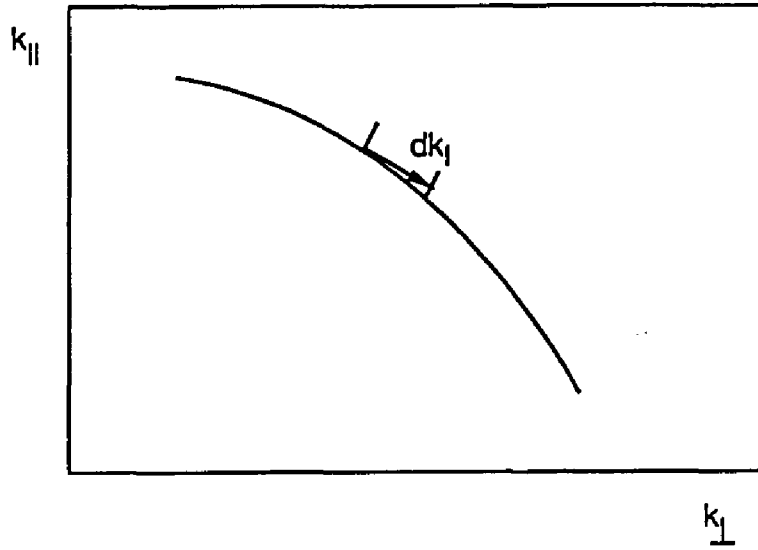


Fig. 7-1 The Isofrequency Integration Contour

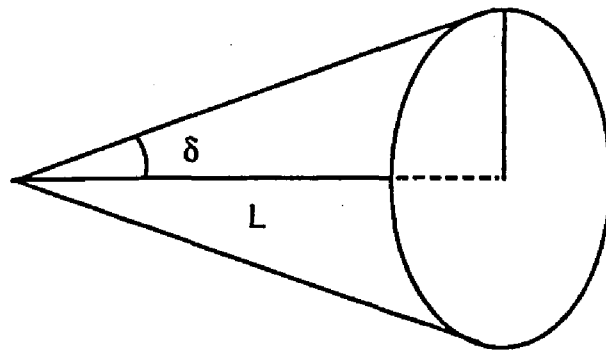


Fig. 7-2 The Argon Beam Open Angle

7.2 O⁺-Acoustic Wave Fluctuations

From Fig. 4-1, we have seen the low frequency background noise is associated with the presence of the argon beam. We also have seen the frequency range of the noise is from 50Hz to 500Hz, which is in the frequency range of the ionospheric O⁺-Acoustic wave, and that the background noise spectra are smooth and continuous. It is reasonable to imagine that the noise was generated by thermal fluctuations in the O⁺-Acoustic wave mode, driven by the argon beam. To verify this hypothesis, we use all available plasma parameters to calculate the thermal fluctuations excited directly by the artificial argon ion beam. To estimate the argon beam density, we assume that the beam ions followed straight lines, and that they formed a cone when the argon ions left the gun chamber. When the sub-payload was not too far from the main payload, the density of the argon beam is expected to be

$$n = \frac{I}{\pi e L^2 v \tan^2 \delta} \quad (7.5)$$

where I is the particle current. For our case I is 0.1 Ampere, i.e. $\frac{1}{1.6} \times 10^{18}$ ions left the gun chamber per second. Here, L is the distance from the gun, δ is the half width of the beam, and v is the speed of an argon ion with an energy of 100ev. The assumed beam structure is shown in the figure 7-2.

The densities calculated for different distances are

Table 7-1 Argon Density Near The Gun

distance,m	0.01	1	10	50	100
density, cm^{-3}	10^{10}	10^6	10^4	4×10^2	10^2

where the distance is the perpendicular distance from the gun's aperture, and the densities are argon ion densities in units of cm^{-3} . From table 7-1, we can see that the argon ion density is expected to be about $400/cm^3$ at a distance of 50 meters, the perpendicular separation distance for the $2 \perp$ firing. This density is too low to produce waves such as O^+ acoustic waves at a frequency near a few hundred Hz .

In order to produce O^+ -Acoustic wave, we have to raise the density of argon ions. Figures 7-3a and 7-3b show the longitudinal dielectric function of a four species plasma. The density (DENS, *particles/cm³*), parallel component of temperature (TPAR), perpendicular component of temperature (TPER, $^{\circ}K$), cyclotron frequency (WC), plasma frequency (WP, rad./s), thermal speed (THML, cm/s), maximum term number of harmonics (MX) and magnetized or unmagnetized status (Y: magnetized; N: unmagnetized) are shown in Fig. 7-3a, 7-3b, 8-9a, 8-9b. We defined e^- as species 1, O^+ as species 2, He^+ as species 4 and Ar^+ as species 6, so the mark C2 represents the cyclotron frequency of species 2, and the mark P2 represents the plasma frequency of species 2. The solid curved line shows the real part of the longitudinal dielectric function ϵ_r , and the dashed curved line shows the imaginary part of it.

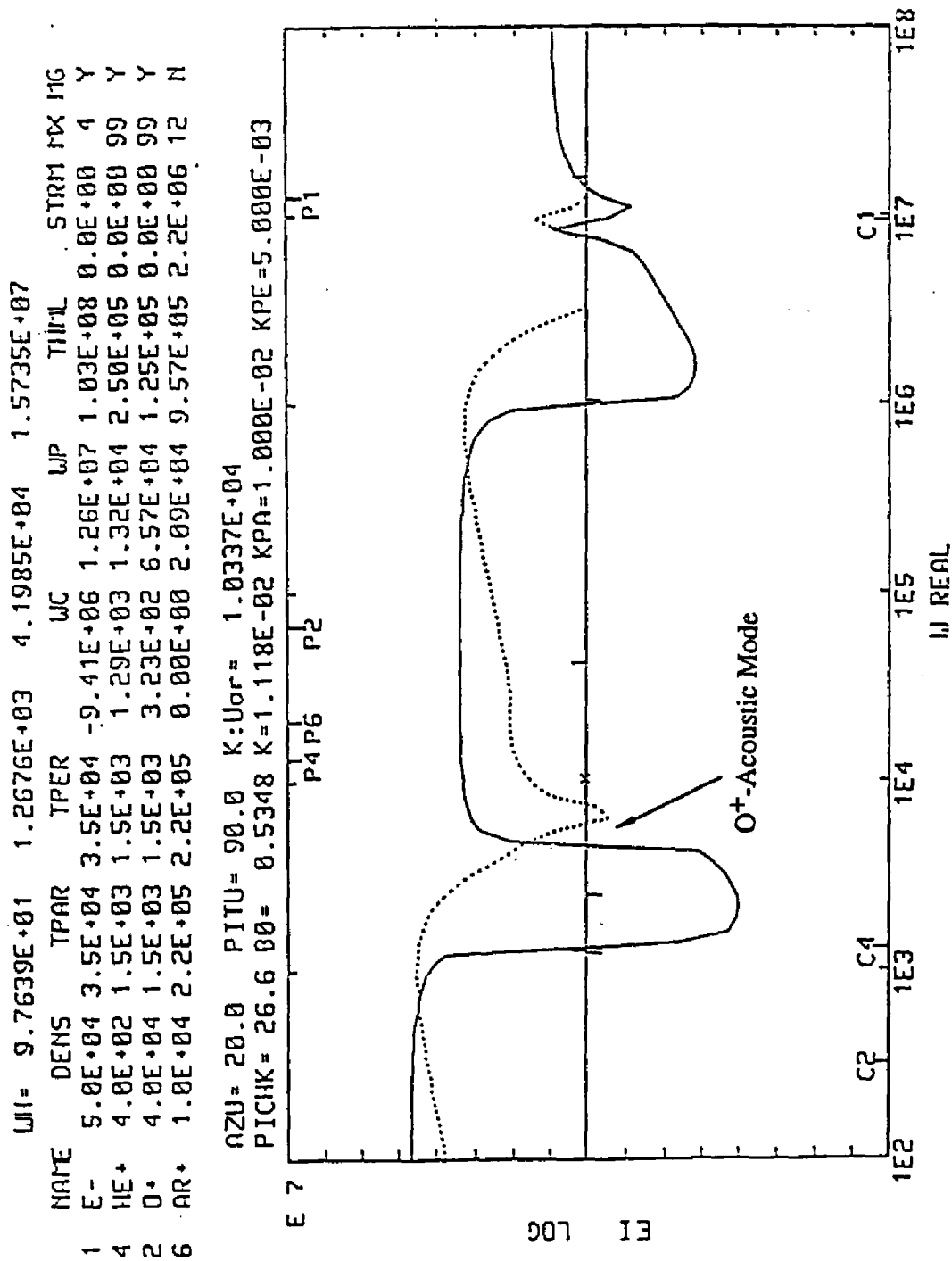


Fig. 7-3a Dielectric Function, 3ev e⁻, O⁺-Acoustic Wave

LH= 9.7639E+01 1.2676E+03 4.1985E+04 1.5735E+07
 NAME DENS TPAR TPER LUC LUP THML STRM PX MG
 1 E- 5.0E+04 5.0E+04 5.0E+04 -9.41E+06 1.26E+07 1.23E+08 0.0E+00 4 Y
 4 HE+ 4.0E+02 1.5E+03 1.5E+03 1.29E+03 1.32E+04 2.50E+05 0.0E+00 99 Y
 2 O+ 4.0E+04 1.5E+03 1.5E+03 3.23E+02 6.57E+04 1.25E+05 0.0E+00 99 Y
 6 AR+ 1.0E+04 2.2E+05 2.2E+05 0.00E+00 2.09E+04 9.57E+05 2.2E+06 12 N

AZU= 0.0 PITU= 90.0 K:Uor= 1.1000E+04
 PICHK= 26.6 B0= 0.5348 K-1.118E-02 KPA=1.000E-02 KPE=-5.000E-03

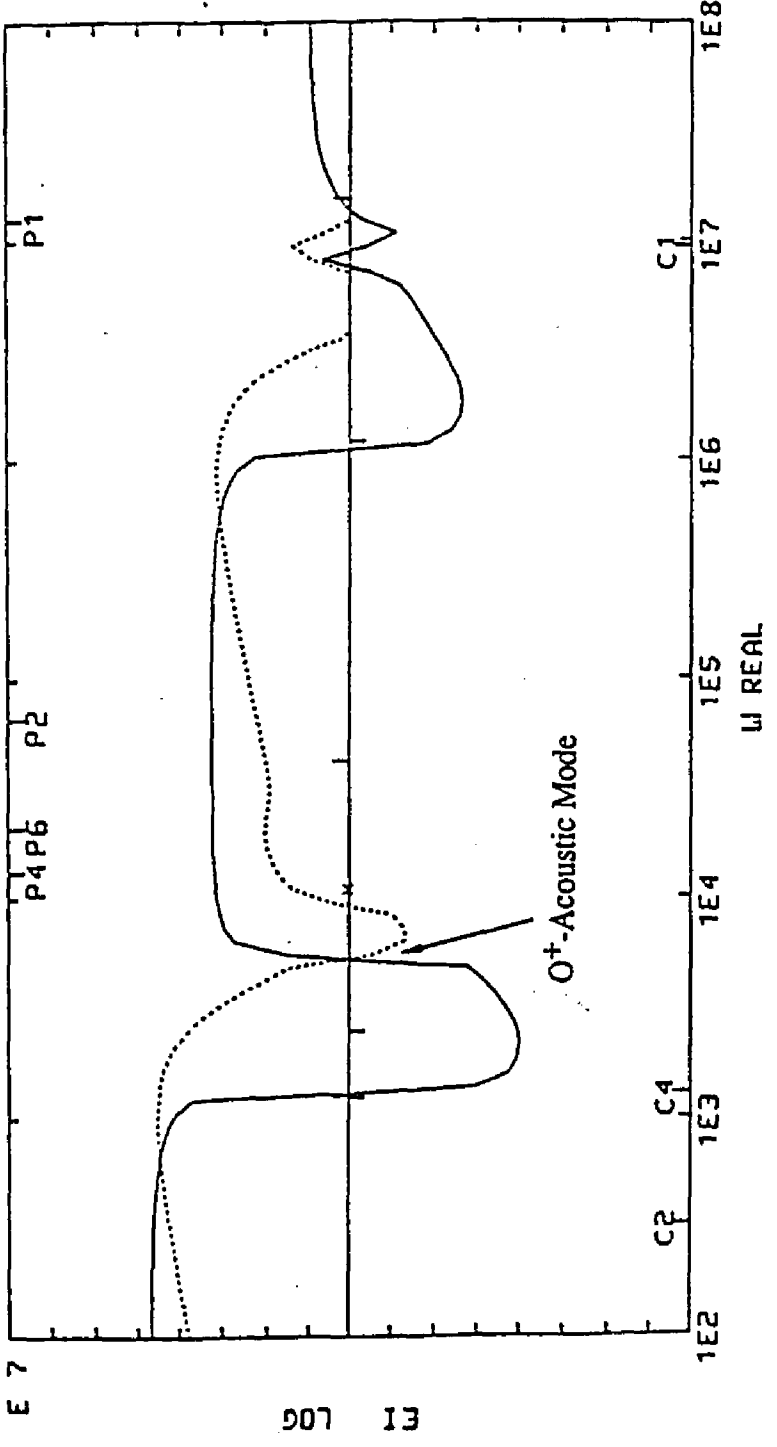


Fig. 7-3b Dielectric Function, 4.5ev e^- , O^+ -Acoustic Wave

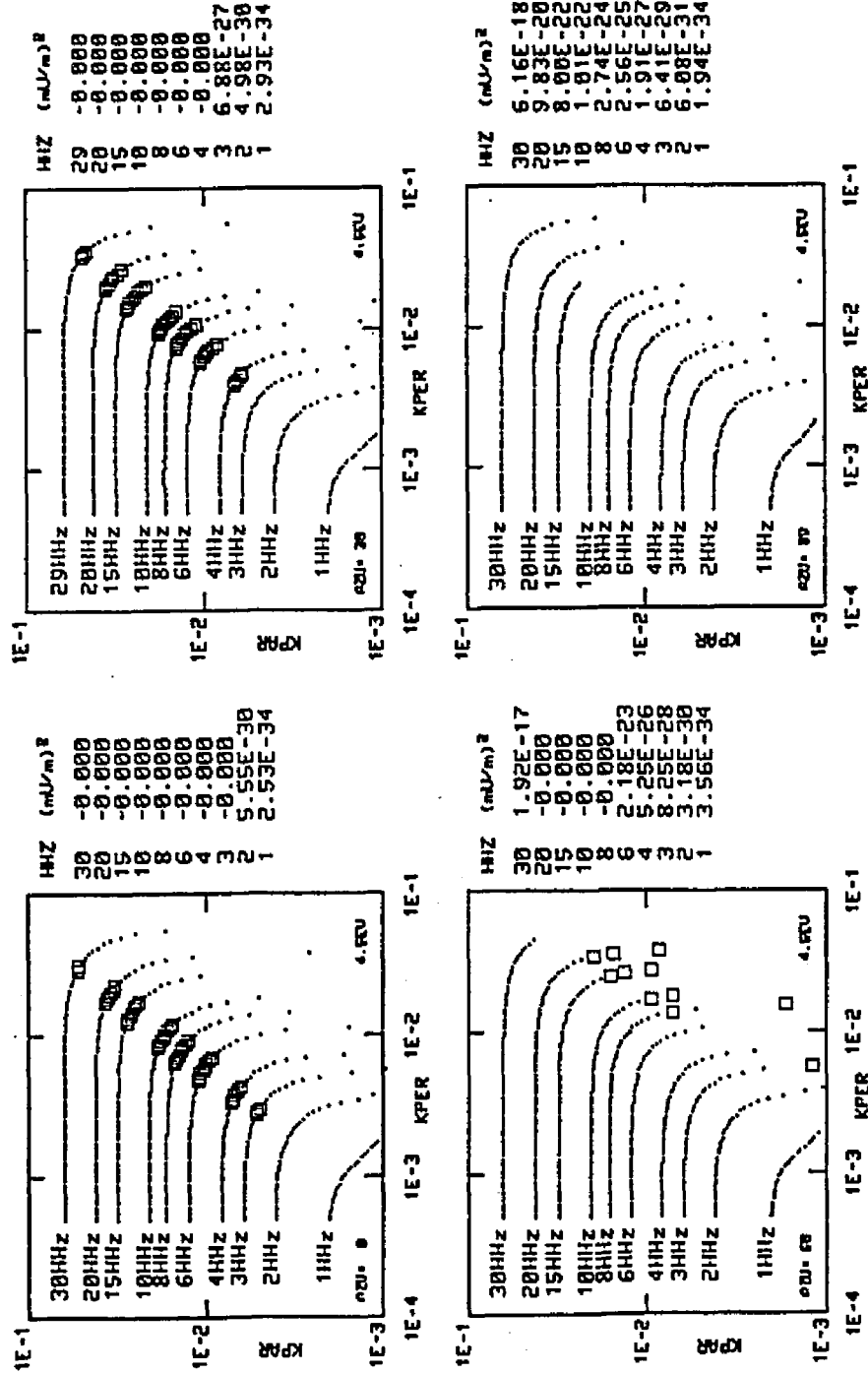


Fig. 7-4a Isofrequency Contour of O^+ -Acoustic Wave, $0 - 89^\circ$

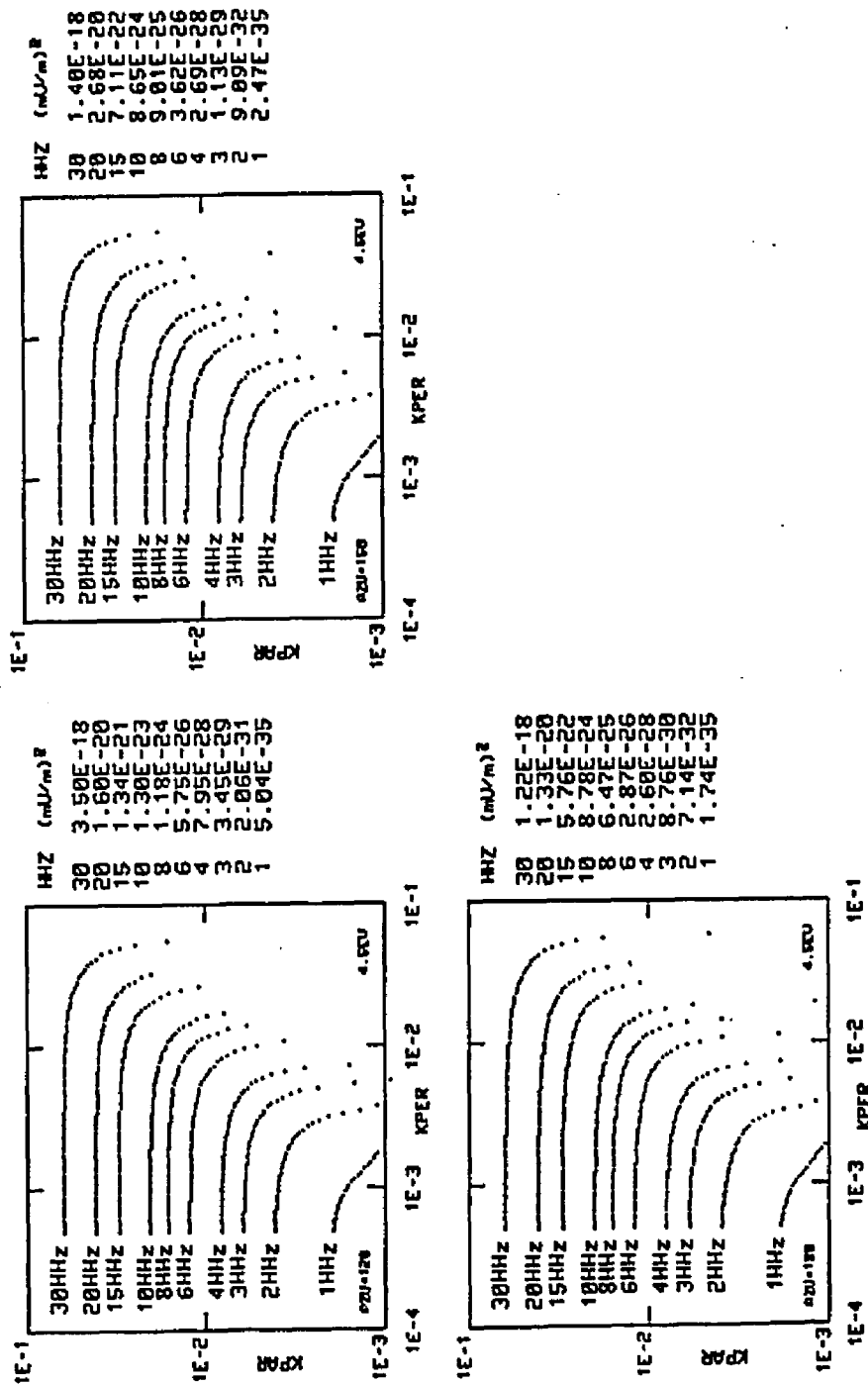


Fig. 7-4b Isofrequency Contour of O⁺-Acoustic Wave, 90 - 180°

In Fig. 7-3a, the principal ion species is oxygen with a density of $4 \times 10^4/cm^3$, as measured by the Stanford Research Institute (SRI) radar. Also included are 1 percent of He^+ with the temperature of $1500^\circ K$, and electrons with the temperature of 3ev. The unmagnetized argon species, with a streaming energy of 100ev, has a density of $10^4/cm^3$ and a temperature of 20ev. From this figure, we can see that ϵ_i - the imaginary part of the dielectric function, is so high near the O^+ ion acoustic wave normal modes ($\sim 800Hz$) that the wave amplitudes easily were damped, and could not produce observable electric fields.

To make a more intense wave, we raised the electron temperature to 4.5ev. Here it is assumed that the ionospheric cold electrons ($1500^\circ K$) were heated by the hot electrons from the ion gun. This assumption is reasonable because the Ar^+ beam was emitted along with hot electrons (few ev) whenever the gun was firing. Figure 7-3b is similar to figure 7-3a, except the electron temperature was changed to 4.5ev. This figure shows an O^+ ion acoustic mode near 470 Hz with a very small ϵ_i , suggesting that the wave mode could be unstable. Starting from this mode, and using the theory and the technique we developed in section (7.1), we traced out the isofrequency contours for frequencies from 100 Hz to 3000 Hz. Along the isofrequency contours, each dot represents a stable (or damped) wave mode, and each square represents a unstable wave mode. Figures 7-4a and 7-4b show contours for the same plasma parameters (densities, temperatures, streaming speeds) which were defined in Fig. 7-3b, except the streaming direction has been changed. The angle A_{zu} represent the azimuthal angle of the beam from the $B - k$ plane. Figure 7-4a and figure 7-4b show two very interesting features.

The first one is that there is a cutoff limit for the O^+ -Acoustic wave mode, i.e. the O^+ -Acoustic wave mode will not propagate when the pitch angle of \mathbf{k} is increased to a certain angle ($\sim 40^\circ$). The second one is that when A_{zu} is smaller, the unstable Ion-Acoustic waves were produced in a small \mathbf{k} space region. This unstable region shifted towards larger pitch angles until they met the cutoff limit as A_{zu} increased. The third feature is that large k_{\parallel} correspond to high frequency waves. Due to this fact, and the fact that the Ion - Acoustic wave has a pitch angle cutoff, the analysis tells us further that high frequency acoustic waves should have longer isofrequency contours, so they could have higher power spectra of electric field fluctuations.

We calculated the power spectra of electric field fluctuations along each isofrequency contour and summed over the different azimuthal angles A_{zu} . The results are shown in table 7-2.

**Table 7-2 Power Spectrum of Electric Field
Fluctuations of 4.5ev e^- , $(mV/m)^2/Hz$**

Az-u	100Hz	200Hz	600Hz	1000Hz	2000Hz
0°	2.5×10^{-34}	5.6×10^{-30}	UST	UST	UST
30°	2.9×10^{-34}	5.0×10^{-30}	UST	UST	UST
60°	3.6×10^{-34}	3.2×10^{-30}	2.2×10^{-23}	UST	UST
89°	1.9×10^{-34}	6.1×10^{-31}	2.6×10^{-25}	1.0×10^{-22}	9.8×10^{-20}
120°	5.0×10^{-35}	2.1×10^{-31}	5.8×10^{-26}	1.3×10^{-23}	1.6×10^{-20}
150°	2.5×10^{-35}	9.1×10^{-32}	3.6×10^{-26}	8.7×10^{-24}	2.7×10^{-20}
180°	1.7×10^{-35}	7.1×10^{-32}	2.9×10^{-26}	8.8×10^{-24}	1.3×10^{-20}
total power	1.7×10^{-33}	9.0×10^{-29}	UST	UST	UST

Where Az-u is the azimuthal angle of the beam u from the B - k plane, and UST means the waves is unstable. The numbers in table 7-2 show the power spectra of electric field fluctuations for different Az-u and frequencies, in units of $(mV/M)^2/Hz$. The total power means the total power spectral density of electric field fluctuations for a certain frequency, they were summed over all possible Az-u angles for frequency at which the waves are stable. From the above figures and table, we can see that the power spectra of electric fluctuations for a stable O^+ -acoustic wave (100Hz to 1000Hz) are around of $10^{-28}(mV/m)^2/Hz$. These magnitudes are much lower than the received noise level (10^{-4} to $10^{-3}(mV/m)^2/Hz$).

It still is possible that the noise was a growing O^+ -Acoustic wave driven by the Ar^+ beam. To investigate this, we calculated the growth lengths for above plasma with zero azimuthal angle. This is the angle at which growth is most rapid. The calculated results are shown in table 7-3.

Table 7-3 O^+ -Acoustic Wave Growth Lengths, M

angle	300Hz	400Hz	600Hz	800Hz	1000Hz	2000Hz
26°	1.5×10^4	600	250	170	130	130
29°	1.3×10^3	360	160	110	90	60
32°	1.5×10^3	350	160	110	90	60
35°	stable	900	250	170	110	90

Where "angle" is the angle between wave vector \mathbf{k} and magnetic field \mathbf{B} . From this table we can see that the growth lengths are long compared to the size of the artificial argon beam ($\leq 50m$). We know that if the size of a physical region equals the growth length, then the wave amplitude will be amplified by a factor of e . If a physical region is n times the growth length, then the growing wave amplitude will be amplified a factor of e^n . If we want to amplify a wave up to 100 times its original amplitude, the physical region size should $2\ln 10$, i.e. ~ 5 times the growth length. These results suggest to us that the received noise was not likely to be thermal fluctuations associated with the O^+ -Acoustic wave, if the plasma parameters we used in the calculations and the measured noise level are correct.

Chapter 8

EIC WAVES, BIHYBRID WAVES AND INSTABILITY

8.1 Observations of EIC Waves

As we mentioned before, on rocket R29015 the wave receiver received a variety of waves, such as signals at multiples of the hydrogen cyclotron frequency and the lower hybrid wave [Kintner *et al.*, 1986]. The University of Minnesota's automatic gain controlled wave receiver [Erlandson *et al.*, 1987], observed several features extending through most of the receiver record (figure 8-1, 8-2 and 8-3). First, two narrow horizontal lines near 2.5 and 3.3 kHz are interference signals from other experiments on the main payload. Second, there is a broad band emission from 8 kHz to 10kHz. Erlandson *et al.* [1987] refer to this band as the lower part of the auroral VLF hiss spectrum, with a cutoff at the lower hybrid resonance frequency. Third, and of most interest to us, is a low frequency band around a few hundred Hz.

Figures 8-4a (188.71s to 190.03s) and 8-4b (193.99s to 195.43s) show intense low frequency waves with a clear modulation at the sub-payload spin frequency, and some pulsations with the frequencies ranging from 50Hz to 10KHz. From this figure, we can also see that a high frequency noise (\sim 8KHz to 10KHz) appeared to decrease dramatically when the 2 \perp gun was turned on around 189.0s. We understand this phenomena as the

result of the high frequency receiver's automatic gain control.

Fig. 8-5a (187s to 192s) and 8-5b (300s to 302s) show the Fourier spectra of low frequency signals received by the DCE receiver. We know that the $2 \perp$ firing was started at 189.0s, so we can see an apparent association between low frequency waves and the ion firing in Fig. 8-5a. Fig. 8-5b, for the $4 \perp$ ion gun firing, shows that the intense wave at a frequency $\sim 180Hz$ has a clear ion gun spin modulation.

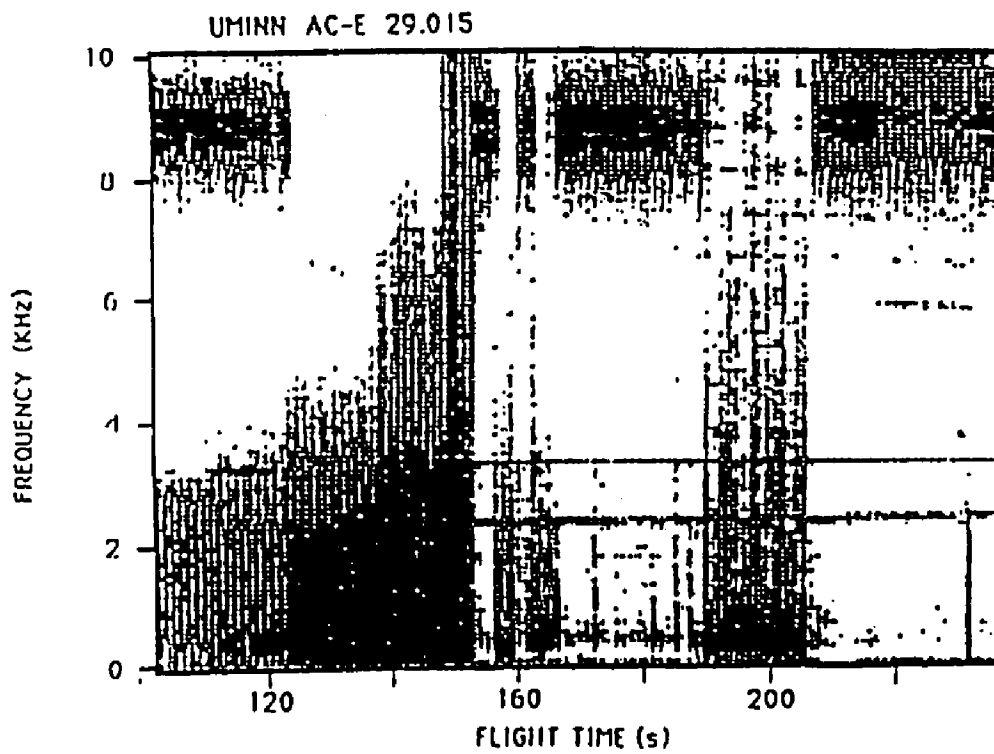


Fig. 8-1 Dynamic Spectrum of ACE Field, 110-220

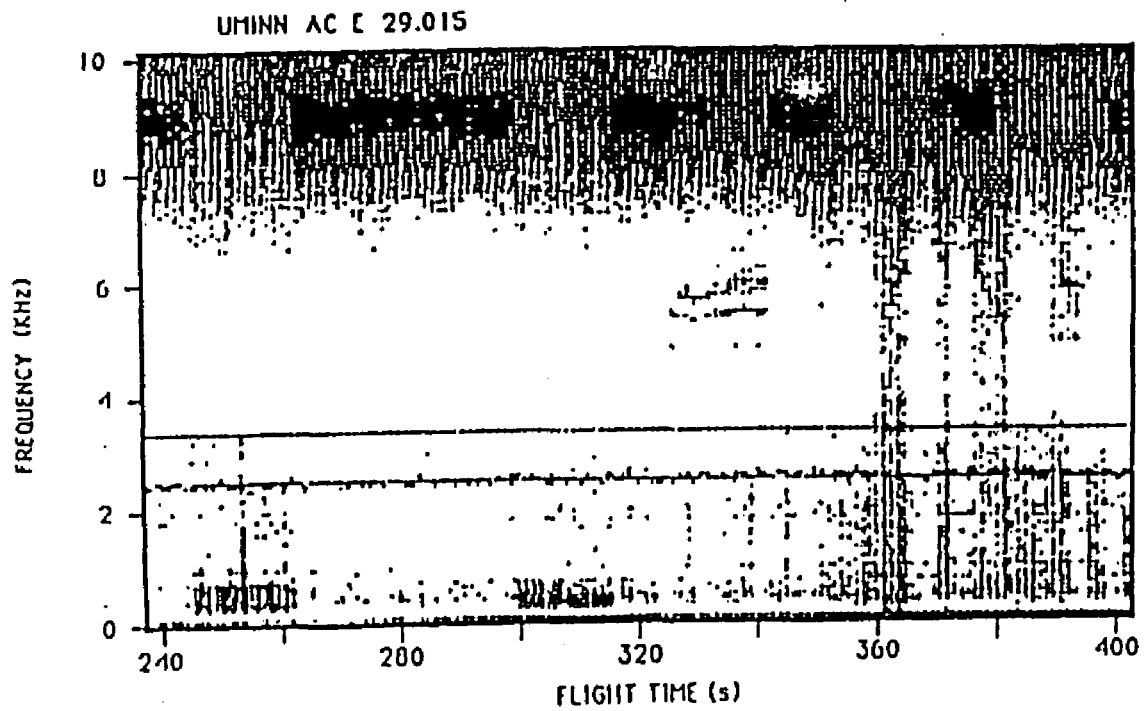


Fig. 8-2 Dynamic Spectrum of ACE Field, 240-400

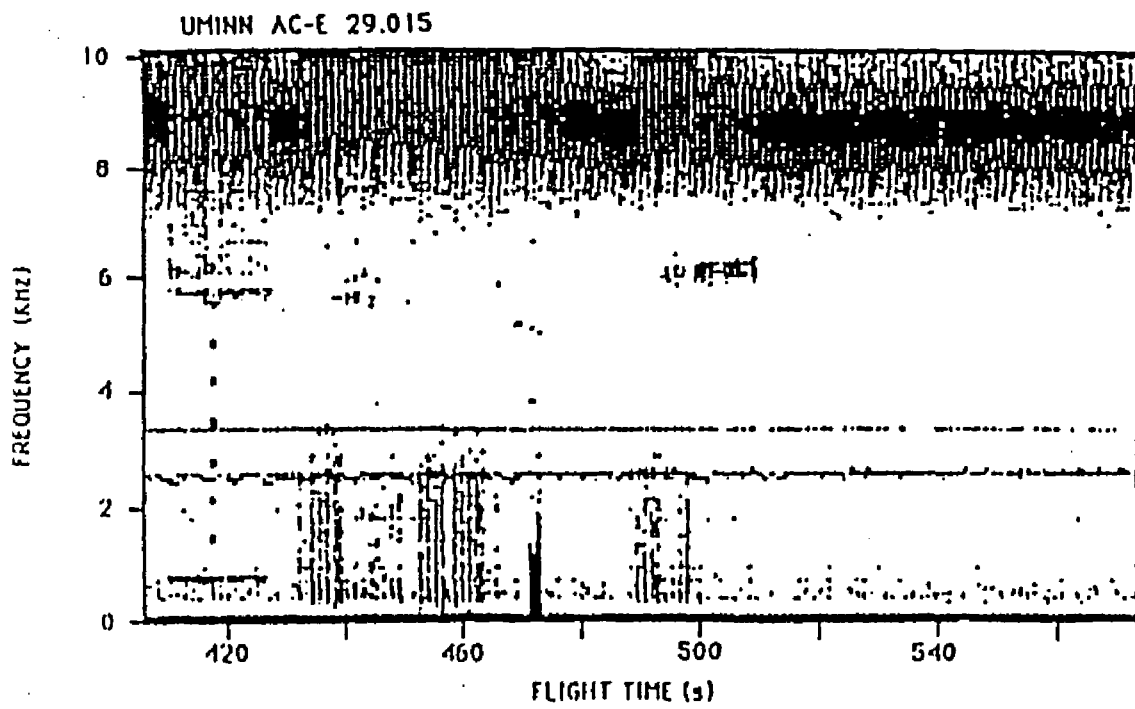


Fig. 8-3 Dynamic Spectrum of ACE Field, 410-550

Let's return to Fig. 4-1 again. Fig. 4-1b, the $2 \perp$ event, after the gun turned off, shows strong and narrow spectral peaks. Fig. 4-1c, the $3 \perp$ event, shows several very narrow spectral peaks near the 2nd to 12th harmonics of the O^+ cyclotron frequency. Fig. 4-1d, the $4 \perp$ event, shows several spectral peaks near the 2nd to 8th harmonics of the O^+ cyclotron frequency. Fig. 4-1b, 4-1c and 4-1d, show a common feature, which is that the strongest peaks are all near the 4th harmonic of the oxygen ($\sim 180\text{Hz}$). This observation is consistent with Fig. 8-5b. Erlandson *et al.* refer those peaks as the fundamental, fourth, fifth and eighth through thirteenth harmonics of the oxygen cyclotron frequency. Because there was no mass spectrometer on the rocket, they don't know exactly which ion species produced these harmonic frequencies. Actually, the H^+ , He^+ , O^+ , and even the argon ions all are possible sources of the spikes. From the Figure 4-1, we can see the spectral densities of the harmonics are from 2×10^{-3} to $8 \times 10^{-3} (mV/m)^2/Hz$.

8.2 Correlations of EIC Wave with Beams

What mechanism produced the spin modulated narrow lines about 180Hz and 130Hz? Were they associated with the argon ion beam? Since the wave pattern had an apparent modulation at the sub - payload spin frequency, we thought at first that the waves could be Electrostatic Ion Cyclotron Waves(EIC) of some species driven by the artificial argon beam. To verify this hypothesis, we checked the time correlations between the argon beam and the waves received by the ACE wave receiver.

First, we calculated the argon beam locations at several different times at which we see waves associated with the argon gun spinning by using the techniques we developed in Chapter 2 and Appendix c. Next we found the times at which the front edge or back edge passed the detector, and used the former time as the "ZERO" for the comparisons with the times at which waves were received. The statistical results are shown in Fig. 8-6.

The wide frequency bursts shown in Fig. 8-4a and 8-4b. appear mostly near the back edge of the artificial argon ion beam. The low frequency EIC waves seen during the $2 \perp$ event are different from those seen during the $4 \perp$ event. For the $2 \perp$ event, we can see that the beams reached the detector 40-60ms ahead of the wave. For the $4 \perp$ event, we find that the beam and waves exhibited a matching pattern, with the beam width being almost the same as the average width of the wave peaks($\sim 180ms$). We can conclude that the low frequency wave is driven by the argon beam.

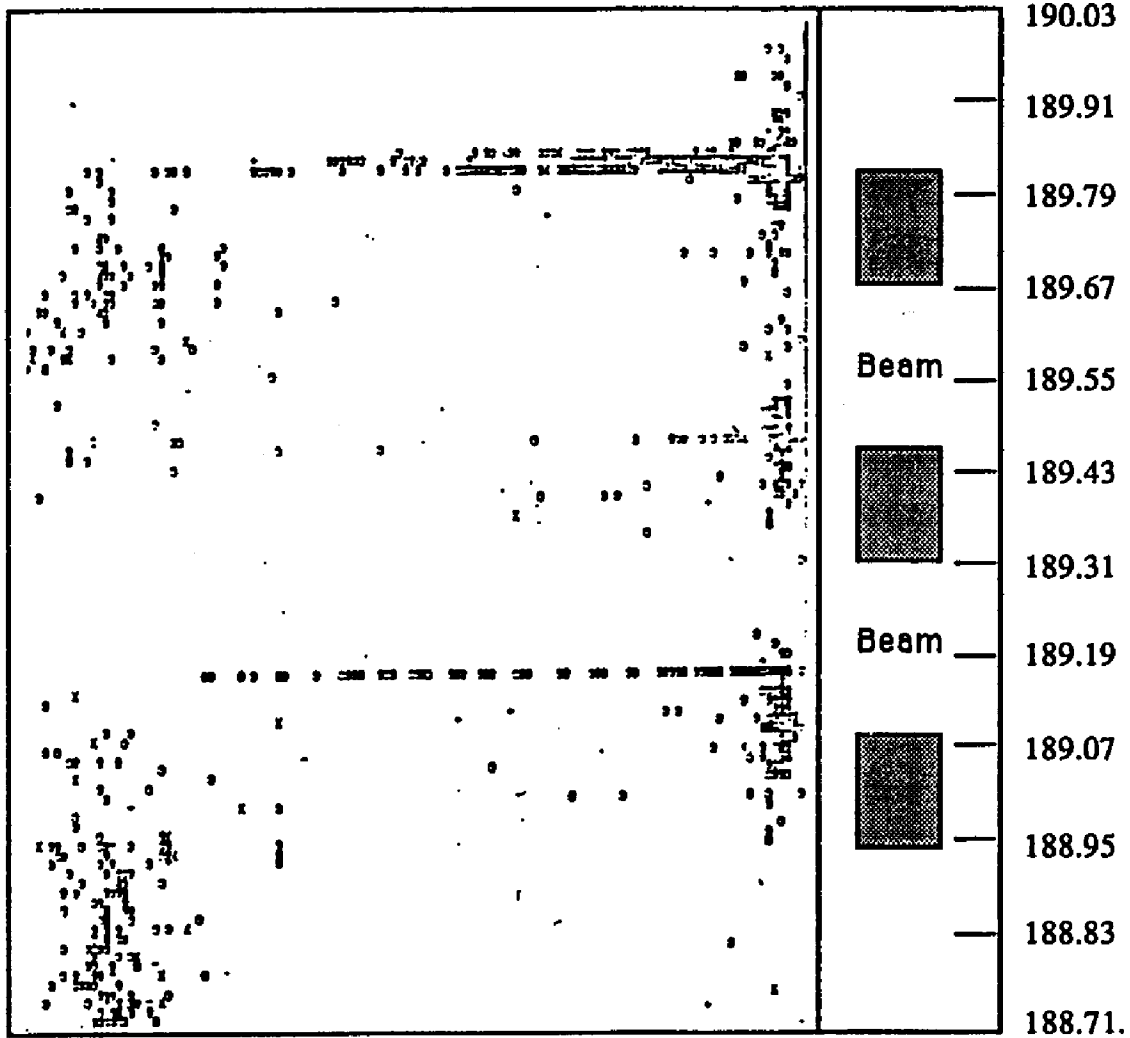


Fig. 8-4a Fourier Spectra of Wide Frequency Band
188.71 - 190.03s

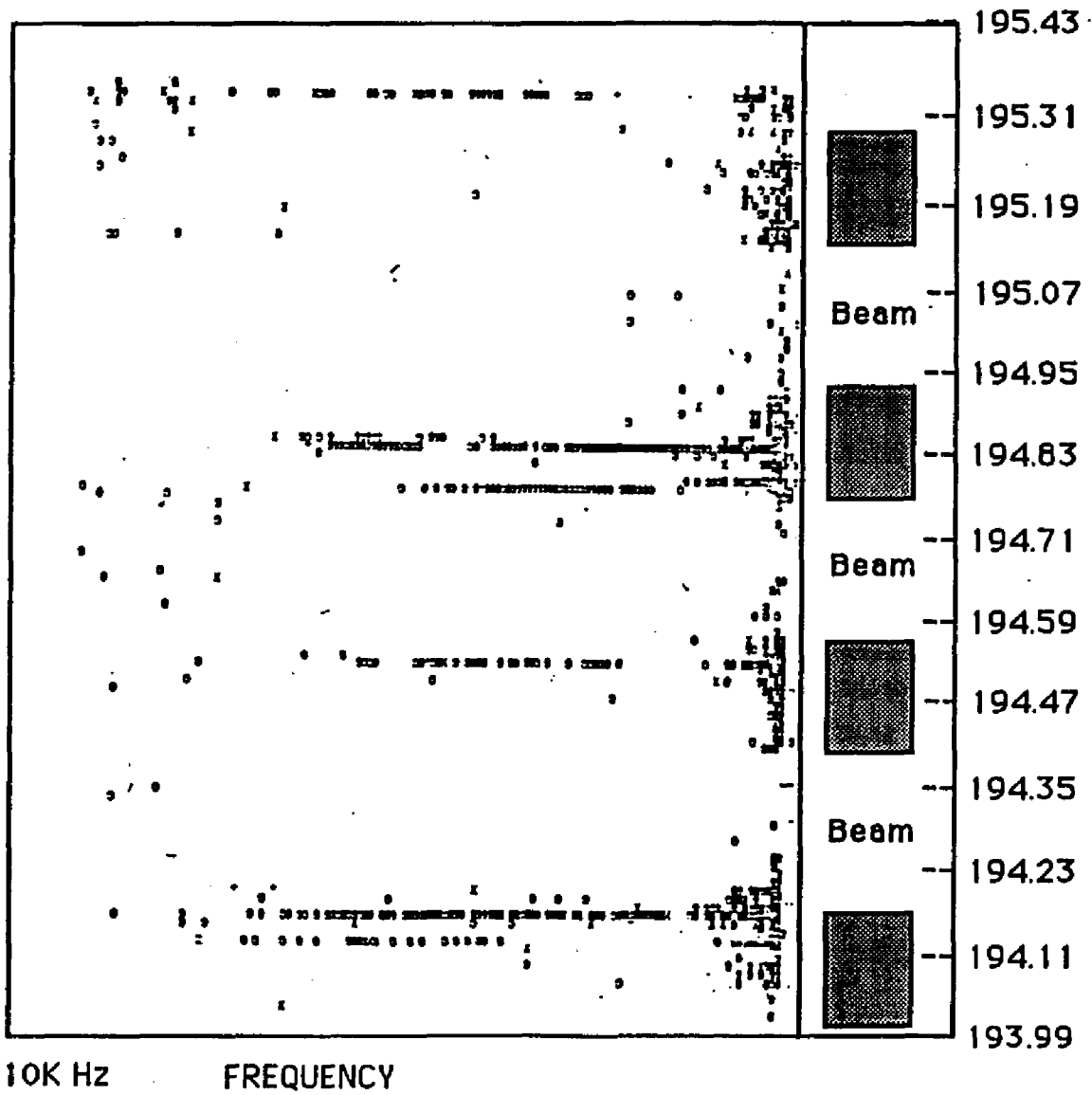


Fig. 8-4b Fourier Spectra of Wide Frequency Band
193.99 - 195.31s

64 frequencies
102.2 msec. window
20 msec. period

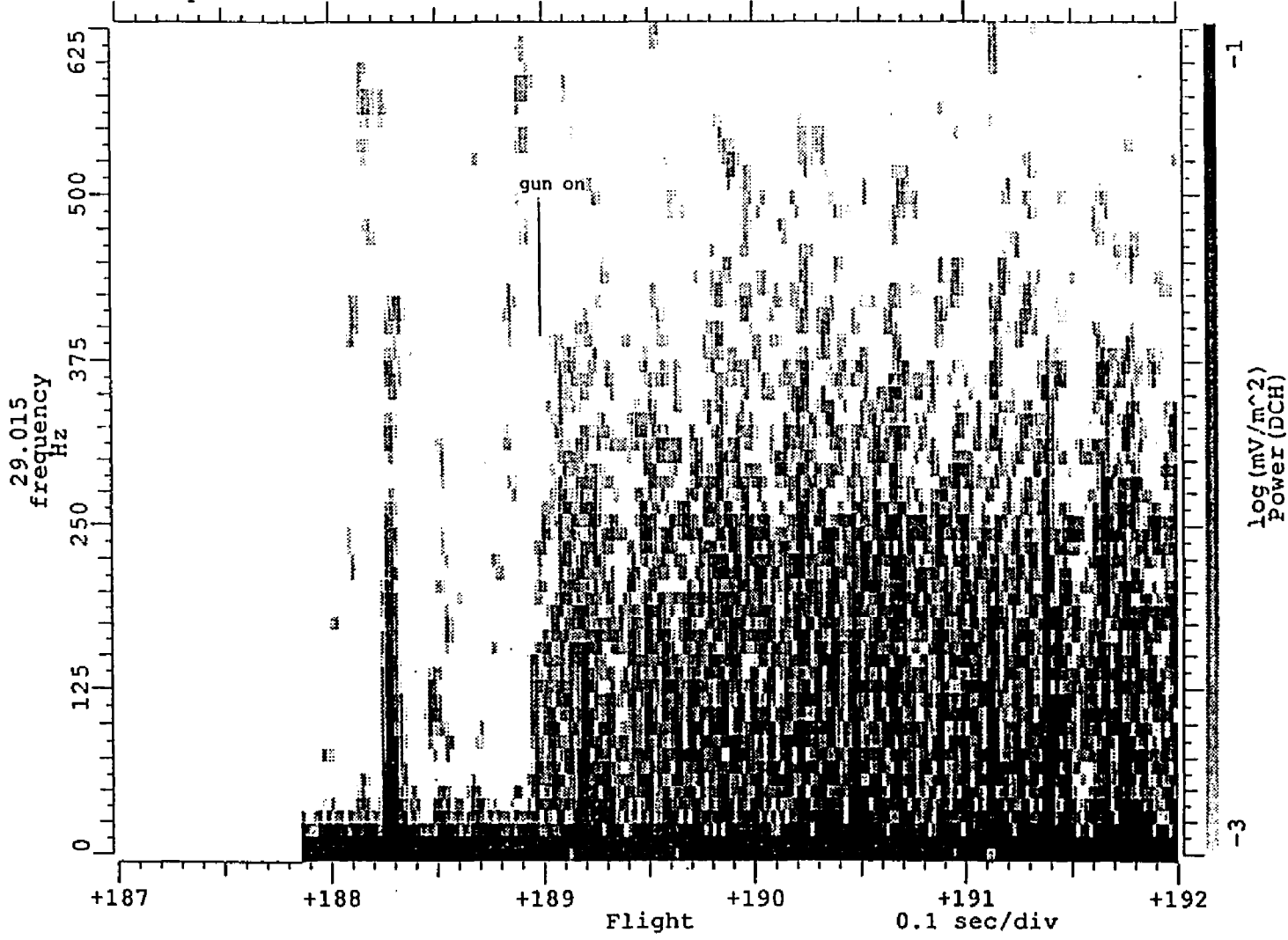
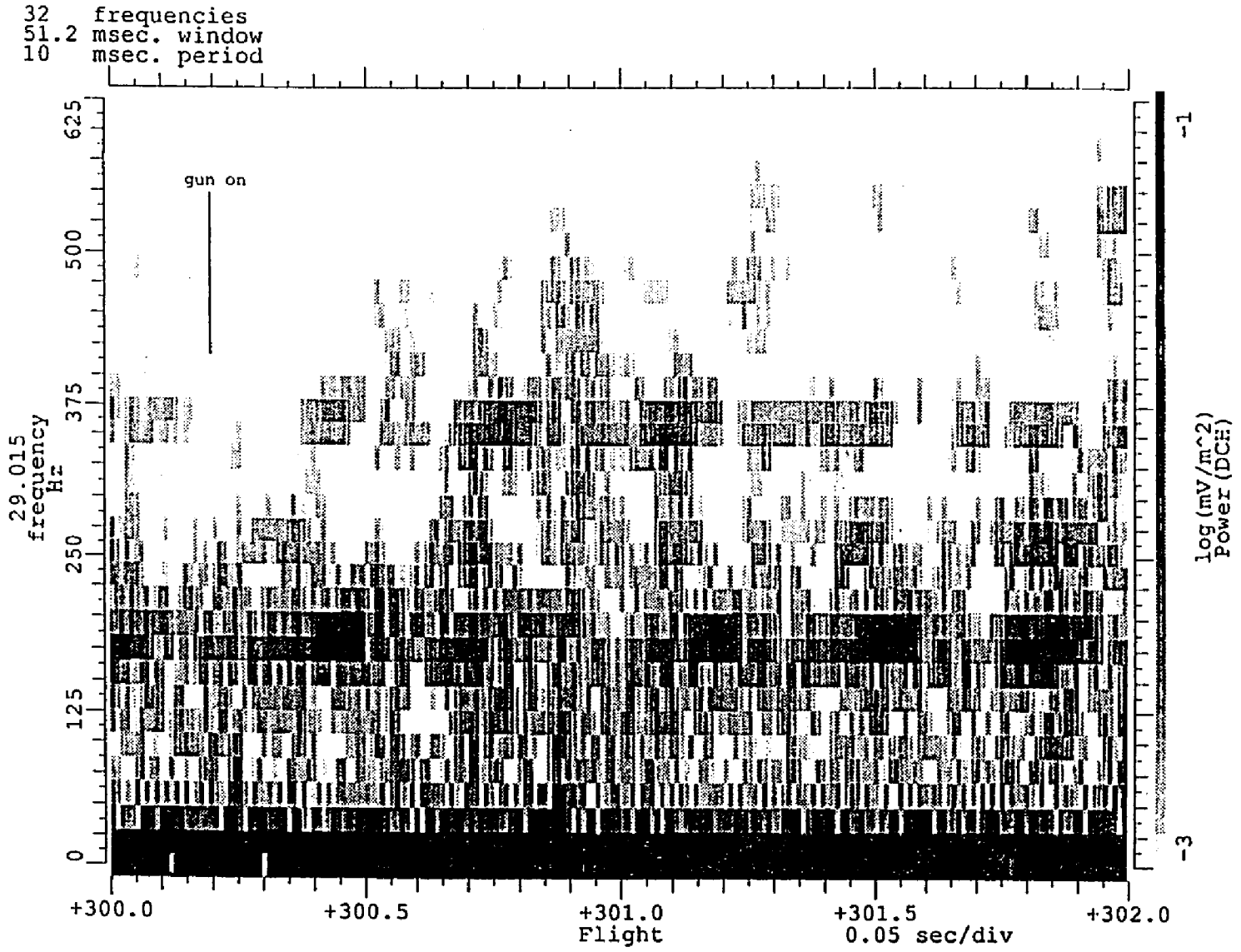


Fig. 8-5a Fourier Spectra of Low Freq. Band, 187.-192.s

Fig. 8-5b Fourier Spectra of Low Freq. Band, 300.-302.s



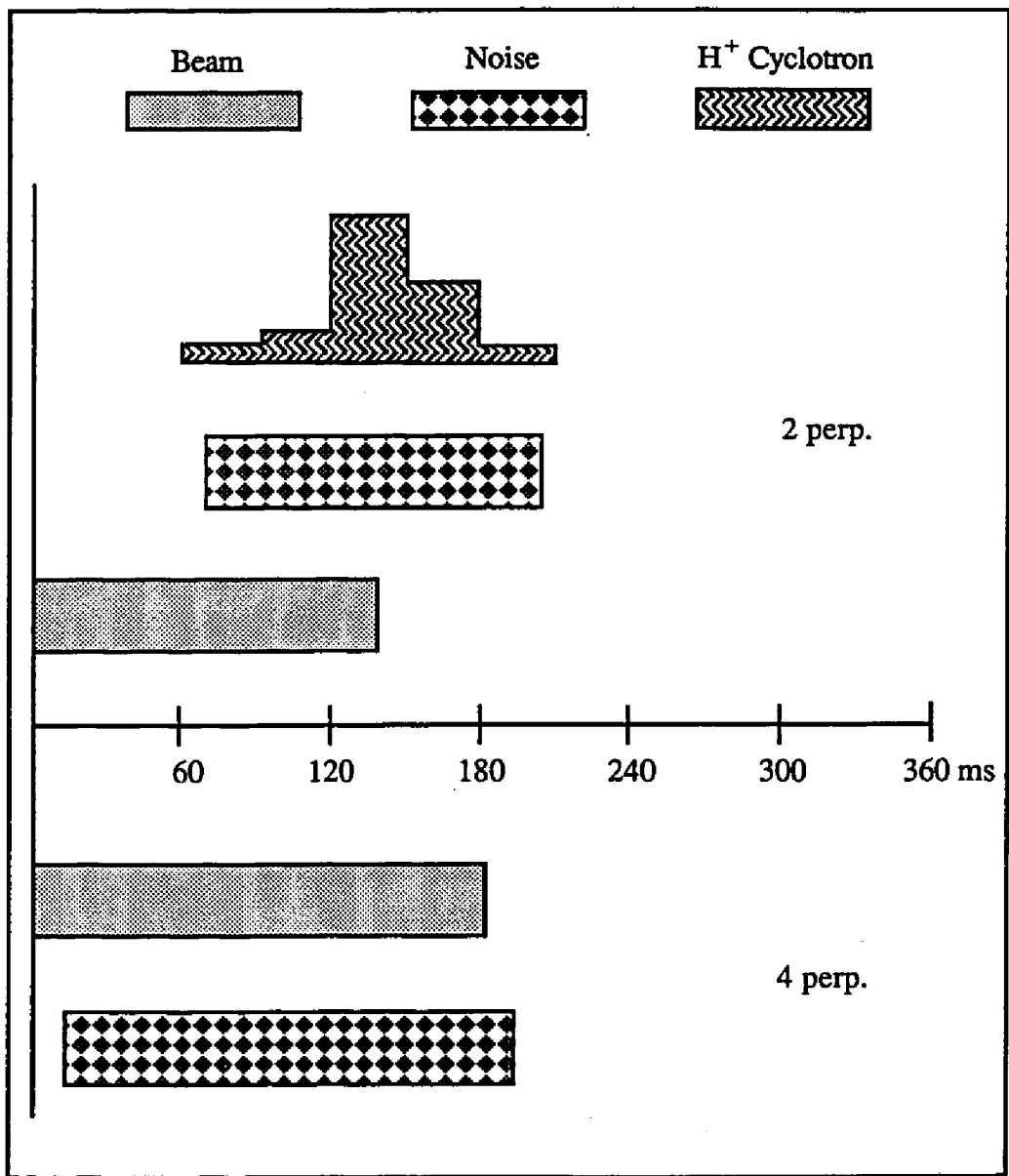


Fig. 8-6 Comparison of Low Frequency Noise, H⁺ Cyclotron Bursts and Beams. For 4th Perpendicular Event, H⁺ Cyclotron Bursts were not seen

Figure 8-7a, a special case, shows the noise received during the time period from 203s to 208s. We note that at 206.1 the $2 \perp$ ion gun firing had turned off, but from this figure we can see that the two low frequency waves still were present, one near 180Hz, one near 130Hz. We understand this as a time delay required for some gun particles to reach the vicinity of the main payload. This time delay can range from a few milliseconds to a few seconds, depending on the parallel velocities of the ions. If we assume that all particles have the same energy, then the time delay depends on the pitch angle of each individual particle. For example, a 100ev argon ion with 180 degree pitch angle, i.e. moving anti - parallel to the local magnetic field B , needs about 5ms to reach main payload during the $2 \perp$ gun firing. At this time, the main payload is separated by 110 to 150 meters from the sub - payload, on which the both argon guns were located. A 100ev argon ion with a 91 degree pitch angle needs $\approx 400ms$ to reach the main payload. Fig 8-7b shows the argon ion flux and density at two times (205.74s, 206.11s), before the $2 \perp$ ion gun was turned off, and at 206.42s and 206.78s, after the ion gun was turned off. We notice that the perpendicular gun was turned off at 206.10s. After 206.1s no more new argon ions came out of the gun. The argon flux dropped from 4×10^7 at 205.74s to 1×10^4 at 206.42s, by a factor of 1000, while the argon ion density dropped from 45 to 4, only a factor of 10. The reason for this was that the particles received a long time after the gun turned off all had high perpendicular velocity and low parallel velocity, or pitch angles that were very close to 90 degrees. They took a great number of gyro periods

before reaching the detector plane. Since

$$\rho = \frac{J}{v_{\parallel}}$$

the flux J passing the detector plane could be low, while the density ρ near the detector plane was not as low as may have been expected. The presence of a high density of argon ion around the main payload after the argon gun was turned off is the reason why we can receive low frequency waves ~ 1 second after the ion gun was turned off.

64 frequencies
102.2 msec. window
20 msec. period

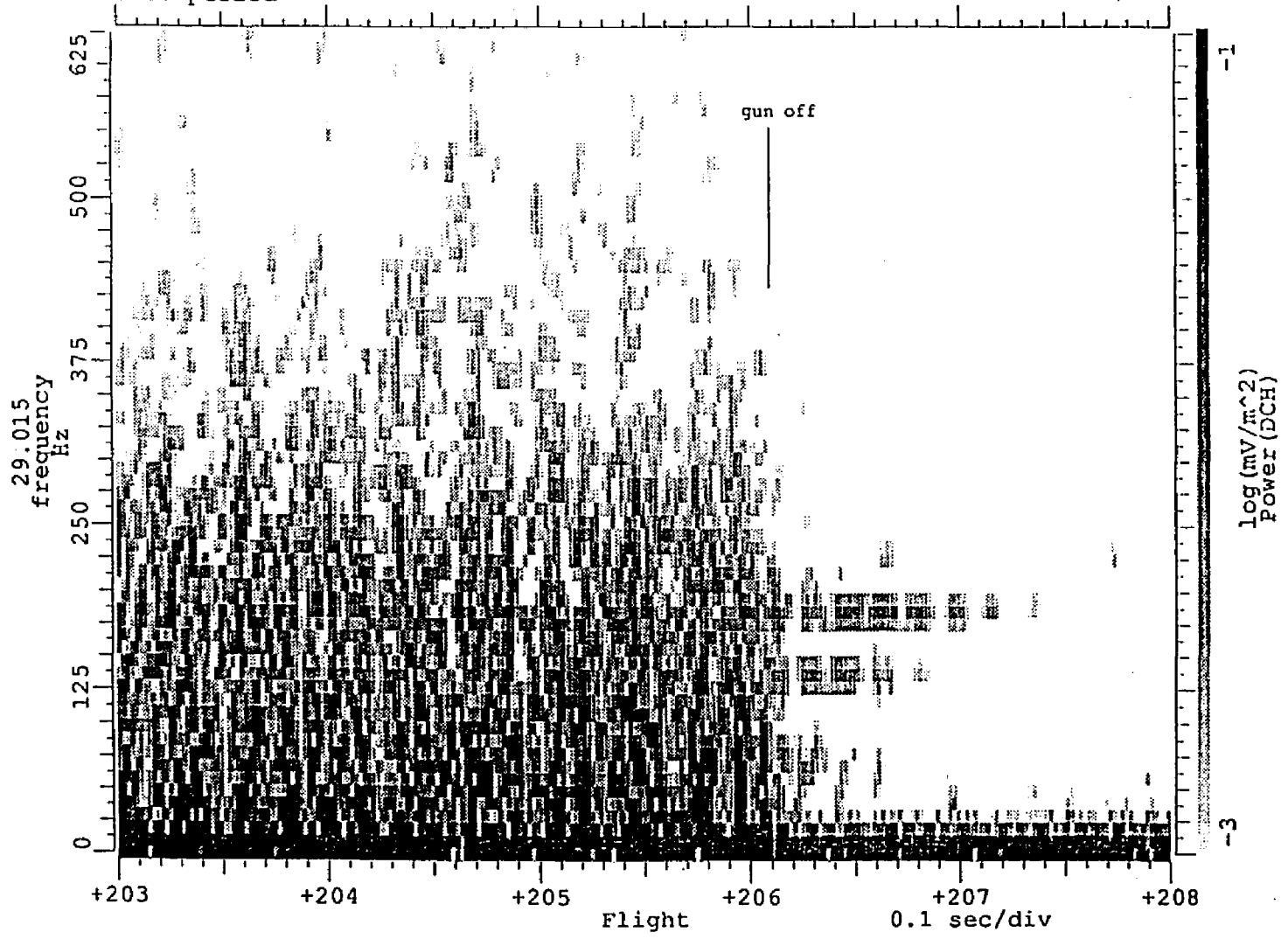
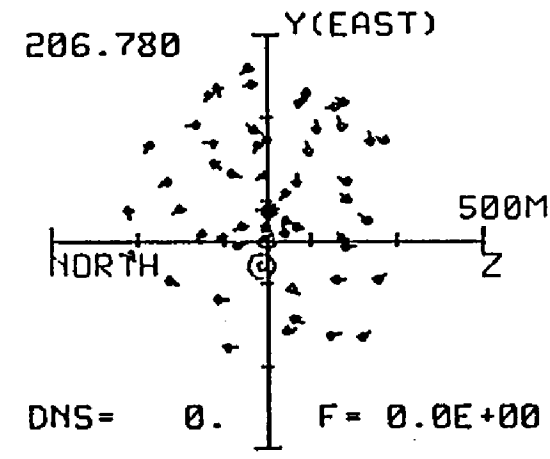
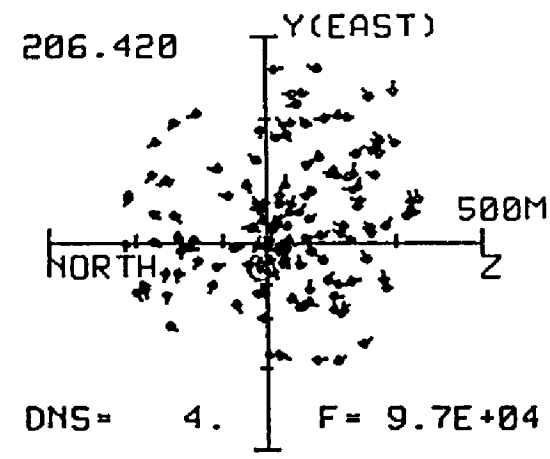
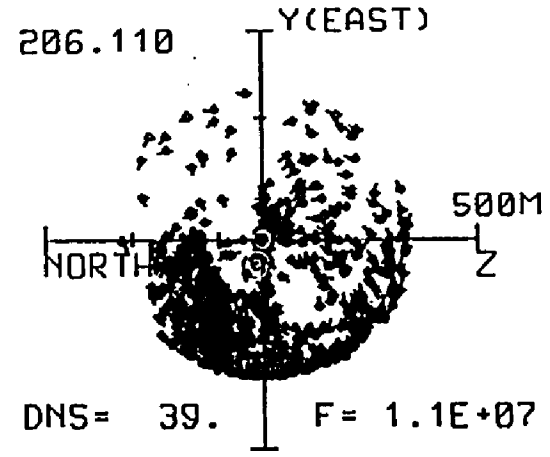
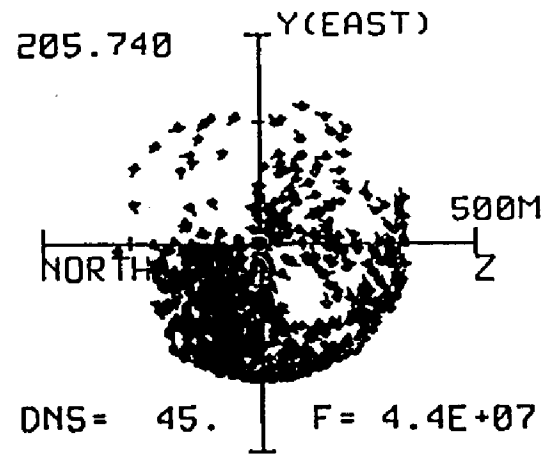


Fig. 8-7a Fourier Spectra of Low Freq. Band, 203-208s

Fig. 8-7b Beam Density and Flux, 205.74-206.78s



8.3 $O^+ - He^+$ Bi-hybrid Mode fluctuations

From Fig. 4-1b, 4-1c, 4-1d, we can see that many peaks appear in the power spectra. The strongest one appears near 190Hz. Kintner *et al.* [1986] refer to this peak as the 4th harmonic of oxygen. To verify this, we checked the frequencies of the possible wave modes with different densities of ionospheric He^+ . When the density of He^+ equals 1% of the ionospheric electron density, the frequency of a normal mode is 203 Hz. This frequency is very close to the 4th harmonic of O^+ (205Hz), and also very close to the bi-hybrid frequency of O^+ and He^+ (202Hz), as shown in Fig. 8-8a. Fig. 8-9a, 8-9b are similar to Fig. 7-3a,7-3b. The 4 numbers of the top line represent the hybrid frequencies for this plasma. The highest number is the upper hybrid frequency, the second highest is the lower hybrid frequency, the next is the bi-hybrid frequency of $O^+ - He^+$. The lowest one is the bi-hybrid frequency of $Ar^+ - He^+$, but is meaningless in this case, because we assumed Ar^+ is an unmagnetized species.

For a cold plasma in a magnetic field, if we consider waves which propagate perpendicular to the magnetic field, i.e. $k_{\parallel} = 0$, the dispersion relation reduces to

$$\sum_s \frac{\omega_{p,s}^2}{\omega^2 - \omega_{c,s}^2} = 1 \quad (8.1)$$

where $\omega_{p,s}$, $\omega_{c,s}$ are the plasma frequency and cyclotron frequency of the s species respectively [Hughes, 1975]. The summation is over all existing species. For our case it is 4 species. In general, Eq. (8.1) has 4 roots for a positive real frequency ω . The highest root of Eq. (8.1) is the upper hybrid frequency, the second highest is lower hybrid frequency. The other two are bi-hybrid frequencies. If a bi-hybrid frequency lies between the cyclotron

frequencies of species A and B, we call it the A-B bihybrid frequency. For example, the third highest frequency in Fig. 8-8a is between the cyclotron frequency of O^+ and the cyclotron frequency of He^+ , so we call it as the $O^+ - He^+$ Bihybrid frequency.

To check this identification, we raised the density of He^+ to 10% of the density of ionospheric electrons. From Fig. 8-8b, we can see that the frequency of the normal mode (181Hz) is far below the 4th harmonic of O^+ (205Hz). However, the frequency of this normal mode is still very close to the bihybrid frequency of $O^+ - He^+$ (179Hz). We conclude that the strongest peak in the power spectrum (Fig. 4-1) corresponds to the bihybrid wave of O^+ and He^+ .

LH= 1.3217E+02 1.2693E+03 3.5938E+04 1.3563E+07
 NAME DENS TPAR TPER WC LP THML STRM MX MG
 1 E- 3.0E+04 1.5E+03 1.5E+03 -9.41E+06 9.77E+06 2.13E+07 0.0E+00 4 Y
 4 HE+ 2.0E+02 1.5E+03 1.5E+03 1.29E+03 9.34E+03 2.50E+05 0.0E+00 99 Y
 2 O+ 2.0E+04 1.5E+03 1.5E+03 3.23E+02 4.65E+04 1.25E+05 0.0E+00 99 Y
 6 AR+ 1.0E+04 1.1E+05 1.1E+05 0.00E+00 2.09E+04 6.82E+05 2.2E+06 12 N

AZU= 20.0 PITU= 90.0 K:Uor= 2.1790E+03
 PICHK= 90.0 B0= 0.5348 K-1.054E-03 KPA=5.415E-07 KPE=-1.054E-03

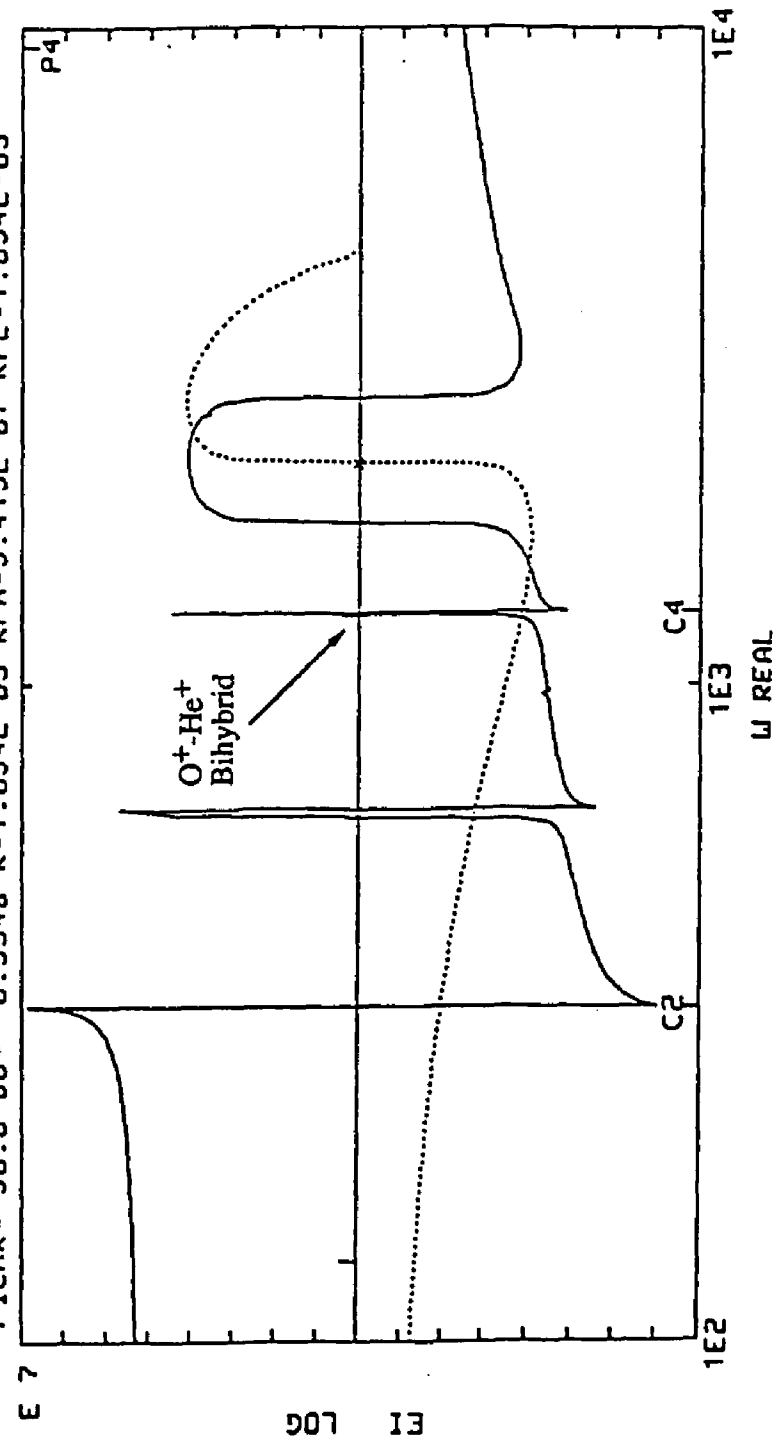


Fig. 8-8a Dielectric Function, 1%He+, O+ - He+ Bihybrid Mode

LH= 1.3140E+02 1.1247E+03 4.0796E+04 1.3563E+07
 NAME DENS TPAR TPER WC LP THML STRM MX MG
 1 E- 3.0E+04 1.5E+03 1.5E+03 -9.41E+06 9.77E+06 2.13E+07 0.0E+00 4 Y
 4 HE+ 2.0E+03 1.5E+03 1.5E+03 1.29E+03 2.95E+04 2.50E+05 0.0E+00 99 Y
 2 O+ 2.0E+04 1.5E+03 1.5E+03 3.23E+02 4.64E+04 1.25E+05 0.0E+00 2 Y
 6 AR+ 1.0E+04 1.1E+05 1.1E+05 0.00E+00 2.09E+04 6.82E+05 2.2E+06 12 N

AZU= 20.0 PITU= 90.0 K:Uor= 2.0673E+03
 PICHK= 89.9 B0= 0.5348 K=1.000E-03 KPA=1.000E-06 KPE=1.000E-03

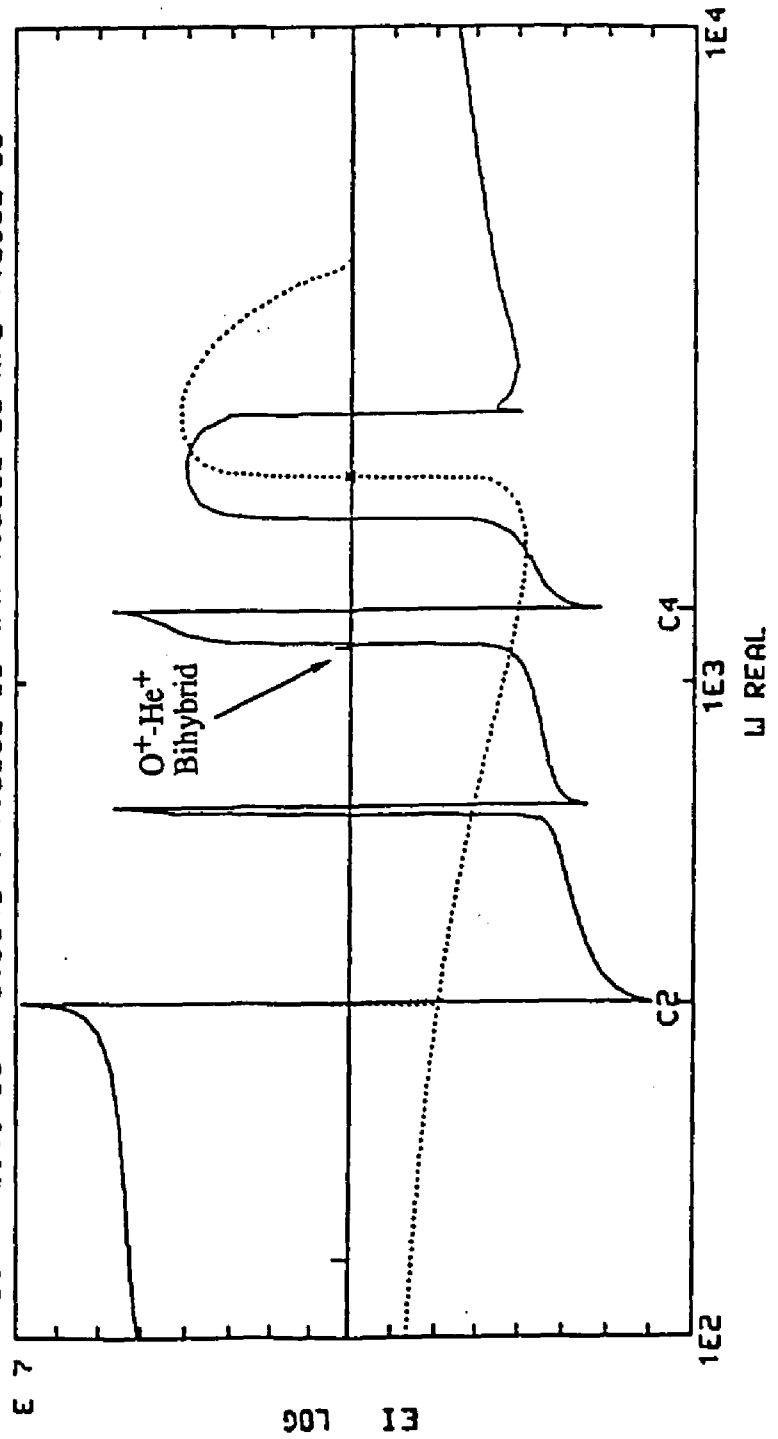


Fig. 8-8b Dielectric Function, 10%He+, O+ - He+ Bi-hybrid Mode

To further investigate the absolute power of the 4th peak (i.e. our $O^+ - He^+$ bihybrid wave), we have to do some quantitative calculations. Following the method we developed in chapter 7, we traced an isofrequency contour for the $O^+ - He^+$ bihybrid wave mode, as shown in Fig. 8-9. For k_{\perp} less than $6 \times 10^{-4}/\text{cm}$, the wave is stable or damped with a damping rate of 10 to 20/s. For k_{\perp} greater than $5 \times 10^{-3}/\text{cm}$, the wave is also stable or damped; the damping rate is around 5 to 10/s. In the intermediate part of the isofrequency contour, i.e. when k_{\perp} is greater than 6×10^{-4} and less than 5×10^{-3} , the wave is unstable.

The calculated growth rates are from 1×10^{-2} to 20/s. The lowest point on the contour ($k_{\perp} \sim 1 \times 10^{-3}$, $k_{\parallel} \sim 5 \times 10^{-7}$) has a growth rate of 7/s. This corresponds to a pitch angle of $\sim 90^\circ$. The calculated growth lengths along the isofrequency contour range from 1 meter to 20 meters. This length is 1/50 to 1/2 of the beam size, so it is very possible for the $O^+ - He^+$ bihybrid wave to grow to the observed noise level [$1 \times 10^{-2} (mV/m)^2$]. Incidentally, for the peak below the $O^+ - He^+$ bihybrid wave peak (near the 2nd harmonic of O^+), the slope of the ϵ_r is much steeper than the slope of ϵ_r for the 4th peak. As a result, the growth rate is much smaller (≤ 1). The growth lengths therefore are much longer ($\geq 100m$). This is the reason why the 4th peak is much higher than any other harmonic peak.

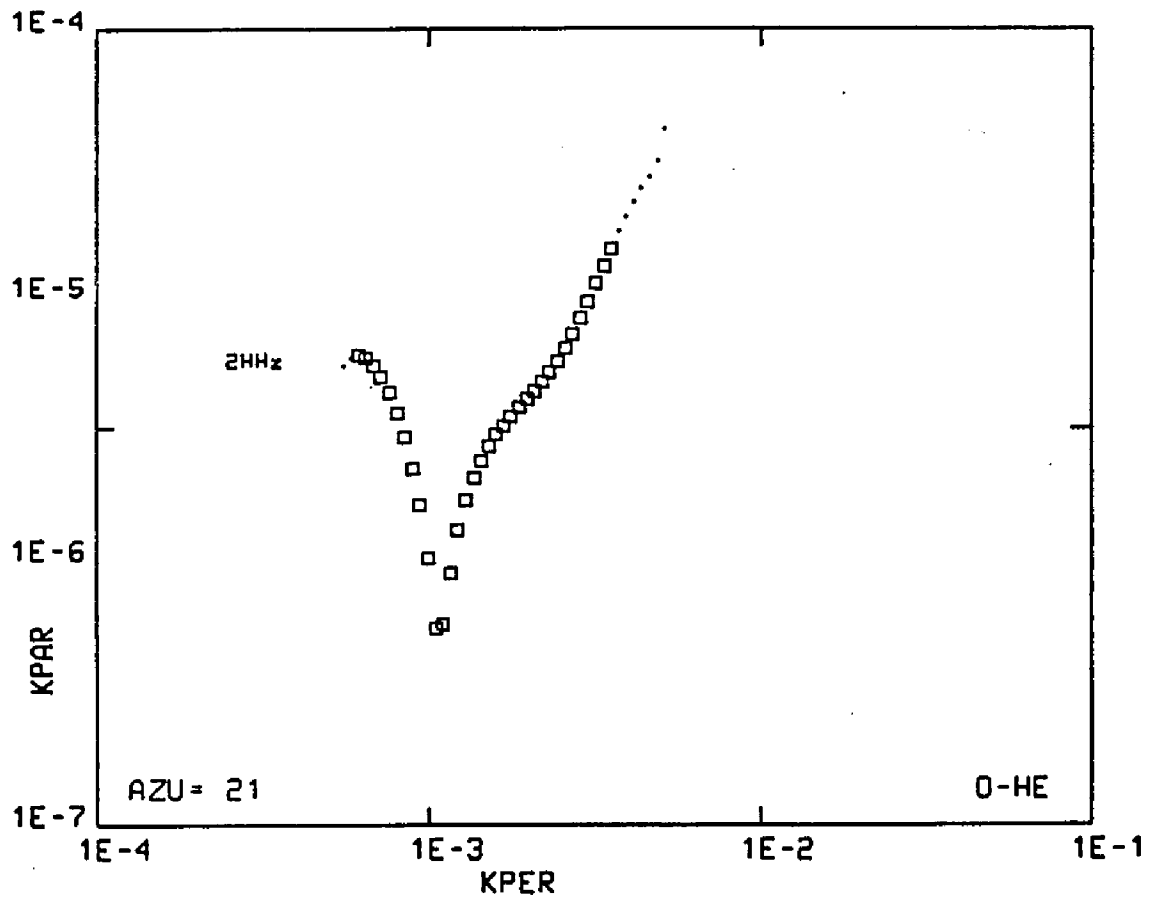


Fig. 8-9 Isofrequency Contour of $O^+ - He^+$ Biybrid Mode

Summary and Conclusions

1. The assumption that the 100ev argon ions followed single particle trajectories from the gun to the main payload matched well with observations made by the OCTO and HEEPS detectors.
2. Most of the broad band bursts appeared near the back edges of the argon beams.
3. After 206.1s, when the 2 \perp ion gun was turned off, a low frequency wave ($\sim 180\text{Hz}$) continued ~ 1 second. This wave was caused by the argon ions with pitch angles $\sim 90^\circ$ which were ejected before the gun was turned off.
4. According to our theory, the angle β between the $\mathbf{k} - \mathbf{B}$ plane and the streaming vector \mathbf{u} , or the factor $\mathbf{k} \cdot \mathbf{u}$, plays an important role in the stability of wave modes. For the O^+ -Acoustic wave, streaming in the same direction as the wave vector \mathbf{k} will drive an unstable wave most easily. As the angle β increases, the unstable region will shift towards larger pitch angles in \mathbf{k} space. When the angle β exceeds a certain limit, the unstable region will disappear. The angle β has a strong influence on the magnitude of steady state O^+ -Acoustic wave fluctuations. For $\beta = 0^\circ$, the wave amplitude is strongest. For $\beta = 180^\circ$, the wave amplitude is weakest.
5. In our calculations, we used a high density for the argon beam ($10^4/\text{cm}^3$) and a high electron temperature (4.5ev). Even for these plasma parameters, our results showed that the calculated plasma thermal fluctuation power spectral density is much lower than the observed background noise. We conclude that the observed background noise is not produced by plasma thermal fluctuations of O^+ -Acoustic waves driven

directly by the artificial argon beam.

6. There is a clear explanation for the harmonics seen on the power spectra of electric field fluctuations received by the DC electric field detector. Most waves are near cyclotron harmonics of O^+ . The 4th peak is the $O^+ - He^+$ bihybrid wave.
7. The comparison of the beam evolution patterns and the wave spectra shows that most noise during the 2 \perp gun operation appeared near trailing edge of the beam. The wave noise was more nearly collocated with the ion beam during the 4 \perp event. It therefore seems that the noise production mechanism was depends on distance from the gun. For the 1st event the electric field receiver was very close to the plasma gun, so the noise received could be produced mostly inside the gun. For the 4th event, the noise was directly associated with the argon beam. For the 2nd event, the noise was associated with the trailing edge of the argon beam.

Discussion

1. The kinetic theory of plasma fluctuations for a plasma with an unmagnetized two temperature component which is streaming in any direction is investigated for small amplitude fluctuations. A nonlinear fluctuation theory would be required to study large amplitude plasma waves. We only discussed fluctuations of the longitudinal waves, so in our calculations we used the longitudinal dielectric function $\epsilon(k, \omega)$. In general, if we consider electromagnetic fluctuations, we should use the dielectric tensor $\vec{\epsilon}(k, \omega)$ instead of the longitudinal dielectric function.
2. We haven't found what produced the low frequency background noise in Fig. 4-1. We have tried several different mechanisms, including the possibility that streaming of ionospheric electrons to neutralize the argon beam could produce the noise. The calculation shows that the density of the streaming electrons must be 100 times larger than is reasonable. The second possibility we have tried is that a 15ev O^+ or Ar^+ beam came from near the argon ion gun, in association with the 100ev argon beam, and produced the background noise. The calculations have told us that this is impossible. The last chance may be that the noise was produced just inside the argon gun chamber, and propagated to the wave receiver. This suggestion has nothing to do with the argon streaming in the ionosphere. The detailed calculations and discussions will be given in a separate paper.

Appendix A

TRANSFORMATIONS FROM ROCKET TO GM FRAME

A.1 Coordinate Systems

In this thesis, we use only right - hand coordinate systems, i.e.

$$\hat{x} \times \hat{y} = \hat{z}$$

$$\hat{y} \times \hat{z} = \hat{x}$$

$$\hat{z} \times \hat{x} = \hat{y}$$

where $\hat{x}, \hat{y}, \hat{z}$ are unit vectors along the X, Y, Z axes respectively. Under this rule, the rotation angles from $\hat{x} \rightarrow \hat{y}$ or from $\hat{y} \rightarrow \hat{z}$ or from $\hat{z} \rightarrow \hat{x}$ are defined positive, and the inverse rotation angles are negative.

The transformation matrix to rotate through an angle θ around the \hat{x} axis is

$$\begin{pmatrix} 1 & 0 & 0 \\ 0 & \cos \theta & \sin \theta \\ 0 & -\sin \theta & \cos \theta \end{pmatrix} \quad (A.1)$$

The transformation matrix to rotate through an angle θ around the \hat{y} axis is

$$\begin{pmatrix} \cos \theta & 0 & -\sin \theta \\ 0 & 1 & 0 \\ \sin \theta & 0 & \cos \theta \end{pmatrix} \quad (A.2)$$

The transformation matrix to rotate through an angle θ around the \hat{z} axis is

$$\begin{pmatrix} \cos \theta & \sin \theta & 0 \\ -\sin \theta & \cos \theta & 0 \\ 0 & 0 & 1 \end{pmatrix} \quad (A.3)$$

A.2 The Rocket Frame

This is the coordinate system moving and spinning with the rocket. Before the rocket was launched, the rocket hung on the launch rail. We define the direction perpendicular to the rocket body and pointing up to the launch hanger as the X axis. The direction in which the nose cone points is the Z axis, and the Y axis is defined by the right - hand rule, i.e.

$$\hat{y} = \hat{z} \times \hat{x}$$

as shown in figure A-1.

A.3 The Local Geographic Frame(LGG)

This coordinate system is defined as a system moving with the rocket. The geographic north direction is defined as the Z axis, the upward vertical direction as the X axis, and of course, the Y axis always points to the local geographic east, see figure A-2.

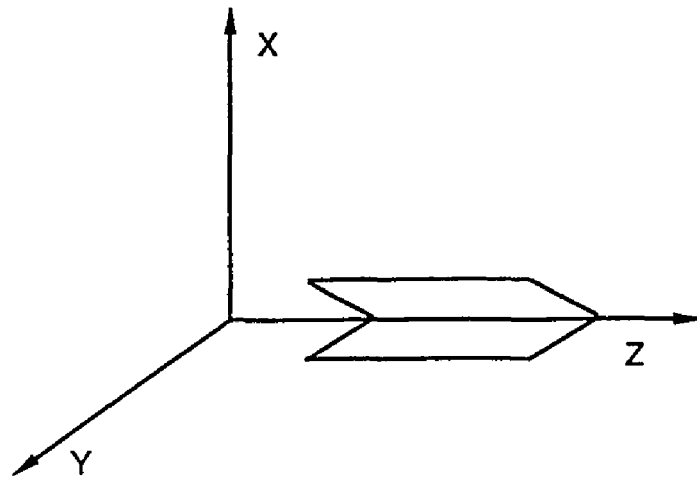


Fig. A-1 The Rocket Frame

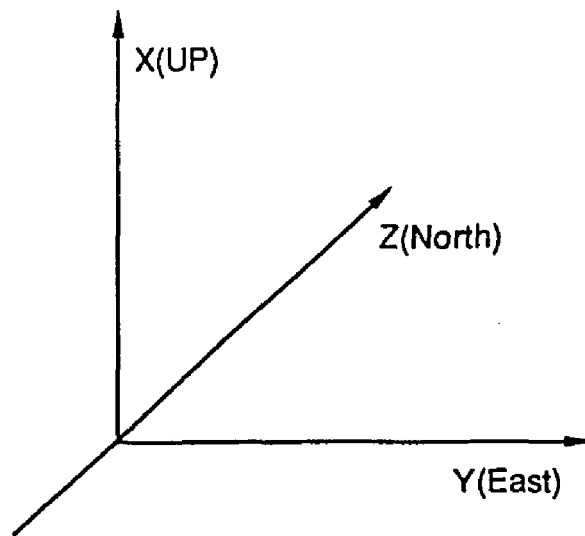


Fig. A-2 The Local Geographic Frame

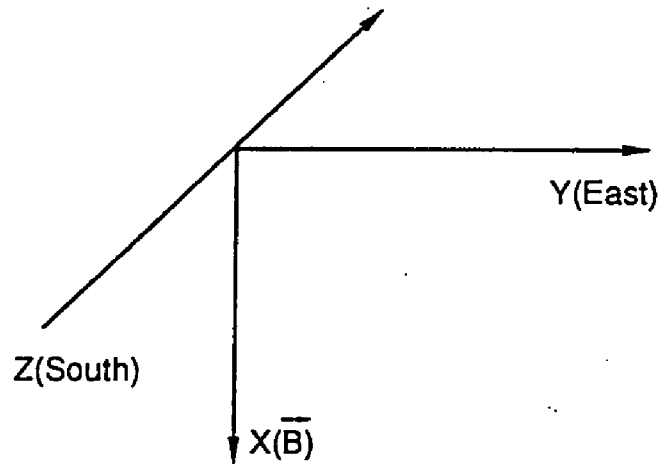


Fig. A-3 The Local Geomagnetic Frame

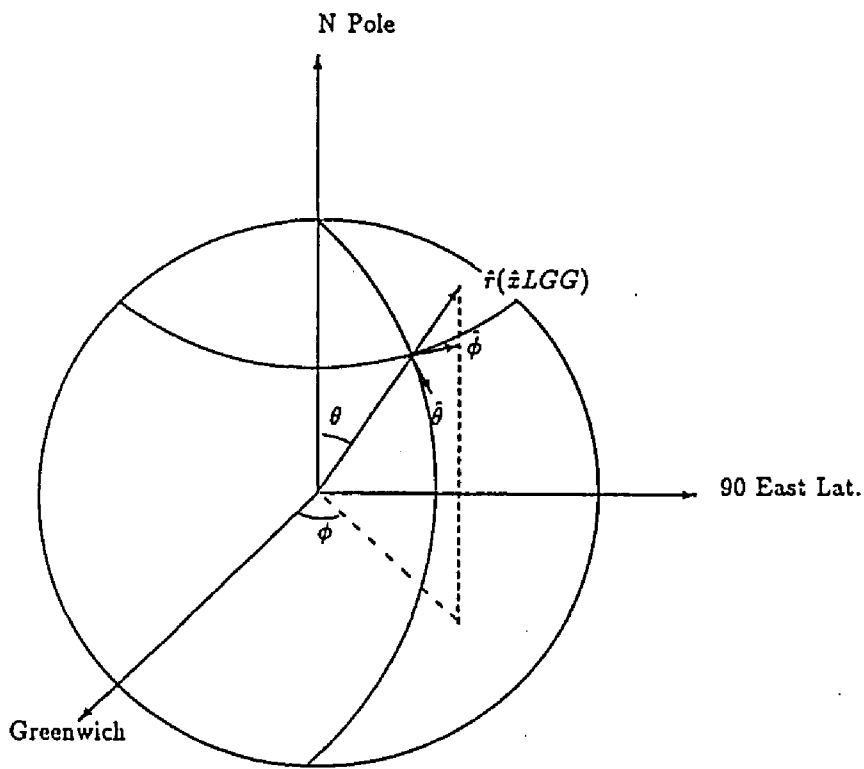


Fig. A-4 Global Geographic System

A.4 The Local Geomagnetic Frame(LGM)

In this coordinate system, the direction of the local magnetic field \mathbf{B} is defined as the X axis. The direction of local geomagnetic east is the Y axis, and the direction of the local geomagnetic south is the Z axis. Actually the LGM system can be obtained by rotating the LGG X axis(up), around the LGG east direction, until it points along the local magnetic field \mathbf{B} (down). Then the rotated LGG Z axis becomes the LGM Z axis, and the Y axis doesn't change. See figure A-3.

A.5 Transformations Between Frames

We now can find the quantitative relationships between the LGG frame and the LGM frame. The Rocket R29015 flight took place at a latitude $\sim 67^\circ N$, and a longitude $\sim 51^\circ W$. At an altitude of 300 kilometers, the local magnetic field was measured by the MagSat satellite[C. Pollock, Ph.D. thesis], as

$$\mathbf{B} = -0.5271\hat{r} - 0.0691\hat{\theta} - 0.0582\hat{\phi} \quad (A.4)$$

The field magnitude $B = 0.5348 \text{ Gauss}$, where the \hat{r} , $\hat{\theta}$, $\hat{\phi}$ are the three unit vectors of the Global Geographic System at SondreStrom Fjord, shown in Fig. A-4. From Fig. A-4 and the definitions of the LGG system, we can see the relationship between the unit vectors in the Global Geographic System (GGG) and the LGG system:

$$\hat{r} = \hat{x}(LGG)$$

$$\hat{\theta} = -\hat{z}(LGG)$$

$$\hat{\phi} = \hat{y}(LGG)$$

According to the above information, we can determine the direction angles of the magnetic field \mathbf{B} in the LGG system (see Fig. A-5).

Where $\hat{\theta}$, $\hat{\phi}$ are the unit vectors of GGG system, $\hat{x}, \hat{y}, \hat{z}$ are the unit vectors of LGG system, ψ is the angle between local zenith and the local magnetic field \mathbf{B} , δ is the angle from LGG North to the projection of \mathbf{B} on the local horizontal plane. From equation A.4,

$$\mathbf{B} \cdot \hat{r} = -0.5271$$

or

$$B \cos \psi = -0.5271$$

Solving this equation, we have

$$\psi = 170.2741^\circ$$

and

$$\tan \delta = \frac{-B_\phi}{-B_\theta} = \frac{0.0582}{0.0691}$$

as shown in Fig. A-6. We have

$$\delta = 40.1^\circ$$

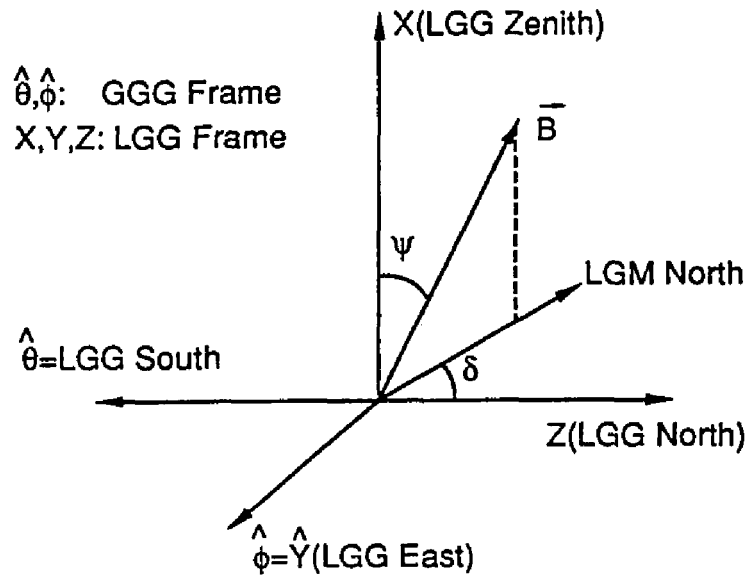


Fig. A-5 B field in the LGG Frame .

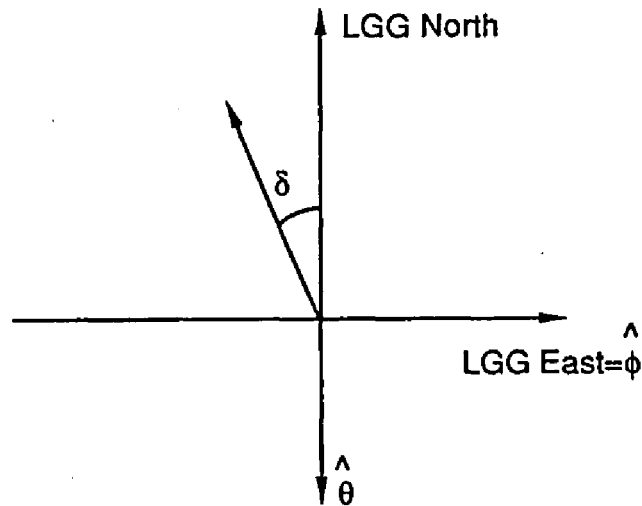


Fig. A-6 Projection of B on the LGG Horizontal Plane

We now have found the complete transformation procedure from the Rocket System to the Local Geomagnetic System:

If we know the roll angle α , pitch angle β , and the elevation angle γ of the rocket nose, the procedure to transform the rocket system to LGG system is:

Stage I, transform from the Rocket frame to the LGG frame:

1. First, roll an angle $-\alpha$ around the Z axis (rocket nose) until the X axis points up,.
2. then turn an angle $-\beta$ around the new Y axis to let the current Z axis lie on the horizontal plane.
3. then rotate through another angle $-\gamma$ around the current X axis until the current Z axis points to LGG north;

Stage II, transform from the LGG frame to the LGM frame:

4. First, turn an angle $\delta = 40.1^\circ$ around the current X axis until the current Z axis points to local geomagnetic north – the direction to which a compass will point.
5. the last step of the transformation is to turn through an angle of $-\psi = -170.27^\circ$ around the current Y axis to let the current X axis point to the local magnetic field's direction(**B**). Now the transformations are completed. Note the sign of the angle δ is positive. The matrixes of the transformations are:

$$\mathfrak{R} = \mathfrak{R}_5 \mathfrak{R}_4 \mathfrak{R}_3 \mathfrak{R}_2 \mathfrak{R}_1 \quad (A.5)$$

According to appendix A.1, where

$$\mathfrak{R}_1 = \begin{pmatrix} \cos \alpha & -\sin \alpha & 0 \\ \sin \alpha & \cos \alpha & 0 \\ 0 & 0 & 1 \end{pmatrix} \quad (A.6)$$

and

$$\mathfrak{R}_2 = \begin{pmatrix} \cos \beta & 0 & \sin \beta \\ 0 & 1 & 0 \\ -\sin \beta & 0 & \cos \beta \end{pmatrix} \quad (A.7)$$

and

$$\mathfrak{R}_3 = \begin{pmatrix} 1 & 0 & 0 \\ 0 & \cos \gamma & -\sin \gamma \\ 0 & \sin \gamma & \cos \gamma \end{pmatrix} \quad (A.8)$$

and

$$\mathfrak{R}_4 = \begin{pmatrix} 1 & 0 & 0 \\ 0 & \cos \delta & \sin \delta \\ 0 & -\sin \delta & \cos \delta \end{pmatrix} \quad (A.9)$$

and

$$\mathfrak{R}_5 = \begin{pmatrix} \cos \psi & 0 & \sin \psi \\ 0 & 1 & 0 \\ -\sin \psi & 0 & \cos \psi \end{pmatrix} \quad (A.10)$$

So if the coordinates of a vector in the rocket system are R_x, R_y, R_z then the coordinates of the vector in the LGM system will be

$$\begin{pmatrix} M_x \\ M_y \\ M_z \end{pmatrix} = \mathfrak{R} \begin{pmatrix} R_x \\ R_y \\ R_z \end{pmatrix} \quad (A.9)$$

Appendix B

SINGLE PARTICLE TRAJECTORIES

B.1 Plasma Diamagnetism

A particle with positive charge in a magnetic field \mathbf{B} experiences a Lorentz Force

$$\mathbf{F} = q\mathbf{v} \times \mathbf{B}$$

This force produces a centripetal acceleration, as shown in Fig. B-1. The centripetal force on a particle with negative charge will be in the opposite direction. In general the particle gyromotion is always in a direction, so that the electric current generated by the moving particle with either charge generates a perturbation magnetic field directed opposite to magnetic field \mathbf{B} . Plasma diamagnetism can help us to determine the initial velocity, initial phase of the particles in a magnetic field.

B.2 Single Ion Trajectory

In the geomagnetic coordinate system, an ion has an initial position x_0, y_0, z_0 and an initial velocity which is described by the initial speed v , initial pitch angle θ and initial azimuthal angle ϕ . Note that in my definition of the local geomagnetic system, the azimuthal angle is measured

from LGM north and increases towards the west. This is opposite to the definition of the azimuthal angle in the LGG system. The reason for this choice is that the local \mathbf{B} direction is almost opposite to the local radial direction. By using the diamagnetism rule [Appendix B.1], we can draw the trajectory of an ion in the LGM system.

In Fig. B-2, the local magnetic field \mathbf{B} points downward into the paper. The initial velocities are:

$$v_{x0} = v_{\parallel}$$

$$v_{y0} = v_{\perp} \sin \phi$$

$$v_{z0} = v_{\perp} \cos \phi$$

where $\phi = Azm - \pi$, and Azm is the azimuthal angle of the particle. If we also consider the $\mathbf{E} \times \mathbf{B}$ drift, the velocities of the ion can be written as

$$\mathbf{v} = v_{\parallel} + \mathbf{v}_{\mathbf{v} \times \mathbf{B}} + \mathbf{v}_{\mathbf{E} \times \mathbf{B}} \quad (B.1)$$

where we assume $\mathbf{E}_{\parallel} = 0$. But

$$\mathbf{v}_{\mathbf{v} \times \mathbf{B}} = v_{\perp} [\sin(\phi + \omega t) \hat{y} + \cos(\phi + \omega t) \hat{z}] \quad (B.2)$$

$$\mathbf{v}_{\mathbf{E} \times \mathbf{B}} = \frac{10}{B_G} [E_x \hat{y} - E_y \hat{z}] \quad (B.3)$$

Combining Eq. (B.1), (B.2) and (B.3), we have

$$v_x = v_{\parallel} \quad (B.4a)$$

$$v_y = v_{\perp} \sin(\omega t + \phi) + \frac{10}{B_G} E_x \quad (B.4b)$$

$$v_z = v_{\perp} \cos(\omega t + \phi) - \frac{10}{B_G} E_y \quad (B.4c)$$

Where B_G is the magnitude of the local magnetic field in Gauss, and E_y, E_z are two components of the electric field in units of mV/m. The position of an ion at any given time t is

$$x = x_0 + \int_0^t v_x(t') dt' = x_0 + v_{\parallel} t \quad (B.5a)$$

$$y = y_0 + \int_0^t v_y(t') dt' = y_0 - R_L [\cos(\omega t + \phi) - \cos \phi] + \frac{10E_z}{B_G} t \quad (B.5b)$$

$$z = z_0 + \int_0^t v_z(t') dt' = z_0 + R_L [\sin(\omega t + \phi) - \sin \phi] - \frac{10E_y}{B_G} t \quad (B.5c)$$

Where $R_L = v_{\perp}/\omega$ is the gyroradius of the ion in a magnetic field. Similarly, the positions of the guiding center of the ion are:

$$x_c = x_{c0} + v_{\parallel} t$$

$$y_c = y_{c0} + \frac{10E_z}{B_G} t$$

$$z_c = z_{c0} - \frac{10E_y}{B_G} t$$

where $x_{c0}, y_{c0} = R_L \cos \phi$, $z_{c0} = -R_L \sin \phi$ are the x, y and z components of the initial positions of the guiding center.

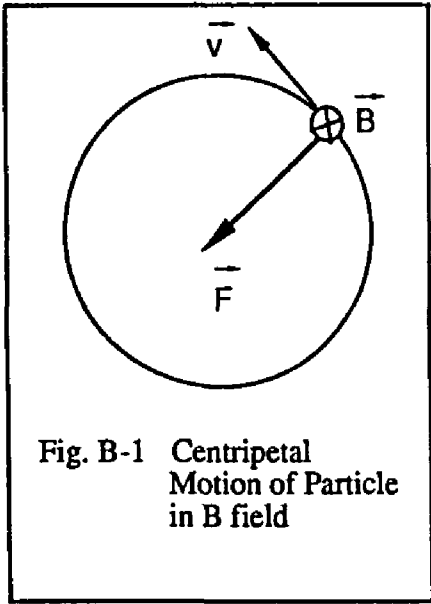


Fig. B-1 Centripetal Motion of Particle in B field

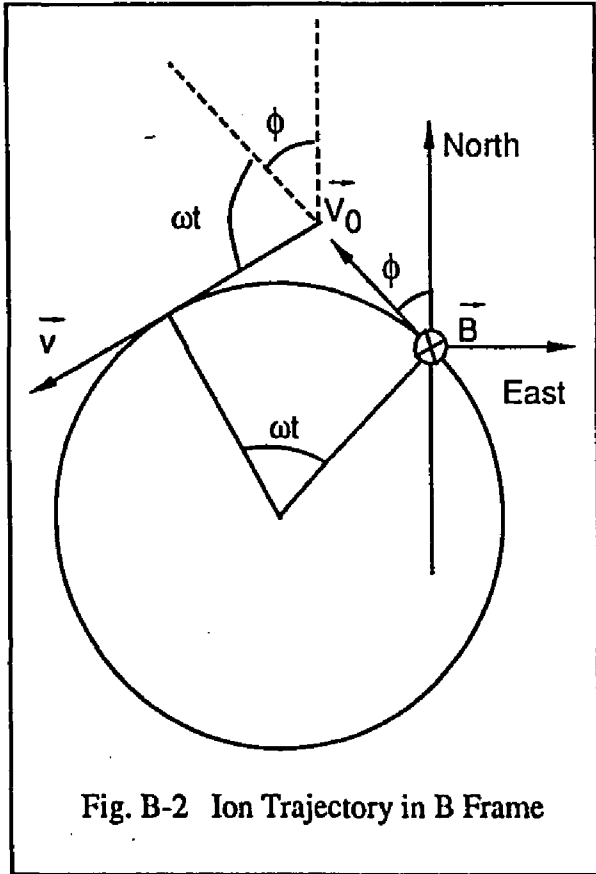


Fig. B-2 Ion Trajectory in B Frame

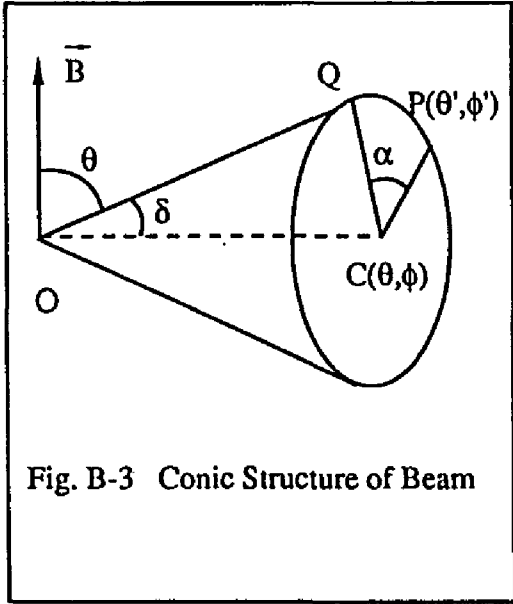


Fig. B-3 Conic Structure of Beam

B.3 Conic Structure of the Beam

In the last section, we have found expressions for the position of a single ion at any given time, given the initial position and the initial velocity. Ions are emitted from the gun with a range of velocities. We know the gun's direction, which also is the direction of the ion beam center line. Measurements in the laboratory [Pollock, 1987] tell us that particles ejected from the gun fill a cone with half angle of about 30 degrees. It is useful to find an expression for the angular direction of an arbitrary ion with respect to the angular direction of the beam's centerline. The cone centerline OC has pitch and azimuthal angles θ , ϕ . An ion moving in the direction OP deviates by an angle δ from the centerline and by an angle α from the line CQ. The line CQ is the intersection of the cone bottom plane and the plane that passes through both the line OC and the magnetic field B. If we call the pitch and azimuthal angles of the ion θ' , ϕ' [see Fig. B-3]; then, we can find the relation between θ' , ϕ' , and θ , ϕ :

$$\cos \theta' = \cos \delta \cos \theta + \sin \delta \cos \alpha \sin \theta \quad (B.6a)$$

$$\sin \theta' = +\sqrt{1 - \cos^2 \theta'} \quad (B.6b)$$

$$\cos \phi' = \frac{\cos \delta \sin \theta \cos \phi - AA \sin \delta}{\sin \theta'} \quad (B.6c)$$

$$\sin \phi' = \frac{\cos \delta \sin \theta \sin \phi - BB \sin \delta}{\sin \theta'} \quad (B.6d)$$

where

$$AA = \cos \alpha \cos \theta \cos \phi + \sin \alpha \sin \phi \quad (B.6e)$$

$$BB = \cos \alpha \cos \theta \sin \phi - \sin \alpha \cos \phi \quad (B.6f)$$

We can easily check Eq. (B-6a) to Eq. (B-6f) by looking at two special cases: First we set the angle $\alpha = 0$. Then the line OP becomes the line OQ. The pitch angle θ' should reduce to $\theta - \delta$ and the azimuthal angle should remain the same, i.e. $\phi' = \phi$. On the other hand, using

$$\alpha = 0, \text{ i.e. } \sin \alpha = 0, \quad \cos \alpha = 1$$

in Eq. (B.6a), we get

$$\cos \theta' = \cos \delta \cos \theta + \sin \delta \sin \theta = \cos(\theta - \delta)$$

Inserting these into Eq. (B.6e), (B.6f), we get $AA = \cos \theta \cos \phi$, $BB = \cos \theta \sin \phi$. Then inserting AA, BB into Eq. (B.6c), (B.6d), we have

$$\cos \phi' = \frac{\cos \phi \sin(\theta - \delta)}{\sin \theta'} = \cos \phi$$

$$\sin \phi' = \frac{\sin \phi \sin(\theta - \delta)}{\sin \theta'} = \sin \phi$$

This is in agreement with our expectations. For the second check, let's set $\delta = 0$. The line OP will reduce to the line OC, i.e. we should have $\theta' = \theta$ and $\phi' = \phi$. Let's use $\delta = 0$, i.e. $\sin \delta = 0$, $\cos \delta = 1$ to calculate $\cos \theta'$, $\sin \theta'$, $\cos \phi'$, $\sin \phi'$. From Eq. (B.6a), it is easy to see $\cos \theta' = \cos \theta$, and $\sin \theta' = \sin \theta$. From Eq. (B.6c),

$$\cos \phi' = \frac{\sin \theta \cos \phi}{\sin \theta'} = \cos \phi$$

From Eq. (B.6d),

$$\sin \phi' = \frac{\sin \theta \sin \phi}{\sin \theta'} = \sin \phi$$

These two checks verify that the relationships Eq. (B.6a) to (B.6f) are correct.

Appendix C

ARGON BEAM SIMULATION

C.1 Beam Expansion

The argon beam consists of a great number of argon ions. To describe the beam's evolution with time t , we use following model which is based on the measurements: In the laboratory calibration, Pollock[1987] showed that the energy of the majority of the argon ions from the argon ion gun with a voltage of 200 volts was around 175ev. On the actual flight, the HEEPS detector found the energy of the majority of the argon ions from the perpendicular gun was about 100ev, and the energy of the argon ions from the parallel gun was about same as on the ground. This observation suggested to us that ions did not lose energy during parallel firings and lost 75 eV during perpendicular events. The reason was that when the argon ion were shot out during perpendicular events, the gun's potential relative to the distant ionosphere dropped ~ 100 volts. This potential difference was associated with an electric field roughly perpendicular to the rocket spin axis. This negative electric field reduced the perpendicular energies of the argon ions and did not substantially effect the parallel energies, i.e.

$$E_{\perp} - E'_{\perp} = 75ev$$

$$E_{\parallel} = E'_{\parallel}$$

or

$$\frac{1}{2}mv_{\perp}^2 - \frac{1}{2}mv'_{\perp}{}^2 = 75ev$$

where the v_{\perp}, v'_{\perp} are the original and final perpendicular velocities of the argon ions respectively. The angles θ and the θ' are measured from the beam center line, (see Fig. C-1).

If the perpendicular component of the original energy is

$$\frac{1}{2}mv_{\perp}^2 = 175ev \times \cos^2 \theta \quad (C.1)$$

then the perpendicular component of the reduced energy will be

$$\frac{1}{2}mv'_{\perp}{}^2 = 100ev \times \cos^2 \theta' \quad (C.2)$$

i.e.

$$175 \cos^2 \theta - 100 \cos^2 \theta' = 75 \quad (C.3)$$

The solution to this equation is

$$\cos \theta' = \frac{1}{2} \sqrt{7 \cos^2 \theta - 3} \quad (C.4)$$

From this solution, we can find that the beam cone angle expands due to the perpendicular energy reduction:

$$\text{for } \theta = 0^\circ \quad \cos \theta' = 1 \quad \Rightarrow \theta' = 0^\circ$$

and

$$\text{for } \theta = 30^\circ \quad \cos \theta' = \frac{3}{4} \quad \Rightarrow \theta' = 41.41^\circ$$

These results tell us that the expansion of the beam is nonlinear. At the edge of the beam, a cone that originally was 30° wide will expand to a 41.41° cone.

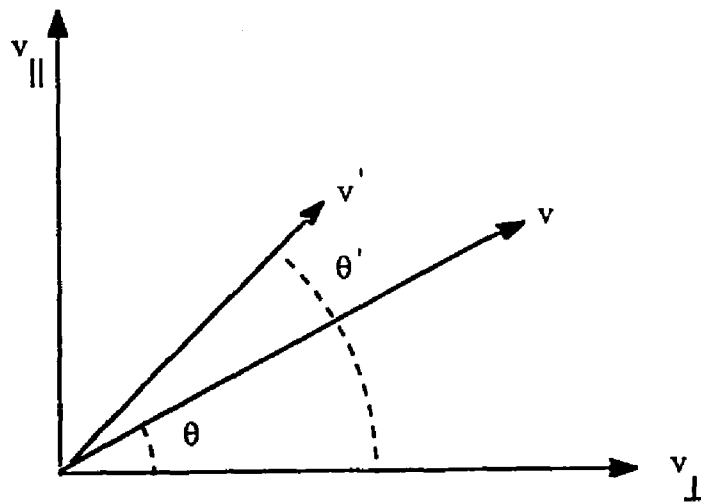


Fig. C-1 Beam Expansion

C.2 Density Weighting Function

From the laboratory calibration [C. Pollock, 1987], we knew the differential density ratio of the argon beam ejected by the ion gun was

$$\frac{dn/d\Omega|_{\theta=30^\circ}}{dn/d\Omega|_{\theta=0^\circ}} = \frac{1}{2}$$

Where the dn is the differential number of ions, and the $d\Omega$ is the differential solid angle. If we set the differential density at the beam center to 1, then

$$\frac{dn}{d\Omega}|_{\theta=30^\circ} = \frac{1}{2} \quad (C.5)$$

What is the new differential density ratio after the beam expansion due to the perpendicular energy reduction? This is an important parameter we must to know before we are able to evaluate the evolution of the beam density. To do this, let's take a derivative of Eq. (C.3), we have

$$\frac{4}{7} \cos \theta' (\sin \theta' d\theta') = \cos \theta (\sin \theta d\theta)$$

i.e.

$$\frac{d\Omega'}{d\Omega} = \frac{7 \cos \theta}{4 \cos \theta'} \quad (C.6)$$

where

$$d\Omega = 2\pi \sin \theta d\theta$$

is the differential element of solid angle at the angle θ from the cone's center line, and

$$d\Omega' = 2\pi \sin \theta' d\theta'$$

is the differential element of the solid angle at a angle θ' from the cone's center line. The equation (C.6) represents the expansion of the solid an-

gles. Now we can easily find the differential density ratio between expanded beam and original beam:

$$\frac{dn'/d\Omega'}{dn/d\Omega} = \frac{d\Omega}{d\Omega'} = \frac{4 \cos \theta'}{7 \cos \theta} \quad (C.6a)$$

Here we used $dn' = dn$, i.e. the number of ions is conserved. For the expanded beam, the differential density ratio between 41.41° and the center of the beam is

$$\begin{aligned} \frac{dn'/d\Omega'|_{41.41^\circ}}{dn'/d\Omega'|_{0^\circ}} &= \frac{(\cos \theta' / \cos \theta) dn/d\Omega|_{\theta'=41.41^\circ}}{(\cos \theta' / \cos \theta) dn/d\Omega|_{\theta'=0^\circ}} = \frac{(\frac{3}{4} / \frac{\sqrt{3}}{2}) dn/d\Omega|_{\theta'=41.41^\circ}}{(1/1) \times 1} \\ &= \frac{\sqrt{3}}{2} \frac{dn}{d\Omega}|_{\theta'=41.41^\circ} \quad (C.7) \end{aligned}$$

where we have selected $dn/d\Omega|_{\theta'=0} = 1$. If the differential density is uniformly distributed before the expansion, i.e.

$$\frac{dn}{d\Omega}|_{\theta'=41.41^\circ} = 1$$

here $\theta' = 41.41^\circ$ corresponding to $\theta = 30^\circ$. Then, the differential density at $\theta' = 41.41^\circ$ is

$$\frac{dn'/d\Omega'|_{\theta'=41.41^\circ}}{dn'/d\Omega'|_{\theta'=0^\circ}} = \frac{\sqrt{3}}{2}$$

We can approximate the differential density is

$$\frac{dn'}{d\Omega'} = w(\theta') = \cos^{\frac{1}{2}} \theta' \quad (C.8)$$

because

$$\cos(41.41^\circ) = \frac{3}{4}$$

and

$$\cos^{\frac{1}{2}}(41.41^\circ) = \frac{\sqrt{3}}{2}$$

If the differential density is non - uniformly distributed before the expansion, such as

$$\frac{dn}{d\Omega} \Big|_{\theta=30^\circ} = \frac{1}{2}$$

then, the differential density at $\theta' = 41.41^\circ$ is

$$\frac{dn'}{d\Omega'} \Big|_{\theta'=41.41^\circ} = \frac{\sqrt{3}}{4}$$

so, we can choose the weighting function of the differential density as

$$\frac{dn'}{d\Omega'} = w(\theta') = \cos^{2.9} \theta' \quad (C.9)$$

because

$$\cos^{2.9}(41.41^\circ) \approx \frac{\sqrt{3}}{4}$$

The differential particle number density is

$$\begin{aligned} dn' &= c \cos^{2.9} \theta' d\Omega' \\ &= c \cos^{2.9} \theta' 2\pi \sin \theta' d\theta' \end{aligned} \quad (C.10)$$

So the total number of ions inside the beam cone of half angle θ' yields

$$n'(\theta') = \frac{2\pi c}{3.9} (1 - \cos^{3.9} \theta') \quad (C.11)$$

Summary of weighting functions:

$$w(\theta) = 1$$

For the case 1, with plasma uniformly distributed within an unexpanded beam cone.

$$w(\theta) = \cos^{\frac{1}{2}} \theta$$

For case 2, an expanded beam cone, uniformly distributed over all beam cone before the expansion.

$$w(\theta) = \cos^{2.9} \theta$$

For case 3, a expanded beam cone, but with the differential density ratio 1:2, i.e. the differential density at the $\theta = 30^\circ$ was half of that at the center before expansion. Note, we will not distinguish between before the expansion and after the expansion, and drop the prime symbol (') from now on.

C.3 Generating Ion Distributions

In this section we will use a random number generator to simulate the argon ions distribution at the aperture of the gun. In the last section we found that the total number of ions inside the cone with a maximum half angle of θ_{max} is

$$n(\theta_{max}) = c \int_0^{\theta_{max}} w(\theta) d\Omega$$

and the total number of ions inside the cone with a half angle of θ is

$$n(\theta) = c \int_0^{\theta} w(\theta) d\Omega$$

Obviously the ratio between the $n(\theta)$ and the $n(\theta_{max})$ is in the range of 0 to 1. But we know that a general random generator can generate a uniform distribution between 0 and 1. So we can use the random number generator to generate the ratio between the $n(\theta)$ and the $n(\theta_{max})$, i.e.

$$\frac{n(\theta)}{n(\theta_{max})} = a \text{ random number } R \quad (C.12)$$

For case 1,

$$\frac{n(\theta)}{n(\theta_{max})} = \frac{1 - \cos \theta}{1 - \cos \theta_{max}} = R$$

For case 2,

$$\frac{n(\theta)}{n(\theta_{max})} = \frac{1 - \cos^{3/2} \theta}{1 - \cos^{3/2} \theta_{max}} = R$$

For case 3,

$$\frac{n(\theta)}{n(\theta_{max})} = \frac{1 - \cos^{3.0} \theta}{1 - \cos^{3.0} \theta_{max}} = R$$

For each random number we can solve these equations to find out the corresponding angle θ respectively. It is easy to verify that the definition (C.12) satisfies the requirement of the weighting function, for example, in case 2:

$$\frac{dn(\theta)}{d\Omega} = \frac{dn}{dR} \frac{dR}{2\pi \sin \theta d\theta}$$

where

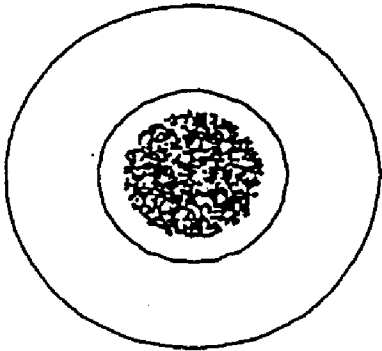
$$\frac{dR}{d\theta} = 3/2 \cos^{1/2} \theta \sin \theta$$

So

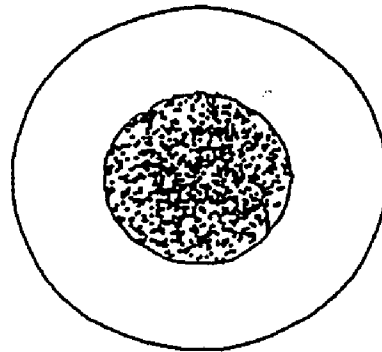
$$\frac{dn(\theta)}{d\Omega} \sim \cos^{1/2} \theta$$

This expression agrees with the requirement of case 2. It is true for all cases. In Fig. C-2, the left two diagrams show uniformly distributed ions with 30° and 90° half opening angles respectively. The right two diagrams show the ion distribution functions which have 2:1 distribution ratio before the perpendicular energies of ions were lost. After the perpendicular energies were lost, the upper right diagram shows the beam is expanding from 30° to 41°, the lower right diagram shows the beam is expanding to 90°.

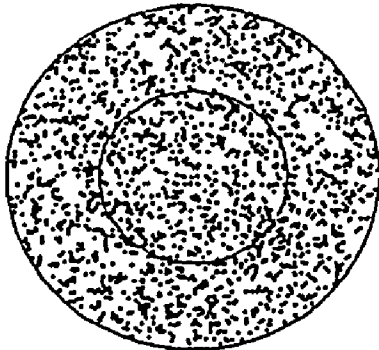
30, UNIFORM



1:2, 30 TO 41



90, UNIFORM



1:2, TO 90

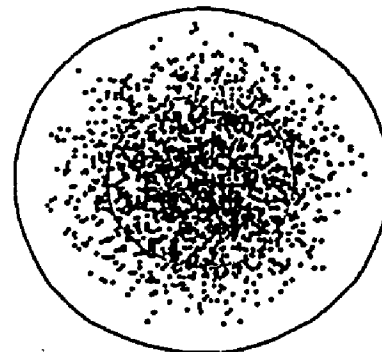


Fig. C-2 Beam Density Distributions

Appendix D

TRANSFORMATION FROM \mathbf{u} TO \mathbf{k} FRAME

As in appendix A, we can perform a series rotations to complete the transformation from the streaming frame (\mathbf{u} frame) to the wave vector frame (\mathbf{k} frame). To simplify the transformation, we choose two coordinate systems as follows: for the \mathbf{u} frame, define the streaming direction \mathbf{u} as the Z axis, and the X axis is in the $\mathbf{B} - \mathbf{u}$ plane; for the \mathbf{k} frame, define the \mathbf{k} direction as the Z axis, and as before, we always choose the X axis in the $\mathbf{B} - \mathbf{k}$ plane, as shown in the Fig. D-1.

In Fig. D-1, θ is the pitch angle of \mathbf{k} , α is the pitch angle of \mathbf{u} , and β is the azimuthal angle of \mathbf{u} . The transform procedures from the \mathbf{u} frame to the \mathbf{k} frame are :

1. rotate through an angle $-\alpha$ around the Y axis of the \mathbf{u} frame, this will place the Z axis of the \mathbf{u} frame in the direction of the magnetic field \mathbf{B} . The transform matrix is

$$\mathfrak{R}_a = \begin{pmatrix} \cos \alpha & 0 & \sin \alpha \\ 0 & 1 & 0 \\ -\sin \alpha & 0 & \cos \alpha \end{pmatrix} \quad (D.1)$$

2. rotate through an angle $-\beta$ around the Current Z axis (\mathbf{B}). The current X axis will turn to the direction of the X axis of the \mathbf{k} frame. The transformation matrix is

$$\mathfrak{R}_b = \begin{pmatrix} \cos \beta & -\sin \beta & 0 \\ \sin \beta & \cos \beta & 0 \\ 0 & 0 & 1 \end{pmatrix} \quad (D.2)$$

3. rotate through an angle θ around the current Y axis (now aligned along the Y axis of the \mathbf{k} frame). The current Z axis will turn to the direction of the wave vector \mathbf{k} . The transformation matrix is

$$\mathfrak{R}_c = \begin{pmatrix} \cos \theta & 0 & -\sin \theta \\ 0 & 1 & 0 \\ \sin \theta & 0 & \cos \theta \end{pmatrix} \quad (D.3)$$

Finally, the transformation from the streaming \mathbf{u} frame to the wave vector \mathbf{k} frame is

$$\begin{aligned} \mathfrak{R} &= \mathfrak{R}_c \mathfrak{R}_\beta \mathfrak{R}_\alpha \\ &= \begin{pmatrix} \cos \theta \cos \beta \cos \alpha + \sin \theta \sin \alpha & -\cos \theta \sin \beta & \cos \theta \cos \beta \sin \alpha - \sin \theta \cos \alpha \\ \sin \beta \cos \alpha & \cos \beta & \sin \beta \sin \alpha \\ \sin \theta \cos \beta - \cos \theta \sin \alpha & \sin \theta \sin \beta & \sin \theta \cos \beta \sin \alpha + \cos \theta \cos \alpha \end{pmatrix} \\ &\quad (D.4) \end{aligned}$$

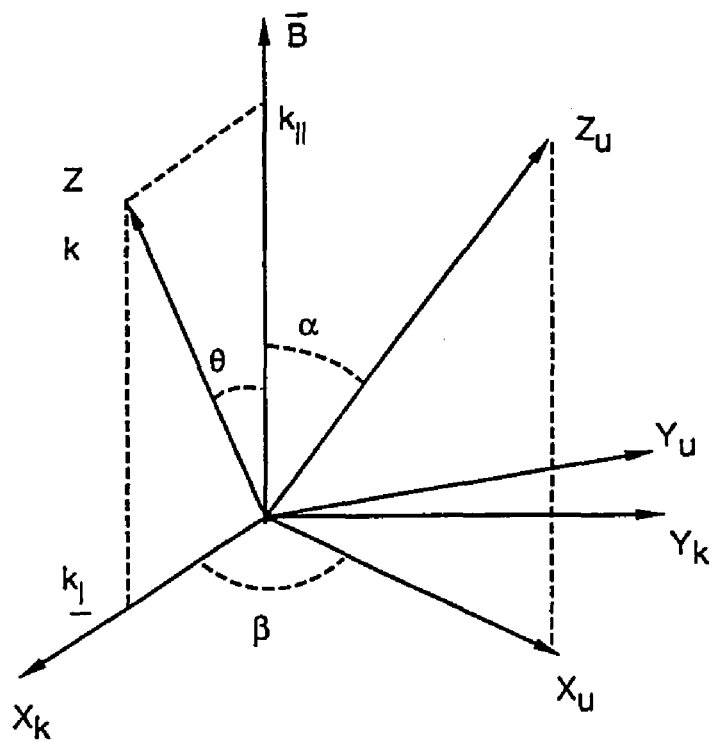


Fig. D-1 The Relationship Between The Three Coordinate System: Local Geomagnetic Field B Frame, Beam U Frame and Wave Vector K Frame

BIBLIOGRAPHY

- o Akhiezer, A. I., I. A. Akhiezer, R. V. Polovin, A. G. Sitenko, and K. N. Stepanov, *Plasma Electrodynamics, Vol. 2, Non - Linear Theory and Fluctuations*, Pergamon, New York, 1975.
- o Arnoldy, R. L., C. J. Pollock and J. R. Winckler, *The Energization of Electrons and Ions by Electron Beams Injected in the Ionosphere*, *J. Geophys. Res.*, 90, 5197, 1985.
- o Chen, F. F., *Introduction to Plasma Physics*, Plenum Press, New York, 1974.
- o Dusenbery, P. B. and R. L. Kaufmann, *Properties of the Longitudinal Dielectric Function: An Application to the Auroral Plasma*, *J. Geophys. Res.*, Vol. 85, NO. A11, Page 5969 - 5976, 1980.
- o Erlandson, R. E., *Plasma Waves Generated During an Artificial Argon Ion Beam Experiment in Ionosphere*, Ph.D. Thesis, University of Minnesota, 1986.
- o Erlandson, R. E., L. J. Cahill, Jr., C. J. Pollock, R. L. Arnoldy, W. A. Scales and P. M. Kintner, *Initial Results from the Operation of Two Argon Ion Generators in the Auroral Ionosphere*, *J. Geophys. Res.*, 92, 4601, 1987.
- o J. V. Evans, *Some Post-war Developments in ground-Based Radiowave Sounding of the Ionosphere*, *Journal of Atmospheric and Terrestrial Physics*, 1974, Vol. 36, pp.2183- 2234.
- o Fried, B. D., and S. D. Conte, *The Plasma Dispersion Function*, Aca-

- demic, New York, 1961.
- o Ginzburg, V. L., Propagation of Electromagnetic Waves in Plasma, Gordon and Breach, New York, 1961.
 - o Haerendel, G. and R. Z. Sagdeev, Artificial Plasma Jet in the Ionosphere, *Adv. Space Res.*, 1, 29, 1981.
 - o Häusler, B., R. A. Treuman, O. H. Bauer, G. Haerendel, R. Bush, C. W. Carlson, B. Theile, M. C. Kelley, V. S. Dokukin and Yu Ya Ruzhin, Observations of the Artificially Injected Porcupine Xenon Ion Beam in the Ionosphere, *J. Geophys. Res.*, 91, 287, 1986.
 - o Hudson, M. K., and I. Roth, Thermal Fluctuations From an Artificial Ion Beam Injection into the Ionosphere, *J. Geophys. Res.*, 89, 9812, 1984.
 - o Hughes. T. P., Plasma and Laser Light, Halsted Press, a division of John Wiley & Sons, Inc., New York, 1975.
 - o Ichimaru, Setsuo, Basic Principle of Plasma Physics, Benjamin/ Cummings Publicashing Company, Inc. 1973.
 - o Jones, D., X_e^+ Induced Ion-Cyclotron Waves, *Space Res.*, 20, 379, 1981.
 - o Kang, S. and Chen Y. Handbook of Plasma Physics, Chinese Academy of Science, 1981, in Chinese.
 - o Kaufmann, R. L. Electrostatic Wave Growth: Secondary Peaks in a Measured Auroral Electron Distribution Function, *JGR*, Vol. 85, NO. A4, p1713-1721, April 1980.
 - o Kaufmann, R. L., R. L. Arnoldy, T. E. Moore, P. M. Kintner, L. J. Cahill, Jr., and D. N. Walker, Heavy Ion Beam-Ionospheric Interactions: Electron Acceleration, *J. G. Res.*, Vol. 90, No. A10, page 9595 - 9614, Oct 1, 1985.

- o Kellogg, P. J. Calculations and Observations of Thermal Electrostatic Noise in Solar Wind Plasma, *Plasma Phys.*, 23, 75, 1981.
- o Kintner, P. M., J. Labelle, W. Scales, R Erlandson and L. J. Cahill, A Comparison of Plasma Waves Produced by Ion Accelerations in the F - Region Ionosphere *Geophysical Monograph* 38, 1986.
- o Kintner, P. M., and D. J. Gorney, A Search For the Plasma Processes Associated with Perpendicular Ion Heating, *J. Geophys. Res.*, 89, 937, 1984.
- o Krall, N. A., and A. W. Trivelpiece, principles of Plasma Physics, McGraw-Hill, New York, 1973.
- o Kenneth R. Lang, Astrophysical Formulae, 2nd edition, Springer-Verlag, Berlin, Heidelberg, New York, 1980.
- o Lifshitz and Pitaevskii, Physical Kinetics, 1981.
- o Montgomery, D. A. Tidman, Plasma Kinetic Theory, McGraw-Hill, New York, 1964.
- o Malingre, M. and R. Pottellette, Excitation of Broadband Electrostatic Noise and of Hydrogen Cyclotron Waves by a Perpendicular Ion Beam in a Multi-Ion Plasma, *Geophys, Res. Lett.*, 12, 275, 1985.
- o Moore, T. E., R. L. Arnoldy, R. L. Kaufmann, L. J. Cahill, Jr., P. M. Kintner, and D. W. Walker, Anomalous Auroral Electron Distributions Due to an Artificial Ion Beam in the Ionosphere, *J. Geophys. Res.*, 87, 7569, 1982.
- o Moore, T. E., R. L. Arnoldy, L. J. Cahill, Jr., and P. M. Kintner, Plasma Jet Effects on the Ionospheric Plasma, Active Experiments in Space *Eur. Space Agency Spec. Publ.*, ESA SP-195, 197-206, 1983.
- o Okuda, H., and M. Ashour-Abdalla, Formation of a Conical Distribu-

- tion and Intense Ion Heating in the Presence of Hydrogen Cyclotron Waves, *Geophys. Res. Lett.*, 8, 811, 1981.
- o Pollock, C. J., Rocket-Borne Low Energy Ion Measurements in Space, Ph. D. Thesis, University of New Hampshire, Durham, September, 1987.
 - o C. J. Pollock, R. L. Arnoldy, R. E. Erlandson, L. J. Cahill, Observations of the Plasma Environment During an Active Ionospheric Ion Beam Injection Experiment, *J. Geophys. Res.*, Vol. 93, NO. A10, Page 11473-11493, OCT 1, 1988.
 - o J. A. Ratcliffe, Experimental Methods of Ionospheric Investigation, 1925 - 1955. *Journal of Atmospheric and Terrestrial Physics*, 1974, Vol. 36, pp. 2095- 2103.
 - o Rostoker, N., Fluctuations of a Plasma, *Nucl. Fusion*, 1, 101, 1961.
 - o Roth, I., C. W. Carlson, M. K. Hudson, and R. L. Lysak, Simulations of Beam Excited Minor Species Gyroharmonics in the Porcupine Experiment, *J. Geophys. Res.*, 88, 8115, 1983.
 - o Tang Keyun, Spectral Analyses in the Studies of the Whistler Waves. M. S. Thesis, Chinese Academy of Science, Beijing, 1981.
 - o Treumann, R. A. and B. Häusler, The Propagation of a Dense Quasi-Neutral Ion Beam Across a Magnetized Plasma, *Astrophys. & Space Sci.*, 110, 371, 1984.
 - o A. H. Waynick, Fifty Years of the Ionosphere. The Early Years - Experimental, *Journal of Atmospheric and Terrestrial Physics*, 1974, Vol. 36, pp. 2105-2111.
 - o Whalen, B. A., A. W. Yau., F. Creutzberg and M. B. Pongratz, Waterhole - an Auroral-Ionosphere Perturbation Experiment, *Physics of*

Auroral Arc Formation, American Geophysical Union, Washington D. C., 1981.

- o Xu, J. and Jin, S., Plasma Physics. Publicashing Agency of Atomic Energy, Beijing, 1981, in Chinese.